

# **Mechanistic studies of iron uptake into, and release from, Ferritins**

**by**

**Raz Farook Abdulqadir**

**A thesis submitted to the School of Chemistry, University of East  
Anglia in fulfillment of the requirements for the degree of Master of  
Science**

**June 2013**

**© This copy of the thesis has been supplied on condition that  
anyone who consults it is understood to recognize that its copyright  
rests with the author and that no quotation from thesis, nor any  
information derived there from, may be published without the  
author's prior, written consent.**

## Acknowledgements

I would like to thank:

I am deeply indebted to my supervisors, Professor Nick Le Brun and Professor Geoff Moore. Their stimulating suggestions and encouragement helped me throughout my research and during the writing of this thesis;

The members of the NLB group for all their help, advice and friendship;

This research would not have been possible without the involvement of our collaborators Dr. Steve Wong, Stephanie Pfaffen, Prof. Grant Mauk, Prof. Michael Murphy, and members of their labs.

My family, my parents: Saadia and Farook, my brothers and sister for always believing in me, for their continuous love and their support in my decisions. Without them I could not have made it here;

Last, but not least, my husband Zryan whose patient love and encouragement enabled me to complete this work.

## Abstract

Iron is the most common and perhaps the most crucial transition metal. It is essential for virtually all of life yet it is also potentially extremely toxic; therefore, how organisms handle iron (iron metabolism) is of critical importance. Ferritins constitute a large family of iron storage proteins that are found throughout life, in bacteria, archaea, plants and animals. The newly discovered ferritin from the bloom-forming pennate diatom *Pseudo-nitzschia multiseries* is similar to other eukaryotic ferritins that contains a ferroxidase centre but also contains a third site (site C) only previously found in non-heme bacterial ferritins. The mechanism of iron uptake in *P. multiseries* ferritin and the effect of substitution of residues at site C has been studied using rapid reaction kinetic methods. These revealed that oxidation in PmFTN is very rapid suggesting a distinct mechanism of iron uptake.

Bacterioferritin (BFR) is a unique heme-containing bacterial member of the ferritin family that stores up to 2700 iron ions as a ferric oxyhydroxide phosphate mineral within its central cavity. This core is surrounded by 24 identical protein subunits, each of which possesses a dinuclear iron centre that catalyses the oxidation of Fe(II) to Fe(III). The heme-binding sites are sandwiched between pairs of subunits and coordinated by two methionine residues (one from each subunit). The heme groups play an important role in iron release, though understanding of this has been hampered by the difficulty in obtaining fully heme-loaded protein that is isolated from over-expressing bacterial cultures. Here, an in vitro heme-loading method is described and used to generate BFR containing variable amounts of heme. Studies of iron release indicate increased heme levels only marginally increases the rate of iron release and actually lowers the extent of iron release. These results suggest that the reconstituted heme-loaded protein behaves differently from naturally heme-loaded protein.

## Abbreviations

% v/v	volume of substance in mL per 100 mL of total solution
% w/v	weight of substance in grams per 100 mL of total solution
$\epsilon$	Extinction coefficient ( $M^{-1} \text{ cm}^{-1}$ )
$\Delta A$	change in absorbance
$\mu\text{l}$	microlitre ( $1 \mu\text{l} = 10^{-6} \text{ L}$ )
$\mu\text{M}$	micromolar ( $1 \mu\text{M} = 10^{-6} \text{ M}$ )
A	Absorbance
BCA	Bicinchoninic acid
BFR	Bacterioferritin
BSA	Bovine serum albumin
DPS	DNA binding protein from starved cells
EDTA	Ethylenediaminetetraacetic acid
Ftn	ferritin
FtnA	non-heme bacterial ferritin
Hepes	4-(2-Hydroxyethyl)piperazine-1-ethanesulfonic acid
IPTG	Isopropyl $\beta$ -D-thiogalactopyranoside
L	litre
M	molar, unit of concentration (moles per liter)
MES	2-( <i>N</i> -morpholino)ethanesulfonic acid
mL	millilitre ( $1 \text{ mL} = 10^{-3} \text{ L}$ )
mM	millimolar ( $1 \text{ mM} = 10^{-3} \text{ M}$ )
MOPS	3-( <i>N</i> -morpholino)propanesulfonic acid
NHE	normal hydrogen electrode
PAGE	polyacrylamide gel electrophoresis
PDB	protein data bank

PmFTN	<i>Pseudo-nitzschia multiseri</i> ferritin
rpm	revolutions per minute
SDS	sodium dodecyl sulfate
TEMED	N,N,N',N'-tetramethylethylenediamine
Tris	tris(hydroxymethyl)aminomethane
U.V.	ultraviolet
Wt	wild type

# Table of Contents

---

## Chapter 1: Introduction

---

	<b>Page</b>
<b>1.1 The chemistry and biology of iron</b>	10
<b>1.2 Overview of ferritin and ferritin-like proteins</b>	11
<b>1.3 Physiological role of iron storage proteins</b>	14
<b>1.4 Mechanism of iron uptake in Eukaryotic ferritins</b>	15
<b>1.5 Mechanism of iron release from Eukaryotic ferritins</b>	17
<b>1.6 <i>Pseudo-nitzschia multiseri</i> Ferritin</b>	18
<b>1.7 Structural features of PmFTN</b>	20
1.7.1 Ferroxidase centre and site C	20
1.7.2 Comparison of PmFTN with bacterial ferritin	22
<b>1.8 Bacterioferritin</b>	24
1.8.1 The ferroxidase centre and inner-surface site	27
1.8.2 Heme-binding site	29
1.8.3 The iron mineral core	30
<b>1.9 Mechanistic aspects of BFR</b>	31
1.9.1 Mechanism of iron mineralization	31
1.9.2 Mechanism of iron release	33
<b>1.10 Goals of current study</b>	34

---

## Chapter 2: Materials and methods

---

	Page
<b>2.1 Overproduction and purification of Wt and M52H BFR from <i>E. coli</i></b>	36
2.1.1 Strains and plasmids	36
2.1.2 Preparation of media and growth cultures	36
2.1.3 Cell harvest and disruption	36
2.1.4 Crude purification steps	37
2.1.5 Column chromatography	37
2.1.6 SDS-PAGE Analyses	38
<b>2.2 Removal of iron from BFR to generate Apo-BFR</b>	38
<b>2.3 PmFTN samples</b>	39
<b>2.4 Protein and iron concentration determinations</b>	40
<b>2.5 Spectroscopic and Kinetic Analyses</b>	41
2.5.1 UV-visible absorbance spectroscopy	41
2.5.2 Stopped flow analysis	42
2.5.3 Addition of heme to BFR	44
2.5.4 Addition of Fe(II) to apo-protein	44
2.5.5 Fe(II) oxidation rate analysis	45
2.5.6 Release of iron from the core	46

---

## Chapter 3: Mechanistic study of iron uptake by a pennate diatoms ferritin

---

	Page
<b>3.1 Study of iron uptake in PmFTN</b>	48
<b>3.2 Iron core formation in PmFTN</b>	48
<b>3.3 Iron oxidation kinetics at the ferroxidase centre</b>	51

<b>3.4 Regeneration of rapid oxidation in PmFTN</b>	<b>59</b>
<b>3.5 The formation of di-Fe(III) peroxo complex formation</b>	<b>62</b>
<b>3.6 Discussion</b>	<b>64</b>

---

## **Chapter 4: Mechanistic study of iron mineralisation variants of diatom ferritin**

---

	<b>Page</b>
<b>4.1 Non-Cys variant of PmFTN</b>	<b>69</b>
4.1.1 Fe(II) oxidation kinetics at the ferroxidase centre	71
4.1.2 Regeneration of rapid oxidation in PmFTN	73
<b>4.2 Variations of PmFTN at site C</b>	<b>75</b>
<b>4.3 E44Q variant of PmFTN</b>	<b>75</b>
4.3.1 Fe(II) oxidation kinetics at the ferroxidase centre	77
4.3.2 Regeneration of rapid oxidation in PmFTN	79
<b>4.4 E44H variant of PmFTN</b>	<b>81</b>
4.4.1 Fe(II) oxidation kinetics at the ferroxidase centre	81
4.4.2 Regeneration of rapid oxidation in PmFTN	83
<b>4.5 E130A variant of PmFTN</b>	<b>85</b>
4.5.1 Fe(II) oxidation kinetics at the ferroxidase centre	85
4.5.2 Regeneration of rapid oxidation in PmFTN	87
<b>4.6 Iron core formation kinetics in PmFTN</b>	<b>89</b>

## Chapter 5: Mechanistic studies of iron release from Bacterioferritin

---

	Page
<b>5.1 Purifications in BFR</b>	93
<b>5.2 Heme loading of <i>E. coli</i> BFR via heat-treatment method</b>	94
5.2.1 The addition of exogenous heme to wild-type BFR	94
5.2.2 The addition of exogenous heme to heme-free (M52H) variant of BFR	96
<b>5.3 The effect of heme on mineralisation in and iron release from <i>E. coli</i> BFR</b>	101
5.3.1 Effect of heme on <i>E. coli</i> BFR iron core formation	101
5.3.2 Effect of heme on iron release from <i>E. coli</i> BFR	104
<b>5.4 Discussion</b>	111
5.4.1 The mechanism of exogenous heme-binding to BFR	111
5.4.2 The effect of heme on iron core formation	112
5.4.3 The role of heme in iron release from BFR	113

---

## Chapter 6: General Discussion

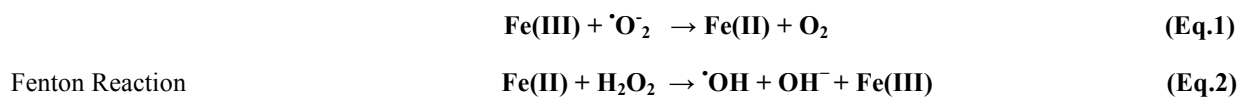
---

	Page
<b>6.1 Mechanistic study of iron uptake by a pennate diatoms ferritin</b>	115
<b>6.2 Mechanistic studies of iron release from Bacterioferritin</b>	120
<b>References</b>	121

# Chapter 1: Introduction

## 1.1 The chemistry and biology of iron

With a few exceptions, virtually all studied organisms need iron for survival. Most organisms utilize iron as a cofactor for fundamental biochemical activities, such as oxygen transport, nitrogen fixation, electron transfer reactions, photosynthesis, respiration, and DNA synthesis (1). Iron can be incorporated into proteins as iron-sulfur clusters, mononuclear iron sites, dinuclear iron sites, mixed metal dinuclear sites, and heme. This is due to the flexible coordination chemistry and redox reactivity of iron, which allow it to associate with proteins and bind to oxygen, transfer electrons or mediate catalytic reactions. In the Earth's crust, iron is the second most abundant metal and fourth most abundant element. However, iron is also poorly available and potentially toxic due to atmospheric dioxygen. The thermodynamically stable ferrous ( $\text{Fe}^{2+}$ ) ( $E^\circ \text{Fe}^{3+} / \text{Fe}^{2+} = +0.77$  volts versus NHE) is converted to ferric ( $\text{Fe}^{3+}$ ) form, in the presence of dioxygen ( $E^\circ \text{O}_2 / \text{H}_2\text{O} = +1.23$  volts versus NHE). This is significant because in aqueous solution at neutral pH values ferrous iron is soluble (up to 0.1 M), whereas the ferric form is insoluble (up to  $1.4 \times 10^{-9}$  M, depending on pH) therefore limiting the concentration of iron (2, 3). Therefore, the oxidised  $\text{Fe}^{3+}$  is poorly bioavailable, despite its high abundance, due to limited solubility. Furthermore, in the presence of reductant(s) and dioxygen, iron can cycle between the ferrous and ferric forms, leading to reduction of  $\text{O}_2$  to superoxide ( $\cdot\text{O}_2^-$ ), hydrogen peroxide ( $\text{H}_2\text{O}_2$ ) and the hydroxyl radical ( $\text{OH}\cdot$ ) (4). This chemistry is summarised in the following equations (Eq. 1-3) :



Hydroxyl radicals, in particular, will react essentially instantaneously with all types of biological macromolecules like DNA, proteins and membrane lipids, typically disturbing their activity and sometimes damaging them completely (5). As iron readily shuttles between the reduced ferrous and the oxidised ferric forms, disruption of the cellular redox equilibrium requires only catalytic amounts of the metal. Despite its clear importance, organisms are challenged with the paradoxical hazard of iron deficiency and iron overload, each with its serious or fatal consequences. To prevent iron toxicity and iron-induced oxidative stress associated with damage of cellular macromolecules, tissue injury and disease, organisms have developed sophisticated mechanisms to control iron in the cell. These mechanisms involve iron-storage proteins belonging to the ferritin family, which store low solubility and low availability iron and make it available as needed for anabolic processes. Ferritins have been intensively studied for several decades and much is known about their ability to store iron in a soluble, bioavailable, non-toxic form, that is readily accessible when needed (1, 3).

## 1.2 Overview of ferritin and ferritin-like proteins

Ferritin is ubiquitously found in most, plants, animals, microorganisms with the exception of yeast. Ferritins were first discovered in higher eukaryotes, with a unique molecular architecture, comprising 24 structurally similar subunits of H (heavy) and L (light) type. Each of these subunits is composed of a four helical bundle with a fifth short helix at the C-terminal.

Mammalian ferritins are all heteropolymers of 24 subunits that form a roughly spherical shell (of

~ 120 Å diameter) with a 4,3,2 octahedral symmetric arrangement (as shown in Figure 1.1) that encloses the central iron storage cavity (of ~70 Å diameter). The two types of subunit, (H) heavy chain and (L) light chain, with an apparent molecular weight of 21 kDa or 19 kDa, respectively, are closely related in sequence and structurally homologous. In ferritin, the assembled 24 subunits are held tightly together leaving eight narrow (about 4 Å wide in diameter) hydrophilic channels at the 3-fold axes and six hydrophobic channels at the 4-fold axes (6-8).

Ferritins were subsequently discovered in plants, bacteria and archaea, in which all of the subunits are H-chain-like. In bacteria, there are different types of ferritins; often several of these are present in a single cell. Several ferritin or ferritin-like proteins are found in *Escherichia coli* (*E. coli*) such as bacterial ferritin (FtnA and FtnB, the latter of which does not contain a recognisable catalytic centre, bacterioferritin and Dps (DNA binding protein from starved cells). No evidence has yet been presented for the co-assembly of subunits making up these different proteins, but this remains a possibility. *E. coli* FtnA is composed of a subunit (~19.5 kDa) that in terms of sequence is approximately 22% identical to eukaryotic H-chain ferritin, but in terms of structure bears a remarkable similarity. The 3-fold channels are lined by both hydrophobic and hydrophilic residues and are significantly less polar than their eukaryotic ferritin counterparts. The 4-fold channels are polar at both ends and hydrophobic in character in their central part. Distinct channels, called B-channel, are present in prokaryotic ferritins only. These are hydrophilic in nature and occur where one subunit dimer meets another in a side-on fashion, such that there are 12 such channels per ferritin (9). It is possible that B-channels in BFRs and Ftns are functionally comparable to eukaryotic ferritin three-fold channels (9, 10).

It has been suggested that the core mineralisation of Ftn occurs via a mechanism similar to that of eukaryotic H-chain ferritin but is more complicated due to the presence of site C, a third iron

binding site that exists in FtnA, and which is believed to cause some of the mechanistic differences observed between these two proteins (11). FtnB lacks several of the crucial residues that form the catalytic centre of the FtnA subunit. Although less well characterized than FtnA, FtnB is not believed to be capable of forming heteropolymers with FtnA because of the lack of residues important for inter-subunit interactions in FtnA.

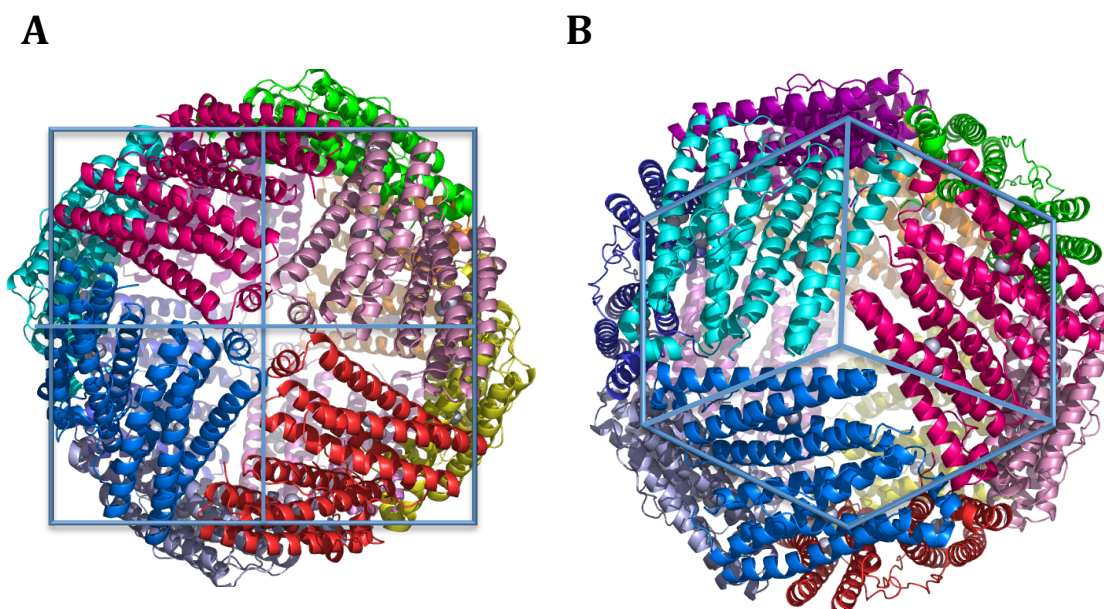


**Figure 1.1.** Structure of prokaryotic ferritin. Cartoon representations of ferritin looking down four-fold (A) and three-fold (B) axes (12). The subunit dimer are represented in various colour and the sphere represent iron at the ferroxidase centre. Figure generated from PDB 3GHQ. This and other structural figures were prepared using Pymol (12).

Dps is the most recently recognized member of the ferritin family. It has a spherical shell-like structure of 3:2 tetrahedral symmetry and is composed of just 12 identical  $\alpha$ -helical ferritin-like subunits, rather than the 24 subunits observed in other ferritins (13).

### 1.3 Physiological role of iron storage proteins

Ferritins have been shown to play different roles in different species of bacteria. Therefore, the exact physiological roles of any one type of proteins are challenging to define. This is, in part, due to the presence of various types of iron storage protein in the same bacterial cell. Studies in *E. coli* and *Porphyromonas gingivalis* have shown that FtnA is important for iron storage (14, 15) and in most cases is probably the principal iron storage protein of cells. Cells have developed different mechanisms to counter the problem that iron imposes as a facilitator of oxygen radical chemistry. While Dps protein is capable of binding and storing up to 500 ferric ions and is structurally related to ferritins, its sole function appears to be to protect the genome from iron-induced free radical damage (16). It does this by two mechanisms. First, Dps binds DNA to protect it physically from oxidative attack. Secondly, free iron is bound and oxidised by hydrogen peroxide in preference to dioxygen, thus removing the reactants for the Fenton reaction (17). Although Dps possesses dinuclear iron sites, these sites are not located in the centre of each subunit, as they are in other ferritins (see section 1.4), but are constructed between pairs of adjacent subunits with each subunit contributing residues that provide ligands for binding iron. BFRs are believed to be mainly involved in iron storage and protection against oxidative stress. In *Neisseria gonorrhoeae* and *Salmonella enterica* serovar Typhimurium BFR has been shown to play important roles in iron storage and protection against oxidative stress under iron-rich conditions, while in *Brucella melitensis* BFR apparently does not have a role in protecting the cells against oxidative stress (17, 18). BFR from *Pseudomonas aeruginosa* provides iron for the heme prosthetic group of KatA, a catalase that is important for protecting the cell against hydrogen peroxide stress (17, 19). Interestingly, *E. coli* BFR minimizes the formation of hydroxyl radicals from the oxidation of ferrous ions by hydrogen peroxide *in vitro*. BFR avoids

Fenton chemistry thus preventing the production of reactive oxygen species and oxidative damage to DNA and other cell components. It does this by catalyzing the two-electron reduction of hydrogen peroxide to water (20).

#### 1.4 Mechanism of iron uptake in Eukaryotic ferritin

Studies suggest that in eukaryotic ferritins, the eight hydrophilic channels function in iron uptake and exit, while the four-fold hydrophobic channels are possibly involved in diffusion of  $O_2$  and  $H_2O_2$  (8, 20, 21). The H-chain subunit of eukaryotic ferritin contains a dinuclear iron centre, known as the ferroxidase centre, located at the centre of the four alpha-helical bundle. The centre is essential for rapid oxidation of Fe(II) to Fe(III) and much work has focused on establishing the mechanistic role of the centre in the mineralisation reaction (8, 22). The ferroxidase centre consists of site A and B as shown in Figure 1.2A.

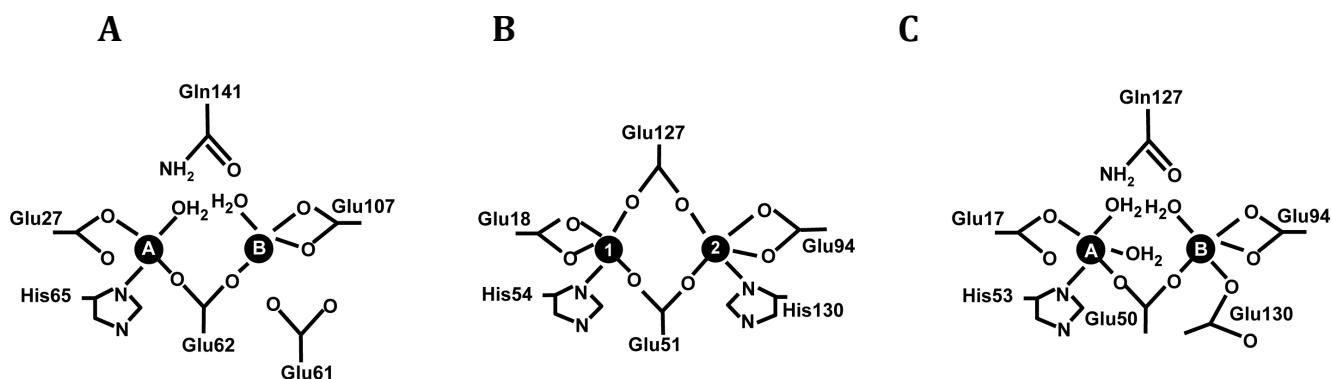
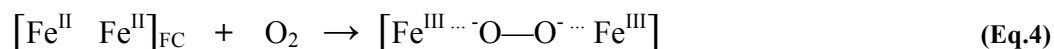


**Figure 1.2.** Schematic representations of (A) the ferroxidase centre of human H-chain ferritin, (B) the symmetric ferroxidase centre of *E. coli* BFR and (C) the ferroxidase centre of FtnA in *E. coli*. Iron in the dinuclear centre is in the ferric form.

A detailed look at the ferroxidation reactions reveals that ferritins of various organisms are characterized by a diverse chemistry of iron deposition and release. In eukaryotic ferritins, in

order to reach the active sites, the Fe(II) substrate crosses the protein cage from the cytoplasmic surface of the cage to the multiple active sites. This is believed to occur via the three fold channels and involves a conserved Glu residue (in each of the three subunits) that forms a constriction half way down the channel (23, 24).

After Fe(II) passes through the channels, it binds to the ferroxidase centre in pairs and promptly reacts with dioxygen to form an intermediate, a  $\mu$ -1,2-peroxodiferric intermediate that gives a characteristic blue colour ( $\lambda$  max at 650 nm). This decays in seconds as indicated in equation 5, to a more stable  $\mu$ -1,2-oxodiferric species (see Equations 4 and 5). The oxidation of two Fe(II) ions is a two electron process and so the expected  $O_2$  reduction product is  $H_2O_2$  (25). The  $\mu$ -oxodiferric species generated by the ferroxidase reaction is itself unstable and this has hindered attempts to structurally characterize the oxidised form of the FC (ferroxidase centre). The stoichiometric release of  $H_2O_2$  is generally not detected, indicating that further reactions take place, although these cannot be Fe(II) oxidation reaction because, if they were, the ratio of  $2Fe:1O_2$  would not be observed (9).



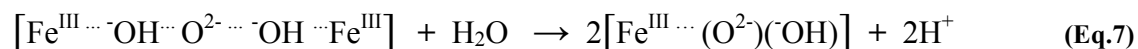
Recently, it was shown by NMR spectroscopy that the pathway of Fe(III) following its exit from the FC involves a 'channel' running along the long subunit axis, entering the cavity at the four fold channel, that is where four such intra-subunit Fe(III) pathways converge (26). Once in the central cavity, Fe(III) which may transit as  $Fe(III)_2O$  units, either attaches to the existing minerals or bind at nucleation sites initiating mineralization (25). L-chain subunits are isostructural with H-chain subunits but lack residues that form the FC catalytic centre. However,

they contain an acidic patch on their cavity-facing surface which is important for efficient nucleation of the core mineral (8, 22).

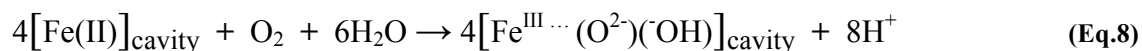
The precise nature of Fe(III) species at defined time points during the mineralisation process is difficult to establish unequivocally. The process may be viewed simply as the hydrolysis of [Fe(III)2O] units that result from oxidation of Fe(II) at the ferroxidase centre. This species could be already partially hydrated before it attaches to the existing mineral/nucleation sites:



and subsequently undergoes further hydration/hydrolysis:



The product here is ferric oxyhydroxide and this is believed to resemble in structure the mineral ferrihydrite ( $5\text{Fe}_2\text{O}_3 \cdot 9\text{H}_2\text{O}$ ). There is a lack of detailed structural information about ferritin mineral cores because in crystals of iron core-containing ferritins, although the protein cages are well ordered, the minerals inside them need not be, and the electron density due to iron mineral is not observed. When larger amounts of iron are added to eukaryotic ferritins, the mineral surface can serve as an alternative catalytic site for Fe(II) oxidation and  $\text{O}_2$  reduction:



These observations initially led to the crystal growth model of mineralisation (9).

### 1.5 Mechanism of iron release from Eukaryotic ferritin

The ferritin mineralisation reaction can be reversed through the addition of electrons and protons (and water), leading to dissolution of the mineral. This reaction can be followed *in vitro* using a

range of reductants, some of which are likely to be physiologically relevant (such as NADH/FMN) (27), together with a chelator that is not physiological but which forms a coloured species, enabling the whole process to be followed kinetically (28).

Although measuring iron release (or at least formation of Fe(II)-chelates) is straightforward, the reaction itself is complex and it is not known whether the reductant contacts the mineral surface directly, or supplies electrons remotely via a transfer chain.

In frog ferritin, it has been shown that the three-fold channels play a key role in the exit of iron from the cavity. Studies revealed that increasing temperature and physiological concentrations of urea leads to opening of the channels, due to localized unfolding. The amino acids residues responsible for the formation of the gated pore are: (Arg 72–Asp 122) that form an ion pair, (Leu134–Leu110) that form a hydrophobic interaction, and (N-terminus-Arg 72) by hydrogen bond interactions. A mutation of any of these residues remarkably increases the ability of iron to migrate out of the interior of the ferritin cage during reductive iron release studies (21, 29).

Another mechanism of iron release from eukaryotic ferritins involves lysosomal degradation of the ferritin protein shell. Lysosomes are membrane-bound compartments that contain many proteolytic enzymes and proton pumps that decrease the local pH. Although ferritin does accumulate in lysosomes under conditions of iron over-supply, this route of iron release is not likely to be a major one under normal circumstances. From what is now known about the complexities of iron metabolism, it also would make little sense for the cell to release large amounts of iron at one time, as this would lead to iron toxicity (29).

### **1.6 *Pseudo-nitichia multiseries* Ferritin**

About 30-40% of the world's oceans contain low iron concentrations that limit the growth of

phytoplankton. Moreover, it was recently discovered that marine algae blooms, which result from periodic iron deposition from atmospheric dust and flow from the deep ocean, are dominated by pennate diatoms (*Pseudo-nitzshia* and *Fragilariopsis*) that contain ferritin (30). Until recently ferritin has not been identified in any member of the Stramenopiles, a diverse eukaryotic lineage that includes macroalgae, unicellular algae and plant parasites. Through phylogenetic analyses it has been suggested that lateral gene transfer accounts for the occurrence of ferritin in this small subset of diatoms. Storing iron in ferritin is one mechanism that confers a growth advantage, enabling them to better survive the low iron conditions that normally prevail in the oceans. The structure of pennate diatom ferritin from *Pseudo-nitzshia multiseriis* (PmFTN) has been reported and is made up of an assembly of 24 monomers (Figure 1.3) forming a hollow sphere with a diameter of approximately 120 Å, typical of the ferritin family (30).

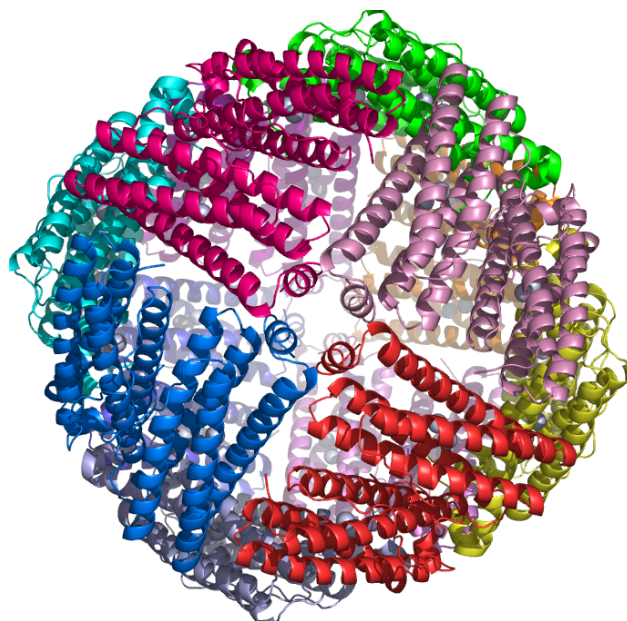


**Figure 1.3.** Crystal structure of *Pseudo-nitzschia multiseriis* ferritin, a 24meric protein. The protein is viewed down one of six four-fold axes. The figure was generated from PDB 3E6R using Pymol (12).

Analysis of mineralisation activity revealed that the protein exhibits ferroxidase activity and was able to support the oxidation of at least 600 Fe(II) per protein, with a Fe:O<sub>2</sub> ratio of ~ 2:1. This indicates that H<sub>2</sub>O<sub>2</sub> is the product of O<sub>2</sub> reduction, a conclusion supported by the regeneration of O<sub>2</sub> upon addition of catalase (30). In order to mimic sporadic blooms as seen in nature, iron limited PmFTN cells were re-supplied with a pulse of iron and immediate growth rate and ferritin transcription increase was seen. When the iron level was depleted it gradually returned to an iron sufficient state. This shows PmFTN ferritin provides protection from oxidative stress by immediately responding to excess iron, as well as iron storage for longer survival (30).

## **1.7 Structural features of PmFTN**

### **1.7.1 Ferroxidase centre and site C**

Ferritin from the diatom *Pseudo-nitzschia multiseriis* is structurally similar to other eukaryotic ferritins. The folded monomers contain 168 amino acids and is similar to eukaryotic, bacterial and archeal ferritin and less related to BFR and Dps ferritins. It also contains three free cysteines that are not usually found in other characterized ferritins. The folded monomer includes four long alpha-helices as well as a short fifth alpha-helix at the C-terminus. The hollow dodecahedron is composed of 24 monomers with a similar highly symmetric arrangement as observed in all other eukaryotic ferritins. The protein is approximately 120 Å across with a molecular mass of ~530 kDa. The residues that form the ferroxidase site in other eukaryotic ferritins are conserved consistent with the catalytic activity observed (31).

The crystal structure of *P.multiseriis* ferritin containing iron revealed iron sites at and near the ferroxidase centre. Site A of the ferroxidase centre did not contain iron but instead contained a water molecule. Site B was fully occupied with iron coordinated by Glu44, Glu48, Glu120 and

Glu 130. Iron was also located at an additional site, termed site C, with 50% occupancy coordinated by one glutamate residue (Glu44). This was a surprising finding because iron binding sites close to the ferroxidase centre have not been observed previously in eukaryotic ferritins. They have been observed in bacterial ferritins in which they are also referred to as site C (30). The site C observed in PmFTN is related to (but distinct from) that of bacterial ferritins, see alignment in Figure 1.4.

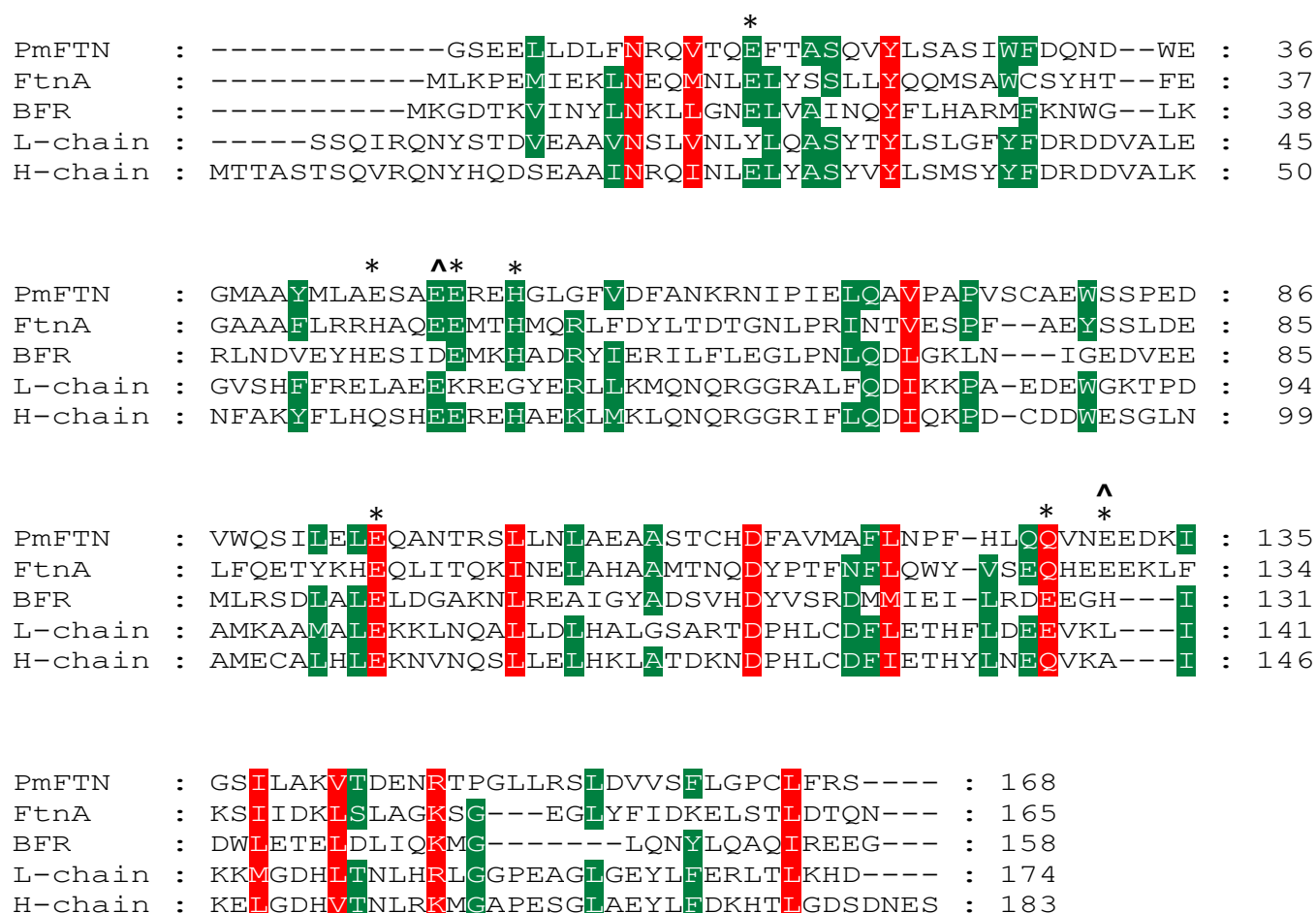


**Figure 1.4.** Amino acid sequence alignment of *Pseudo-nitzschia multiseriis* FTN (PmFTN), FtnA, BFR, *E. coli* and Human L and H chains. Alignment was performed using ClustalW (77) and the figure generated using Genedoc (78). Residue numbers are indicated on the right. Asterisks indicate residues that serve as ligands at the ferroxidase centre of PmFTN and BFR. Black arrow indicates residues that coordinate iron at site C in PmFTN.

A second iron site outside the ferroxidase centre was also observed with lower occupancy than site C which may represent a route for iron from the ferroxidase centre to the cavity (32). The mechanism of iron mineralisation is not understood see Figure 1.5.

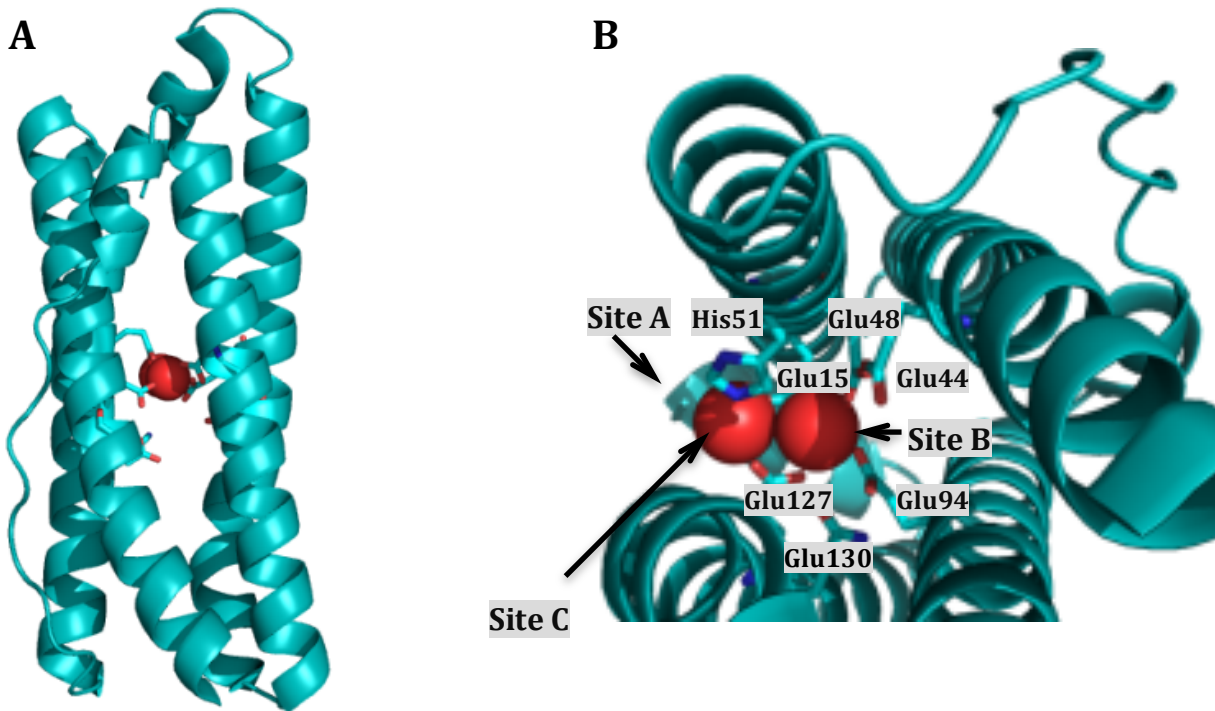


**Figure 1.5.** Ferroxidase site of *Pseudo-nitzschia multiseriis* ferritin. (A) Monomer of  $\alpha$  helices and ferroxidase centre side chains (shown in teal) and iron atoms (shown in red). (B) Ferroxidase centre: site A is occupied by a water molecule (water molecule is not shown here). Iron (shown in red) occupies site B at full occupancy, and is coordinated by four glutamates (Glu44, Glu48, Glu94, and Glu130).

### 1.7.2 Comparison of PmFTN with bacterial ferritin

Bacterial ferritin appears only distantly related to eukaryotic H-chain ferritins in terms of sequence identity (approximately 22%), yet it shares unusual structural similarity to human H-chain. It has the same subunit structure and 24meric arrangement and possesses six 4-fold

channels and eight 3-fold channels. The 4-fold channels are hydrophobic in character in their middle part and polar at both ends. The 3-fold channels are covered by both hydrophobic and hydrophilic residues, but are considerably less polar than their eukaryotic counterparts (8). Bacterial ferritins contain another type of channel first identified in BFR and not present in eukaryotic ferritins (9). These are located where one subunit dimers contacts another (essentially the edges of each of the dodecahedron's 12 faces, hence there are 12 such channels per protein). It is suggested that B-channels might be functionally equivalent to 3-fold channels in eukaryotic ferritins because they are polar in nature. Evidence in support of this is thus far lacking.

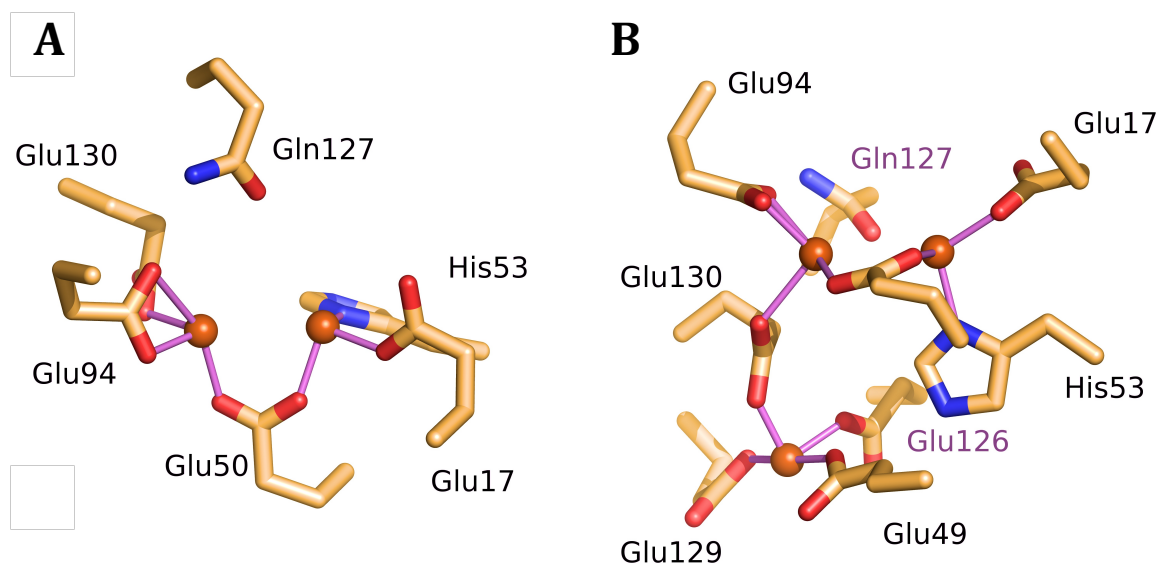


**Figure 1.6.** The ferroxidase centre and Site C of *E. coli* of FtnA. (A) Stick representation of the bridged di-Fe(III) form of the *E. coli* FtnA ferroxidase centre. (B) A rotated view from under the ferroxidase centre showing Fe(III) at the closely lying site C (shown in purple Gln127) (PDB 1EUM).

FtnA, a bacterial ferritin from *E. coli*, has a dinuclear ferroxidase site, where Fe(III) is bound at site A (see Figure 1.6) where it is ligated by monodentate glutamate (Glu17) and histidine (His53) residues and a bridging glutamate (Glu50). At site B, Fe(III) is ligated by Glu50 and two

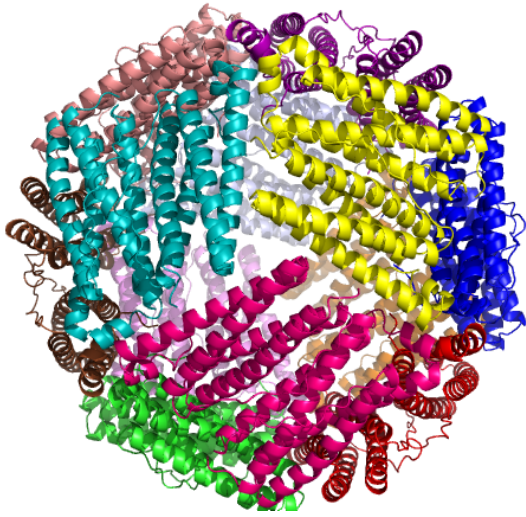
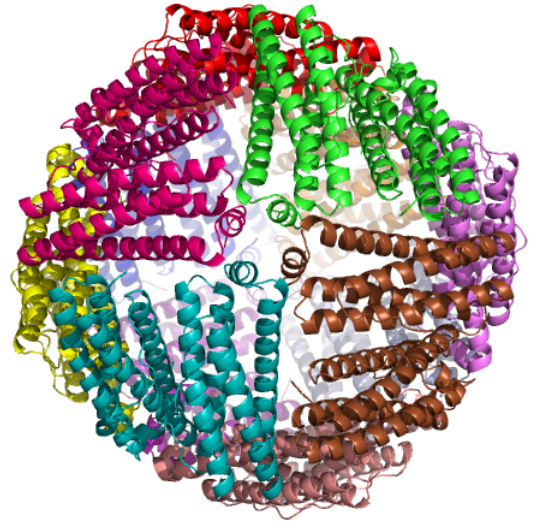
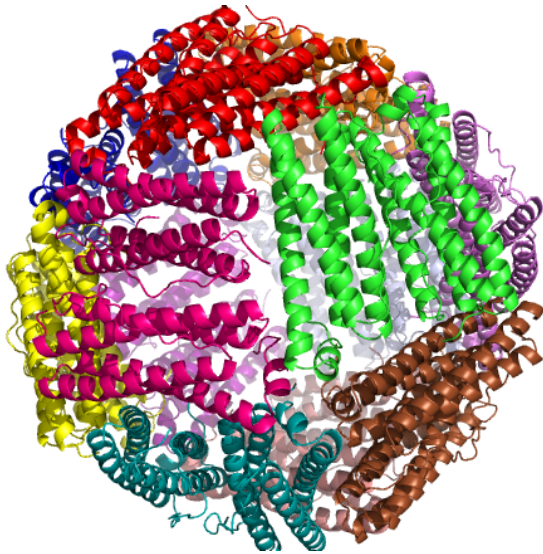
monodentate glutamates (Glu94 and Glu130). Furthermore, a water molecule was coordinated to Fe(III) at site A and a second water bridges the irons, although this is more likely to be an oxo- or hydroxo-bridge (33). Site B occupancy was found to be slightly lower compared to site A. Furthermore, site B coordination resembles that of H-chain ferritin, with one difference: residue Glu61 in human H-chain ferritin is replaced as a metal ligand by Glu130 (8, 9). There is some debate about whether Glu61 is actually a ligand to the iron at site B. In addition, FtnA also has a third iron-binding site, site C, located towards the subunit surface. The iron at this site (Figure 1.6) is coordinated by Glu129, Glu49, Glu130 and Glu126 (8, 9). Mutagenesis of site C residues suggested that site C is not essential for ferroxidase activity, because this resulted in only a slight reduction in oxidation rate. Therefore, site C might not play an important role in the catalysis of Fe(II) oxidation, but could play an important role in determining iron movement into the protein cavity (32, 34).

## **1.8 Bacterioferritin**

Bacterioferritin was first observed in *E. coli* whole cells, in which optical spectra indicated the presence of a heme containing protein that was assumed to be a cytochrome, cytochrome *b*<sub>1</sub> or cytochrome *b*<sub>557.5</sub> (35). Subsequently, a cytochrome *b* protein that contained a large amount of iron was isolated from *Azotobacter vinelandii* (36) and since then BFRs have been isolated from various bacteria such as *Rhodobacter capsulatus* and *Desulfovibrio desulfuricans*. Despite the fact that it contains heme, BFR is a member of the ferritin family of iron-storage proteins and contains 24 identical subunits that are packed together to form the typical highly symmetrical, nearly spherical shell surrounding a central, hollow shell, about 80 Å in diameter. The heme-binding sites are located at the interface between the two subunits that make up each of the 12 faces of the dodecahedron. Hence there are 12 heme-binding sites, see Figure 1.10. The hemes

have bis-methionine axial ligation, with the methionine residues provided by the two separate subunits(37). Bis-Met coordination is highly unusual, with only one other known occurrence, in the surface protein Shp of *Streptococcus pyogenes* (9). In addition to the absorption bands in the visible region that are highly characteristic of heme, bis-Met coordinated heme gives rise to a weak absorption band at ~739 nm due to a LMCT band resulting from the coordination of Met sulfur to iron(III) (38-40).

As in other 24mer ferritins, the symmetrical arrangement of the subunits in BFR results in various channels that connect the inner core with the protein environment. There are eight three-fold symmetry channels, six four-fold symmetry channels and twelve B-channels formed between subunits that are possible entry and exit routes iron (Figure 1.7). The three-fold channel and the four-fold channel are both hydrophilic in BFR, being lined with Asp109, Arg117, and Asp118. Since BFR and eukaryotic H-chain 3-fold channels are very similar, it has been proposed that these channels are the major sites used by ferrous to enter and move to the ferroxidase centre. However, substitution of Asp118 with Ala had a relatively minor effect on mineralisation (41). The four-fold channels are also hydrophilic with four Asn148 residues on the outer surface of the protein shell and four Gln151 residues on the inner surface. B-channels are lined with Asp132, Glu135, Thr136, and Asp139 with Asn34 and Glu66 from different subunits.

**A****B****C**

**Figure 1.7.** The overall structure of *E. coli* BFR. BFR structure looking down (A) a three-fold (B) a four-fold and (C) a B-channel. Figure generated from PDB 1BFR.

### 1.8.1 The ferroxidase centre and inner-surface site

Each BFR subunit includes a dinuclear metal binding site (the diiron site) linking together the four major helices of the subunit, which has been identified as the ferroxidase active site, responsible for catalyzing the oxidation of ferrous iron by dioxygen (2). The BFR ferroxidase centre is distinct from those of other H-chain subunits (see Figure 1.2B and Figure 1.8), in that it is highly symmetrical, projecting a much closer relationship to the centres of class II di-iron proteins, such as ribonucleotide reductase and methane monooxygenase (3, 42). These structural differences result in distinct mechanistic and functional properties. For example, spectroscopic and kinetic studies showed that the oxidised form of the ferroxidase centre of *E. coli* BFR is stable and that the ferroxidase centre is required throughout core formation (2, 43).

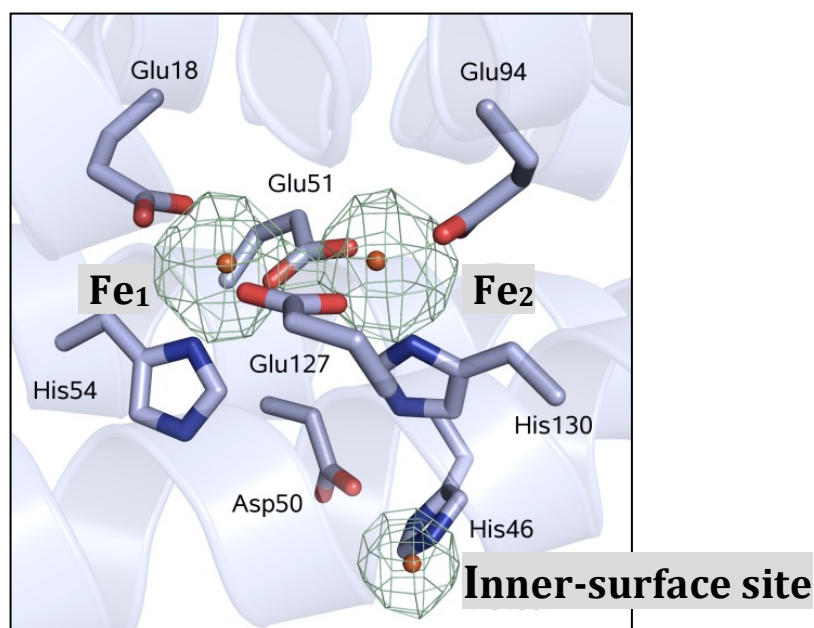


**Figure 1.8.** The ferroxidase centre and inner-surface site of *E. coli* BFR. A stick/cartoon representation of the di-Fe(II) form of the *E. coli* and the inner-surface site where  $\text{Fe}^{2+}$  is coordinated by His46 and Asp50. PDB 3E1M.

The residues forming the di-iron ( $\text{Fe}_1$  and  $\text{Fe}_2$ ) centre of BFR consist of two terminal glutamates (Glu18 to  $\text{Fe}_1$ , Glu94 to  $\text{Fe}_2$ ), and histidines (His55, His130), and two bridging glutamates (Glu51, Glu127) (Figure 1.2B). All of these residues are conserved in the BFR sub-family. The ferroxidase site is capable of binding metals other than iron including zinc, cobalt, and manganese. Studies have shown zinc is a potent inhibitor of iron oxidation activity, and this occurs through the binding of the metal to the dinuclear iron site (9, 41, 44).

Besides the ferroxidase centre, *E. coli* BFR has been shown to possess an additional iron site, located on the inner surface of the protein, approximately 9.2 Å from the nearest ferroxidase centre iron, and 10.2 Å from the second iron, in which ferrous iron is coordinated by an aspartate residue (Asp50) and a histidine residue (His46) (see Figure 1.8 and 1.9). This site is structurally and mechanistically important; kinetic studies of variant proteins containing substitutions of either Asp50 or His46 exhibited significantly impaired iron mineralisation but were unaffected in their ferroxidase centre reaction. The inner surface iron site is believed to be required for the transfer of electrons, derived from  $\text{Fe}^{2+}$  oxidation in the cavity, to the ferroxidase centre (9, 28), see section 1.9.2.

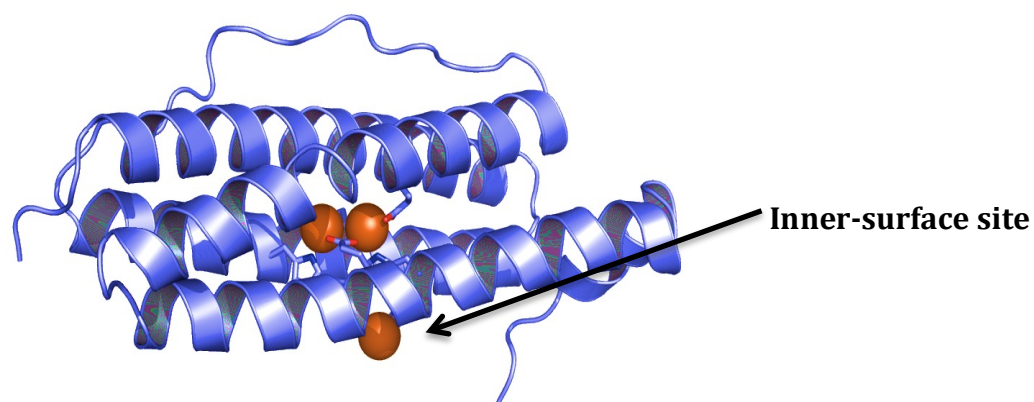


**Figure 1.9** The inner-surface site of *E. coli* BFR. A cartoon representation of the inner-surface site of *E. coli* in which  $\text{Fe}^{2+}$  is below  $\text{Fe}_1$  and  $\text{Fe}_2$ . PDB 3E1M.

## 1.8.2 Heme-binding site

BFR is unique amongst ferritins in that it contains 12 heme-binding sites, and these sites give the protein a characteristic red colour. BFR heme is located at a two-fold symmetric inter-subunit site, where it is sandwiched between two methionine residues (Figure 1.8). The bis-methionine coordination leads to a ligand field strength sufficient to generate the low-spin state of the heme iron. Furthermore, in *A. vinelandii* BFR, heme has a reduction potential which is remarkably low. In the absence of the iron core of the protein, the heme midpoint potential has been measured at pH 8.0 as  $-225$  mV (vs NHE), while in the presence of the iron phosphate core this potential drops to  $-475$  mV. The iron core has a reduction potential of  $-420$  mV which suggests a possible redox interaction between the iron core and heme. The reduction potential of the core is very low indicating that it is hard to reduce. However, the heme potential is lower still, suggesting that it is capable of passing electrons in the the core resulting in reduction of Fe(III) to Fe(II). The reduction potential for the iron-coproporphyrin III that replaces heme in the structure of bound to *D. desulfuricans* BFR was measured to be  $+140$  mV which is much higher than that of *A. vinelandii* BFR (39, 45). The reduction potential of heme bound to *E. coli* BFR has not been reported.

The presence of heme in BFR is an intriguing matter as heme is normally present in proteins as an essential cofactor. For a long time there was a lack of consensus about the functional role for heme in BFR. It has been reported that heme is not required for protein assembly or aerobic oxidative iron uptake, as similar activities were observed for a heme-free variant and the wild type protein (39). Heme-free *E. coli* BFR, obtained by substitution of the methionyl residues that normally bind heme with His or Leu, accumulated, *in vivo*, four times as much iron as compared

to heme bound wild-type protein. Significant accumulations of iron led to the suggestion that heme functions in iron release, and there is now evidence for its involvement in iron release, through mediating the reduction of the iron core (9, 27, 39), see section 1.9.1.

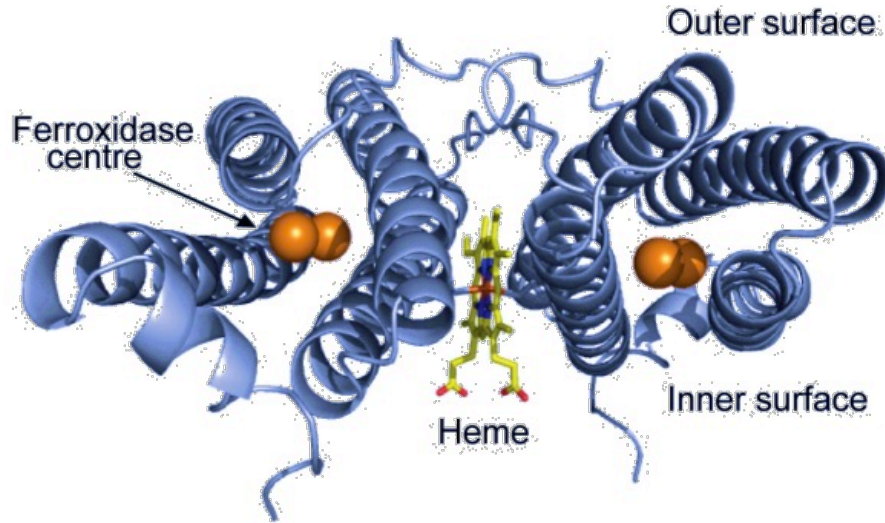


**Figure 1.10.** A cartoon representation of *E. coli* BFR subunits showing the ferroxidase centre, the outer and inner surfaces, and the heme-binding site. The heme is located at an intra-dimer, inter-monomer site and is coordinated by two Met52 residues, one from each subunit PDB 1BCB.

### 1.8.3 The iron mineral core

Like eukaryotic ferritins, BFR from *E. coli* is able to accumulate large quantities of iron, theoretically up to 4500 iron atoms, in the form of an inorganic ferric oxyhydroxide mineral in the central cavity. However, as isolated, the protein from native sources usually contains around 800-1500 iron atoms. This might be related to the fact that BFRs are most efficient at lower iron loading. It has been suggested that, at high iron loadings where there is more iron around to fully load ferritin, the rate of mineralisation is lower due to ferrous oxidation occurring outside of the cavity, competing kinetically with intra-protein oxidation (10). For example noncore oxidation can occur within the protein coat channels that provide access for  $\text{Fe}^{2+}$  into the cavity, potentially blocking  $\text{Fe}^{2+}$  access routes (9, 44).

The mineral cores of native BFR are generally phosphate-rich ‘iron-oxyhydroxide-phosphate’, though, like other ferritins, phosphate is not essential for core formation to occur. The amount of phosphate present in the iron core of BFR is greater than in other ferritins and the phosphate is dispersed throughout the core structure, giving an amorphous and much less dense structure compared to mammalian ferritin cores (46). Furthermore, *in vitro* oxidation of iron in the presence of phosphate allows the incorporation of phosphate into the iron core at levels found in native cores and changes the structural and chemical nature of the core.

## **1.9 Mechanistic aspects of BFR**

### **1.9.1 Mechanism of iron mineralisation**

In BFR, the ferroxidase centre plays an essential role in the mechanism of iron mineralisation (27). Mineralisation of *E. coli* BFR occurs by three kinetically distinct phases. In the first and fastest phase, two  $\text{Fe}^{2+}$  ions enter via an outer pore to each of the flexible 24 pre-organized ferroxidase centres. In the presence of dioxygen or hydrogen peroxide the di- $\text{Fe}^{2+}$  ions are oxidised to  $\text{Fe}^{3+}$ , resulting in a likely hydroxo bridged di- $\text{Fe}^{3+}$  form of the centre along with reduction of dioxygen to hydrogen peroxide or hydrogen peroxide to water. This is phase 2 of the mineralisation process, 48 Fe(II) per 24mer, or 2 per subunits are required to saturate the ferroxidase centres. Fe(II) added in excess of, 48 Fe(II) per protein leads to the formation of an oxyhydroxide mineral core (phase 3) in a reaction that occurs much more slowly than phase 2 oxidation at the ferroxidase centre.

The bridged di-Fe(III) form of the ferroxidase centre is stable. This property makes BFR quite distinct from eukaryotic and bacterial ferritins, in which the oxidised form of the ferroxidase

centre is unstable, with Fe(III) migrating into the cavity. The stability of the oxidised BFR ferroxidase centre raises the question of how it functions in mineralisation. It is apparent that the centre behaves as a true catalytic centre in BFR; it cycles its oxidation state between di-Fe(II) and bridged di-Fe(III) forms and this process drives the mineralisation reaction in the central cavity. Electrons necessary to re-reduce the oxidised form of the centre are derived from Fe(II) oxidation occurring in the cavity.

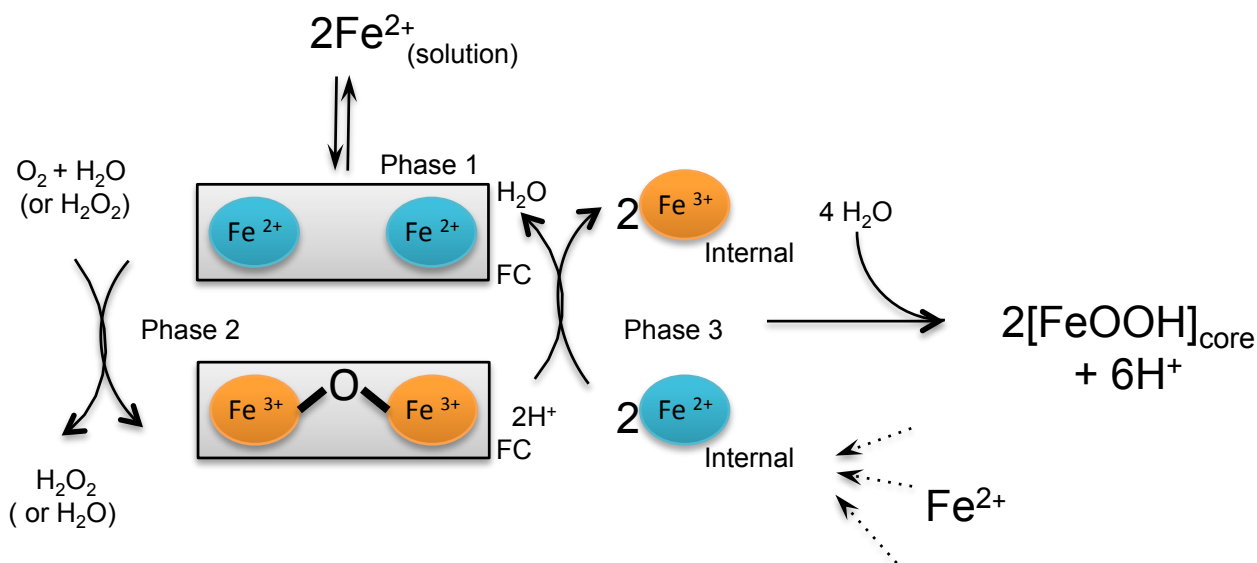


**Figure 1.11.** Mechanism of mineralisation in *E. coli* BFR. This model displays the mechanism of iron uptake which consists of three distinct kinetic phases: phase 1, binding of two  $\text{Fe}^{2+}$  ions per ferroxidase centre (FC), rapid oxidation of the  $\text{Fe}^{2+}$  to  $\text{Fe}^{3+}$  in the presence of dioxygen in phase 2. Phase 3,  $\text{Fe}^{2+}$  bound at the internal, inner site is oxidised, where electrons are channeled to ferroxidase centre then re-reduced. The mechanism continues to operate during the core formation.

Recent studies suggest that inner surface site (see section 1.8.1) is a key constituent of the electron transfer pathway connecting the core to the ferroxidase centre. When  $\text{Fe}^{2+}$  is present in excess of that required to saturate the ferroxidase centre sites, it enters the central cavity, and binds on the inner face of the protein coat at internal nucleation sites. In that particular site,

involving the side chain of Asp50 and His46, the  $\text{Fe}^{2+}$  is approximately 10 Å away from the ferroxidase centre. The  $\text{Fe}^{2+}$  bound at that internal surface site becomes oxidised to  $\text{Fe}^{3+}$  and eventually undergoes a hydrolysis reaction. The electrons from  $\text{Fe}^{2+}$  oxidation in the cavity are channeled to the ferroxidase centre forming a reduced di- $\text{Fe}^{2+}$  of the centre. The generated di- $\text{Fe}^{2+}$  ferroxidase centre can now react again with dioxygen/hydrogen peroxide, perpetuating a catalytic cycle that drives the core mineralisation process (9), see Figure 1.11 for a summary of the mechanism.

In Phase 2, the presence of phosphate does not significantly affect the rate, but in Phase 3, the presence of phosphate significantly enhanced the rate up to five-fold (46). Phosphate is believed to play a role in iron binding and electron transfer at the iron core as shown by studies with *A. vinelandii* BFR (47).

### 1.9.2 Mechanism of iron release

As mentioned above, a major function of BFR is iron storage. An iron store for anabolic processes is only useful if iron can be released from it, as required. The mechanism of how iron is released from the insoluble core of BFR remains unclear.

As for eukaryotic ferritins, iron release from BFR requires a source of electrons and protons, and can be followed using the same kind of chelator assays. Studies of *E. coli* BFR showed that chelators such as pipyridyl and ferrozine are not innocent reporters of iron release, but actually influence (enhance) the rate of iron release, indicating that they must interact with the protein in some way. The use of different reductants showed that electron transfer to the mineral core is the rate-determining step of the release process (27).

The heme groups of BFR have been proposed to be involved in iron release, but evidence for this has been lacking until recently. Studies of BFR containing variable numbers of heme groups revealed that the presence of heme significantly enhanced the rate of iron release, consistent with a role for heme in channeling electrons from the reductant towards the core mineral. Any enhancement in this rate would be expected to increase the overall rate of release. The identity of the physiological reductant for iron release is unclear, but, as for eukaryotic systems, flavins have been suggested as likely candidates and can certainly act as efficient reductants *in vitro*. In many bacteria, the gene encoding BFR is found next to a gene that encodes a small ferredoxin protein called *Bfd* (bacterioferritin-associated ferredoxin) and the expression of *Bfd* is upregulated under low iron conditions, suggesting that this ferredoxin might play a role in iron release (29, 48, 49).

Early studies of *Bfd* from *E. coli* revealed that it binds a [2Fe-2S] cluster with a reduction-midpoint potential of -254 mV, and that it binds specifically to BFR (50). The high resolution structure of a complex between *P. aeruginosa* BFR and *Bfd* showed that *Bfd* binds above the heme groups at an inter-subunit location, with the cluster  $\sim 18$  Å away from the heme iron (49).

### **1.10 Goals of current study:**

1. Iron mineralisation in the recently discovered diatom PmFTN is not well understood. We therefore sought to investigate the catalytic mechanism of iron uptake. This was of particular interest because PmFTN is the first eukaryotic ferritin with a site C located close to the intra-subunit ferroxidase centre (see section 1.7.1). Thus, it was expected that the mineralisation mechanism would be different from that of other eukaryotic ferritins.
2. It was previously shown that heme plays a role in iron release from BFR. However, the

previous study was restricted to samples of BFR containing zero, one or five hemes per BFR. Recently, a novel method for fully loading BFR with heme after purification was devised (51). We sought to establish that the added heme binds at the native heme-binding site and to generate a range of heme loaded BFR samples in order to understand in more detail the role of heme in iron release, and particularly the dependence on heme loading.

## Chapter 2: Materials and Methods

### 2.1 Overproduction and purification of wild-type and M52H BFR

#### 2.1.1 Strains and plasmids

Wild type BFR was expressed from cultures of *E. coli* AL1 (BL21 DE3 *bfr*<sup>-</sup>) containing the plasmid pALN1 (a pET21a derivative containing the *bfr* gene). For M52H BFR, a heme free variant of BFR, *E. coli* JM109 was transformed with pGS758, a derivative of pALTER-Ex1 under the control of a tac promoter.

#### 2.1.2 Preparation of media and growth of cultures

BFR cultures were grown at 37 °C at 200 rpm in Luria-Bertani (LB) media (10 g tryptone, 5 g yeast extract, 10 g NaCl per liter distilled water). On solid media, agar was added to LB (3 g per 250 mL) prior to autoclaving, and poured into 9 cm diameter sterile plates. After autoclaving, a final concentration of 100 µg/mL ampicillin was added. Each flask was inoculated with 2.5 mL of colonies resuspended in LB from agar plates, and grown until the optical density at 600 nm (OD<sub>600</sub>) was 0.4-0.8. At this point wild-type *bfr* gene expression was induced with a final concentration of 1 mM IPTG (Isopropyl-β-D-thiogalactopyranoside) and cultures grown for a further 4 hours. In the case of heme-free BFR (M52H), 0.4 mM IPTG was added and cultures were grown overnight.

#### 2.1.3 Cell harvest and disruption

The cell cultures were harvested by centrifugation at 7,500 rpm for 15 minutes at 4 °C. The resulting supernatant was discarded and the pellet was resuspended in 200 mL of BFR buffer (20 mM HEPES, 100 mM KCl, 0.1 mM EDTA, 10 % v/v glycerol, pH 7.8) and centrifuged as

before. The supernatant was discarded and the wet pellet weighed. Where necessary, the pellet was stored at  $-70\text{ }^{\circ}\text{C}$  until later needed.

The cell pellets were resuspended in a minimal volume of BFR buffer ( $\sim 10\text{ mL}$  per  $1\text{ g}$ ). The sample was divided into  $30\text{ mL}$  aliquots and then sonicated for  $0.2\text{ sec/sec}$  at  $100\text{ watts}$  for  $8\text{ minutes}$  and allowed to cool on ice before sonicating again. Cell debris were pelleted by centrifugation at  $4\text{ }^{\circ}\text{C}$  and  $18500\text{ rpm}$  for  $45\text{ minutes}$ .

#### **2.1.4 Crude purification steps**

The supernatant was heated for  $70\text{-}80^{\circ}\text{C}$  in a metal beaker in a water bath and stirred continuously for  $15\text{ minutes}$ , then rapidly cooled by placing the beaker on ice with continuous stirring. The suspension was centrifuged at  $4\text{ }^{\circ}\text{C}$  and  $18500\text{ rpm}$  for  $45\text{ minutes}$ . The supernatant was collected and stored on ice and subsequently precipitated with ammonium sulphate ( $0.55\text{ g/mL}$ ) at  $4\text{ }^{\circ}\text{C}$  overnight. The resulting suspension was centrifuged as before and the supernatant was discarded. The pellet was resuspended in a minimal volume of BFR buffer ( $\sim 20\text{ mL}$ ), and the resulting solution was dialyzed at  $4\text{ }^{\circ}\text{C}$  against  $500\text{ mL}$  of BFR buffer, with three changes over  $12\text{ hours}$ .

#### **2.1.5 Column chromatography**

A Sephacryl S300 (GE Healthcare) gel filtration column [ $70\text{ x }1.6\text{ cm}$  (bed dimensions)] was equilibrated at  $2\text{ mL/min}$  overnight with  $3\text{ L}$  BFR buffer at  $4\text{ }^{\circ}\text{C}$ . The dialysed protein was loaded onto the column and eluted at  $\sim 2\text{-}3\text{ mL/min}$  using the same BFR buffer. Fractions of  $10\text{ mL}$  were collected using a fraction collector and analysed for BFR content by SDS-PAGE.

A  $5\text{ mL}$  Q-sepharose column (Amersham Biosciences) was equilibrated in five column volumes of BFR buffer at  $1\text{ mL/min}$ . Pooled fractions of BFR were loaded on to the column and the

protein eluted with 1 M KCl in BFR Buffer. Samples were collected in a fraction collector and dialyzed against 0.1 M MES, pH 6.5 at 4 °C with three changes of buffer.

### **2.1.6 SDS-PAGE Analyses**

Samples were taken at various stages of cell growth, harvesting and purification for SDS-PAGE analysis to determine purity as shown in result section. A BioRad gel kit was used to prepare w/v 15% SDS polyacrylamide gels. Sample pellets were resuspended in SDS-PAGE loading buffer (1 M Tris pH 6.8, 200 mM DTT, 20% w/v SDS, 20% v/v glycerol, and a grain of bromophenol blue), boiled for 10 minutes, and centrifuged prior to loading onto the gel. The gel was stained with Coomassie blue (2.5 g Coomassie brilliant blue, 30% v/v methanol, 7% v/v acetic acid, and distilled water per litre), and subsequently destained in 10% v/v Methanol, 10% v/v Acetic Acid, and distilled water.

### **2.2 Removal of iron from BFR to generate apo-BFR**

Iron was removed from BFR by utilizing sodium dithionite as reductant and 2,2'-bipyridyl as a chelator at 4 °C. BFR was dialyzed against 100 mM MES buffer pH 6.2 (freshly prepared in 500 mL deoxygenated Millipore water, sparged for a minimum of 1 hour with dinitrogen) containing sodium dithionite (3 g/100 mL) and a spatula tip of bipyridyl. The reduction/chelator buffer was exchanged 4-5 times over a period of 36 hours. The sample was then dialyzed against 500 mL 0.1 M MES buffer, 0.5 M NaCl pH 6.2 and exchanged 3 times over 24 hours. Finally apo-BFR was dialyzed against 500 mL 0.1 M MES pH 6.2 (3 changes) and 500 mL 0.1 M MES pH 6.5 (3 changes) over a 48 hour period.

### 2.3 PmFTN Samples

*Pseudo-nitzschia multiseris* ferritin protein (wild-type and variants) samples were purified and subjected to iron removal by Stephanie Pfaffen in the laboratory of Prof. Michael Murphy, University of British Columbia, Vancouver. Table 2.1 shows the samples that were supplied. Alkylated samples were treated as described in chapter 3. This resulted in the following samples shown below.

<b>PmFTN Samples</b>	<b>Comments</b>
Wild-type	Alkylated at the three Cys residues to improve protein stability during crystallization study.
Wild-type	Non-alkylated samples
Triple Cys variants	Protein in which all three Cys residues were substituted with Ala
E44H	Alkylated at the three Cys residues to improve protein stability. Glu44 was replaced with His.
E130A	Alkylated at the three Cys residues to improve protein stability. Glu44 was substituted with Ala.
E44Q	Non-Cys residues were substituted with Ala. Also Glu44 was substituted with Gln.

**Table 2.1.** *Pseudo-nitzschia multiseris* ferritin samples used in the iron uptake study.

## 2.4 Protein and iron concentration determinations

Protein concentrations were determined using the bicinchoninic acid (BCA) method (Smith et al., 1985). Bovine serum albumin (BSA) was used as the standard. A calibration curve was attained for the BSA standard to determine the concentration of unknown protein samples. The protein concentration was calculated according to the relationship shown Eq. 2.1. BFR concentration was also determined through absorbance at 280 nm using an extinction coefficient  $33,000 \text{ M}^{-1} \text{ cm}^{-1}$  (2) per subunit. For PmFTN at 280 nm extinction coefficient of  $24,980 \text{ M}^{-1} \text{ cm}^{-1}$  per subunit (30).

$$\text{Unknown concentration} = \frac{\text{Gradient of unknown}}{\text{Gradient of BSA}} \times \text{Concentration of BSA} \quad \text{(Eq. 2.1)}$$

Iron contents of BFR were determined using a colorimetric method. BFR samples with unknown iron content, at appropriate concentration ( $0.5 \mu\text{M}$ ), were placed in 0.5 mL aliquots (in triplicate) into Teflon containers, followed by addition of 0.5 mL concentrated nitric acid (70 % v/v). Each container was sealed into a stainless steel outer jacket and placed in an oven at  $>100 \text{ }^\circ\text{C}$  overnight. A series of ferrous ammonium sulphate standards with a final concentration of 50-250  $\mu\text{M}$  were also prepared from a carefully prepared 5 mM stock solution. 0.4 mL of the iron standard solutions were placed in labeled test tubes and 0.4 mL concentrated nitric acid was added. When the digested protein samples were cooled, 0.8 mL from each Teflon container was placed into a labeled test tube, 0.4 mL of 252 mM sodium ascorbate was added to each test tube (sample and standards) followed by 2 mL of saturated sodium acetate and mixed. Finally, 0.4 mL of 10 mM ferrozine solution was added to each tube and the colour was allowed to develop at room temperature for 15 minutes. Using plastic cuvettes, absorbance at 562 nm was measured.

Absorbance data were plotted as a function of Fe(II) concentration to generate a standard curve. A line of best fit was drawn and the iron concentration of the unknown protein sample was then estimated from the absorbance reading for each unknown sample. The concentration of iron was verified using the extinction coefficient for the [Fe(II)(ferrozine)<sub>3</sub>] complex at 562 nm (28,000 M<sup>-1</sup> cm<sup>-1</sup>) (52).

## 2.5 Spectroscopic and Kinetic Analyses

### 2.5.1 UV-visible absorbance spectroscopy

This technique involves measurement of electronic transitions of samples from their ground state to various excited states. The energy required to promote such transitions lies in the ultraviolet UV (200-400 nm) and visible (400-750 nm) regions of the spectrum. Different types of molecules absorb different frequencies of light providing a means by which they can be distinguished. Types of transitions include  $\pi \rightarrow \pi^*$ , and  $n \rightarrow \pi^*$  (promotion of a non-bonding or lone-pair electron to  $\pi^*$ ). These types of transitions occur in the peptide backbone of proteins and in aromatic amino acid side chains. The d-d and charge-transfer (CT) transitions are also common and are usually highly characteristic of protein cofactors. UV-Visible absorbance is a quantitative technique where absorbance intensity is related to concentration through the Beer-Lambert law, Equation 2.2.

$$A = \log(I_0/I_t) = \epsilon \cdot c \cdot l \quad \text{(Eq. 2.2)}$$

Here A is absorbance (with no units);  $I_0$  and  $I_t$  are, respectively, the radiation incident on, and transmitted by, the sample;  $\epsilon$  is the extinction coefficient (measured in units of M<sup>-1</sup> cm<sup>-1</sup>); c is

the molar concentration of the sample ( $M$ ); and  $l$  is the pathlength (cm) of the sample through which the radiation travels. This enables changes during reactions to be followed quantitatively.

Iron uptake measurements were carried out using a Perkin Elmer  $\lambda$ 35 or  $\lambda$ 800 UV-visible spectrophotometer by following absorbance changes at 340 nm after addition of ferrous iron as a function of time. Data attained were plotted using Origin software (version 7.0 Origin Labs). Increases of absorbance at 340 nm are due to the oxidation of ferrous to ferric iron, resulting in ligand to metal CT bands in the near UV-and visible regions.

### **2.5.2 Stopped-flow experiments**

Fast biochemical reactions that take place in solution over timescales of milliseconds up to tens of seconds are difficult to follow accurately using a conventional spectrophotometer. However, by using rapid mixing stopped-flow, fast reactions can be precisely measured. In the stopped-flow spectrophotometer, two reactants are rapidly mixed in a mixing chamber (approximately 100-200  $\mu$ L). The flow is stopped with the reactant stream in the flow cell. At this point data accumulation in the observation cell begins and changes in absorbance or fluorescence are followed over time. A schematic representation of the stopped flow is shown in Figure 2.1.

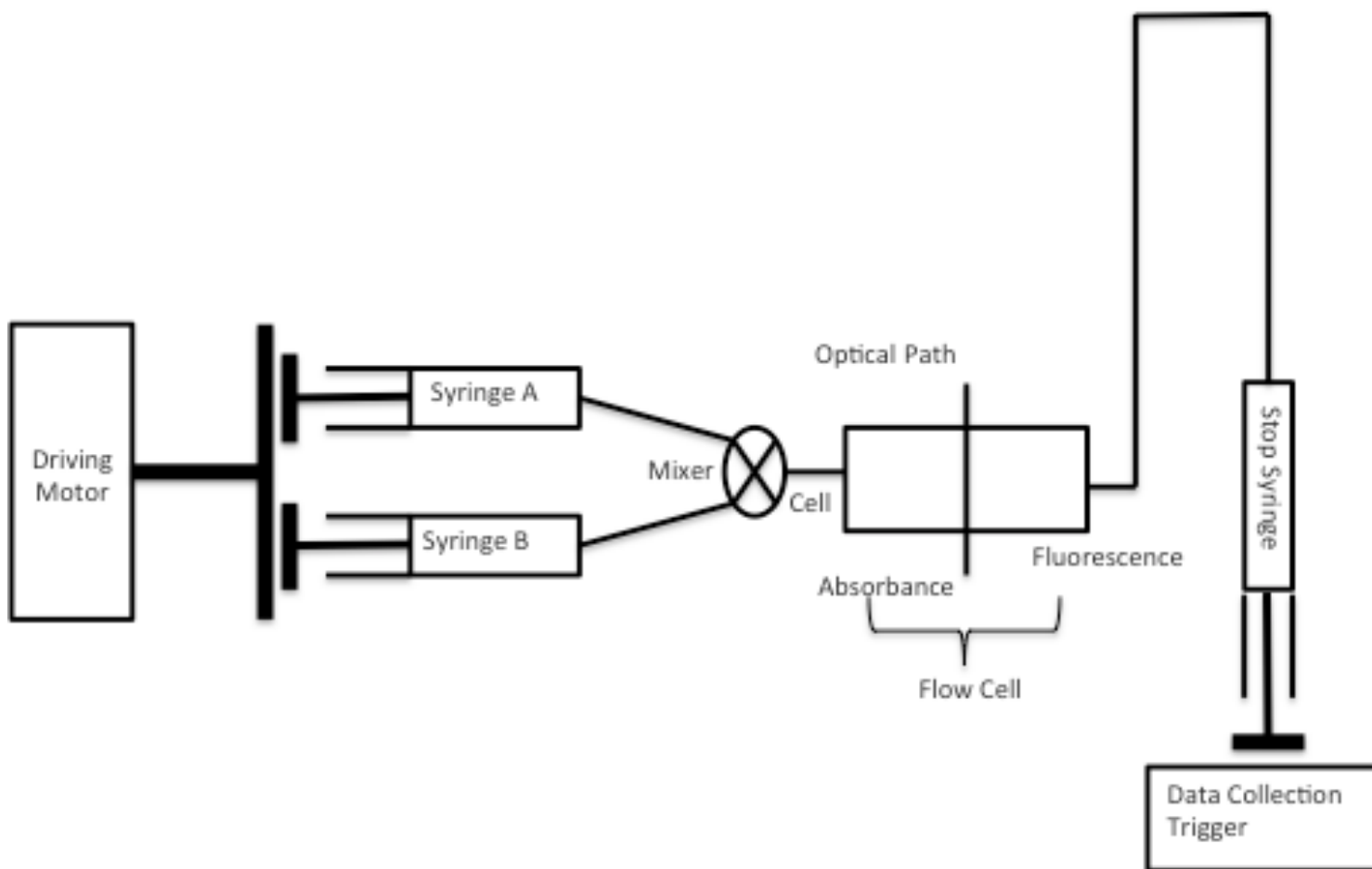


**Figure 2.1.** Schematic diagram of a stopped-flow instrument.

In this study, rapid changes in absorption at 340 nm and  $>500$  ms after the addition of ferrous solution to PmFTN were measured using an Applied Photophysics DX17MV stopped-flow instrument. The collected data was processed by the supplied software and absorbance versus time data files exported into Origin (version 7, Origin Labs) for plotting, fitting and presentation. Data curves were fitted using Origin, either to single or double exponent.

### 2.5.3 Addition of heme to BFR

In overexpressed purified BFR less than stoichiometric amounts of heme are bound to the protein. The numbers of hemes bound to the protein was determined from the absorbance at 280 nm ( $33,000 \text{ M}^{-1} \text{ cm}^{-1}$  per subunit) and at 418 nm ( $109,000 \text{ M}^{-1} \text{ cm}^{-1}$  per heme) (53) with the extinction coefficient indicated. In order to achieve full occupancy of the heme-binding sites, heme was added to the protein. Stock solutions of 1 mM hemin chloride (Sigma) were prepared by dissolving hemin chloride in sodium hydroxide (5 M) and diluting with 50 mM Tris-HCl, 50 mM KCl pH 8 buffer, and quantified by using extinction coefficient,  $\epsilon_{385 \text{ nm}} = 55000 \text{ M}^{-1} \text{ cm}^{-1}$ . After hemin addition to the protein (0.5  $\mu\text{M}$ ) in 0.1 M MES pH 6.5, 1 M NaCl the solution was heated to 80 °C for 10 mins, and allowed to cool to room temperature. Free and adventitiously bound hemes were removed from the protein by passage through a PD-10 desalting column (GE Healthcare), equilibrated with 0.1 M MES, pH 6.5. Absorbance changes were measured using a Jasco 2100 UV-visible spectrophotometer. In the case of M52H BFR, addition of heme to the protein, according to the method described above, led to precipitation of ~25-33 % of the protein when heated at 80 °C. Therefore, it was instead heated to 65 °C.

### 2.5.4 Addition of Fe(II) to apo-ferritin

To mineralize apo-ferritin, a solution of ferrous ammonium sulfate was prepared in deoxygenated pure water (sparged with nitrogen gas for a minimum of 3 hours). Concentrated hydrochloric acid (25  $\mu\text{l}/50 \text{ mL}$ ) was added to prevent auto-oxidation of Fe(II). A micro-syringe (Hamilton) was used to make microlitre additions of the iron stock solution to a cuvette containing aerobic solutions of 0.5  $\mu\text{M}$  BFR (wild type, heme loaded and heme free variant) or PmFTN (wild-type and variants) in 100 mM MES, pH 6.5 at 25 °C. Kinetics of the core

formation process were determined by measuring  $A_{340\text{nm}}$  changes. Fe(II) oxidation was allowed to go to completion and the resulting solution was transferred to an Eppendorf tube and centrifuged at 10,000 rpm for 5 min to remove any Fe(III) precipitate not bound to the protein. The supernatant was carefully transferred back into the cuvette prior to the next addition. Absorbance changes were measured using a PerkinElmer  $\lambda 800$  spectrophotometer.

### 2.5.5 Fe(II) oxidation rate analysis

In order to determine kinetic characteristics of mineralisation (Phase 3), Fe(II) oxidation rates were calculated by drawing a tangent line (shown in Figure 2.2) to the initial linear region of the curve or slope, corresponding to the initial rate of oxidation. The slope of the tangent was calculated, giving the rate.

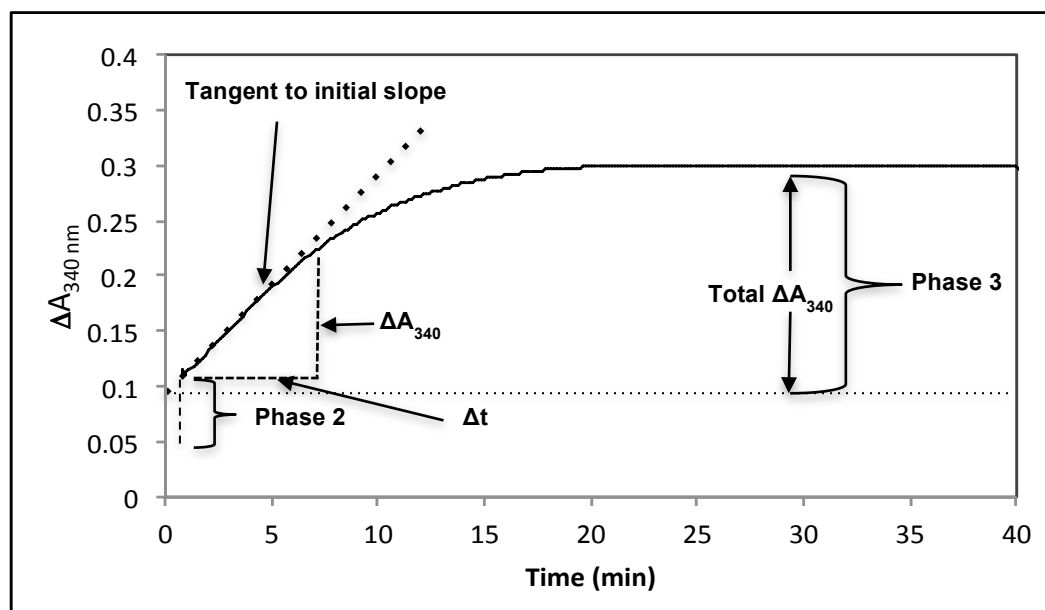


**Figure 2.2.** Rate calculation of Fe(II) oxidation in  $\mu\text{Ms}^{-1}$ .

Calculated rates, in units of  $\Delta A$  at 340 nm per second, were converted to  $\mu\text{M}$  Fe(II) oxidised per second by dividing by the total  $\Delta A_{340\text{nm}}$  which corresponds to the complete oxidation of a known

concentration of Fe(II), and multiplying by that Fe(II) concentration, giving the rate in units of  $\mu\text{M s}^{-1}$  (see Eq. 2.4). Estimates of the error in the determined rates were obtained by drawing alternative tangents describing the outermost acceptable fits of the data, calculating rates and determining standard errors (46).

$$\text{Rate} = \frac{(\Delta A_{340} / \text{Total } \Delta A_{340}) \times \text{Fe (II) concentration}}{\Delta t} \quad (\text{Eq. 2.4})$$

### 2.5.6 Release of Iron from the Core

To study the release of iron, BFR loaded with 1200 Fe(II) was transferred to an anaerobic cabinet (Faircrest) in which  $\text{O}_2$  was maintained at  $<3.0$  ppm, unless otherwise specified. Stock solutions of 50 mM sodium dithionite were prepared and quantified anaerobically by utilizing the extinction coefficient,  $\epsilon_{320 \text{ nm}} = 8000 \text{ M}^{-1} \text{ cm}^{-1}$  (54). A mixed buffer system (referred to as MBS: potassium acetate, MES, Tris, MOPS (all at 10 mM), 200 mM NaCl, pH 6 or 7) was used, and iron release was monitored using the  $\text{Fe}^{2+}$  chelator ferrozine (3-[2-pyridyl]-5,6-diphenyl-1,2,4-triazine-4,4'-disulfonic acid). The progress of the reaction was monitored by following the time-dependent changes in the intensity of the band at 562 nm reporting on the formation of  $[\text{Fe(II)(ferrozine)}_3]^{4-}$  ( $\epsilon_{562 \text{ nm}} = 28,000 \text{ M}^{-1} \text{ cm}^{-1}$ ) (52), indicative of  $\text{Fe}^{2+}$  release. In most cases, the chelator was present at 1 mM and BFR was present at 0.05  $\mu\text{M}$  (containing 1200  $\text{Fe}^{3+}$ ), and assays were conducted in a 1.0 cm path length cuvette equipped, and release initiated by the addition of sodium dithionite via a microsyringe (Hamilton). For iron release experiments with flavin mononucleotide (FMN), generation of the reduced dihydroflavin form ( $\text{FMNH}_2$ ) was carried out using stoichiometric or excess concentrations of sodium dithionite. Assays in MBS were performed at pH 7.0 and 15 °C, with chelator, dithionite (100  $\mu\text{M}$ ), and variable FMN (0–

100  $\mu\text{M}$ ) (27). Absorbance changes were measured using a PerkinElmer  $\lambda$ 800 spectrophotometer. Data were fitted to a single exponential function, yielding a first order rate constant,

# Chapter 3: Mechanistic studies of iron uptake by a pennate diatom ferritin

## 3.1 Study of iron uptake in PmFTN

A novel ferritin was recently discovered in *Pseudo-nitzschia multiseriata*, a marine pennate diatom that is found in algal blooms, which result from periodic iron deposition from atmospheric dust and flow from the deep ocean. Diatoms play a major role in global primary production and carbon sequestration to the deep ocean. Storing iron in ferritin is one mechanism that confers a growth advantage, enabling those that contain a ferritin to better survive the low iron conditions that normally prevail in the oceans. Ferritin from the diatom, referred to as PmFTN, is structurally similar to other eukaryotic ferritins. Three distinct iron binding sites were identified. Sites A and B are located at the conserved ferroxidase active site. The centre is unusual, however, as it contains a third iron site (site C) previously found only in non-heme prokaryotic ferritins. The mechanism of iron mineralisation is not been investigated. During the preparation the cysteine residues were alkylated to improve protein stability. Here, rapid reaction kinetic studies of alkylated and non-alkylated PmFTN were undertaken.

## 3.2 Iron core formation in PmFTN

To examine the protein's ability to store iron, the mineralisation reaction of alkylated wild-type PmFTN was studied by following changes in absorbance at 340 nm upon addition of 400 Fe(II) per apo-PmFTN molecule, see Figure 3.1. Mineralisation involves the binding and oxidation of iron at the inner core, and only occurs (to any significant extent) where Fe(II) exceeds that required to saturate the ferroxidase centre and associated sites. The trace in Figure 3.1 shows

clearly that the PmFTN protein is able to catalyse Fe(II) oxidation. Phase 2 is not observed, due to the experimental set up.

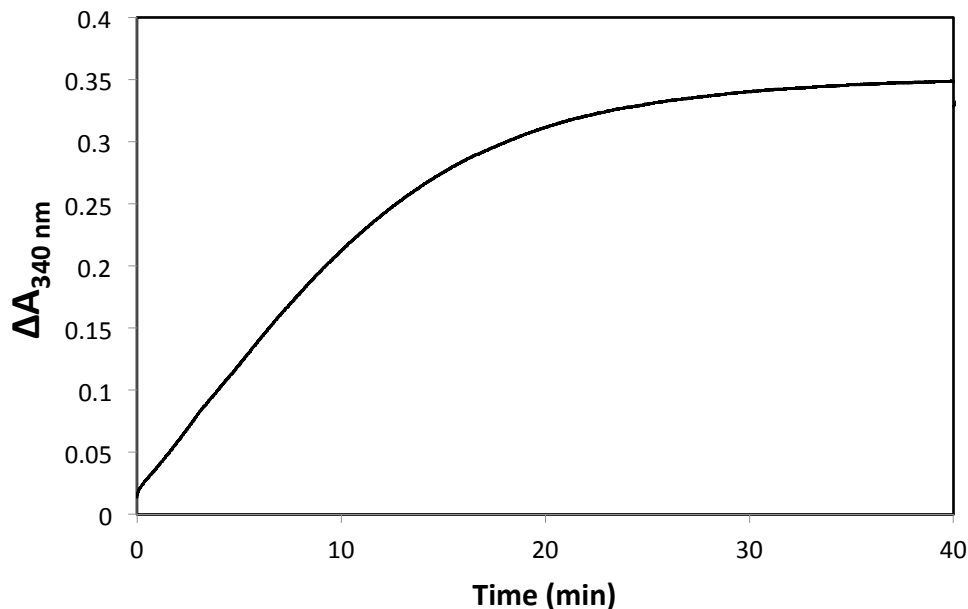


**Figure 3.1.** Absorbance changes at 340 nm showing Fe(II) oxidation in the presence of alkylated 0.5  $\mu\text{M}$  PmFTN in 0.1 MES pH 6.5. 400 Fe(II) ions per PmFTN were added at 25  $^{\circ}\text{C}$  and pathlength 1 cm.

To examine the protein's capacity to store iron, sequential additions of 400 Fe(II) per protein were made to apo-PmFTN see Figure 3.2A. Precipitation was observed in the cuvette after the addition of a total of 1600 Fe(II) ions per PmFTN. The second addition of Fe(II) is oxidised but at a rate that is clearly lower than that for the first addition, and the rate does not increase for subsequent additions. Little of the third addition is actually taken up by the protein (as demonstrated by the large decrease in absorbance following centrifugation of the sample after the third addition). Thus, the protein does not have a high capacity for iron, at least under the conditions tested here. Figure 3.2B shows a plot of the initial rate of Fe(II) oxidation as a function of Fe(II) ions added per PmFTN. It shows a maximum rate at 400 Fe(II) ions. This is

quite different behaviour to ferritins such as BFR, which exhibit a maximum rate at  $\sim 1200$  Fe(II) per protein, and can accommodate 2700 Fe(II) per protein (44). Furthermore, each addition of 400 Fe(II) ions produces a larger absorption response than the previous addition. This does not occur with BFR and could indicate that the form of the mineral core changes significantly during the course of the titration.

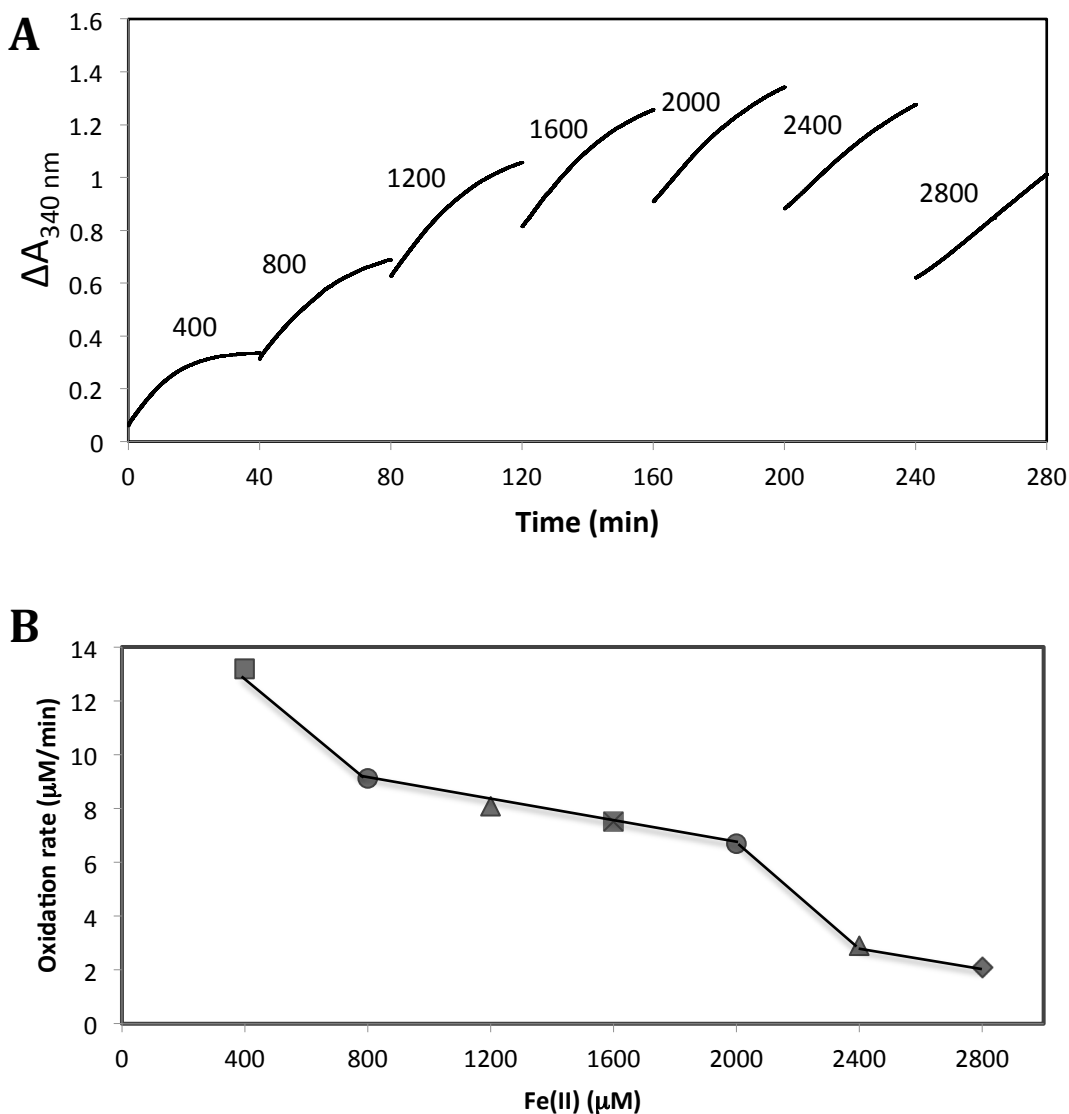


**Figure 3.2.** Iron oxidation catalysed by alkylated wild-type PmFTN. (A) Absorbance changes at 340 nm showing Fe(II) oxidation in the presence of 0.5  $\mu\text{M}$  PmFTN in 0.1 M MES pH 6.5. Numbers indicate total Fe(II) ion additions (sequentially added 400 Fe(II) ions per PmFTN) at 25  $^{\circ}\text{C}$  and pathlength 1 cm. (B) Plot of initial rate of Fe(II) oxidation, catalysed by 0.5  $\mu\text{M}$  PmFTN in 0.1 M MES pH 6.5, as a function of Fe(II) ions added per PmFTN. Rates were calculated as described in chapter 2.

### **3.3 Iron oxidation kinetics at the ferroxidase centre**

To monitor rapid Fe(II) oxidation catalysed by apo-PmFTN, stopped-flow experiments were performed monitoring absorption changes at 340 nm. Figure 3.3 shows absorption changes following mixing of 1  $\mu$ M alkylated wild-type apo-PmFTN in 0.1 M MES buffer at pH 6.5, with various amounts of Fe(II) as function of time. An extremely rapid oxidation of Fe(II) was observed, the oxidation being completed within 0.5 seconds.

For the alkylated protein, a plot of  $\Delta A_{340}$  nm versus Fe(II)/protein, Figure 3.3B, shows that saturation of the initial rapid phase occurred at  $\sim 50$  Fe(II) ions per protein, which is  $\sim 2$  equivalents of Fe<sup>2+</sup> per PmFTN subunit. This amount of iron corresponds to the number of iron atoms required to occupy the dinuclear iron sites. This is consistent with the characteristic of ferritins where the ferroxidase centre is the initial site of rapid Fe(II) oxidation.

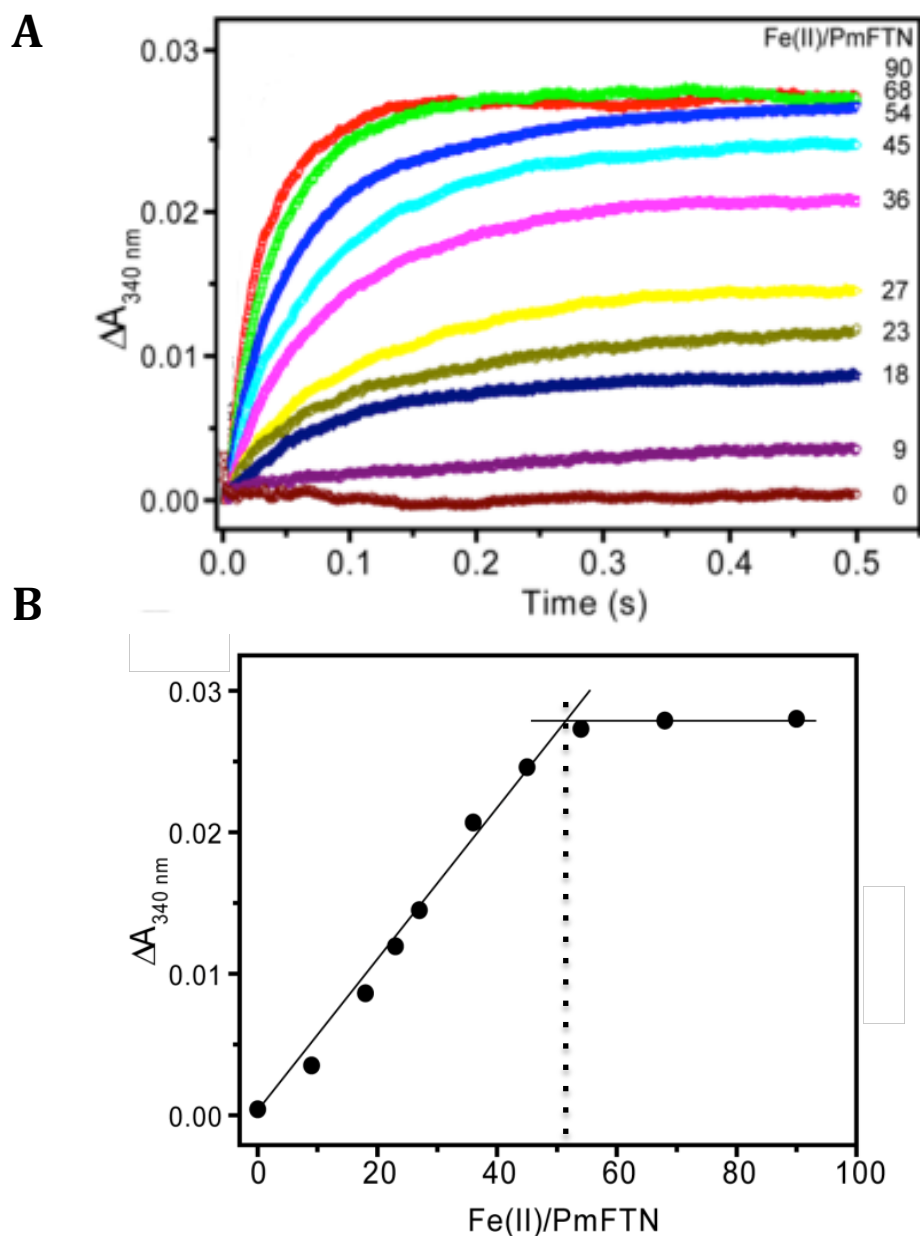


**Figure 3.3.** Kinetic analyses of Fe(II) oxidation catalysed by alkylated wild-type PmFTN (A) Fe(II) was added to final concentrations of 0, 9, 18, 23, 27, 36, 45, 54, 68 and 90  $\mu\text{M}$  to PmFTN wild-type alkylated protein (1  $\mu\text{M}$ ) in MES buffer (0.1 M, pH 6.5, 25  $^{\circ}\text{C}$ ) using a stopped-flow instrument. (B) Final absorbance change after 0.5 seconds of iron oxidation at various ratios of Fe(II)/PmFTN subunit concentration. The two clear phases are highlighted, intersecting at  $\sim 50$  Fe(II) per protein, represented by the dotted line.

Figure 3.4A shows the absorption changes following the mixing of 1.2  $\mu\text{M}$  non-alkylated wild-type apo-PmFTN, in 0.1 M MES buffer at pH 6.5, with various amounts of ferrous iron as a

function of time. Similar to alkylated-wild type it shows a very fast rapid oxidation of ferrous ion. For the non-alkylated protein, a plot of versus Fe(II)/protein, Figure 3.4B, shows that saturation of the initial rapid phase occurred at ~59 Fe(II) ions per protein, which is ~2 equivalents of Fe<sup>2+</sup> per PmFTN subunit which is similar to alkylated protein.

The  $t_{1/2}$  for the oxidation reaction was <50 ms, indicating that the a rate of reaction is an order of magnitude greater than those measured for EcFtnA and Human H ferritin under equivalent conditions (33, 55). Data from the alkylated and non-alkylated PmFTN(Figure 3.5A and Figure 3.6A ) fitted well to a single exponential function, providing for each trace, an observed (pseudo-first order) rate constant,  $k_o$ . Figure 3.5B and Figure 3.6B show a plot of  $k_o$  as a function of Fe(II) concentration. Interestingly, there is a linear relationship, demonstrating a first order dependence of the rate of oxidation on the concentration of Fe(II). This observation is significant because it indicates that Fe(II) binding, rather than Fe(II) oxidation, is the rate-determining step of the reaction, consistent with the unprecedented overall rate of Fe(II) oxidation. For alkylated wild-type PmFTN (Figure 3.4B) the slope of the line provides an apparent second order rate constant,  $k$ , of  $2.59 (\pm 0.12) \times 10^5 \text{ M}^{-1} \text{ s}^{-1}$ . For the non-alkylated wild-type PmFTN the slope of the line gives an apparent second order rate constant,  $k$ , of  $5.61 (\pm 0.02) \times 10^5 \text{ M}^{-1} \text{ s}^{-1}$  (Figure 3.6B). This approximate two-fold increase in the second order rate constant suggests that alkylation of the protein may have a minor effect on the ferroxidase activity of this protein.

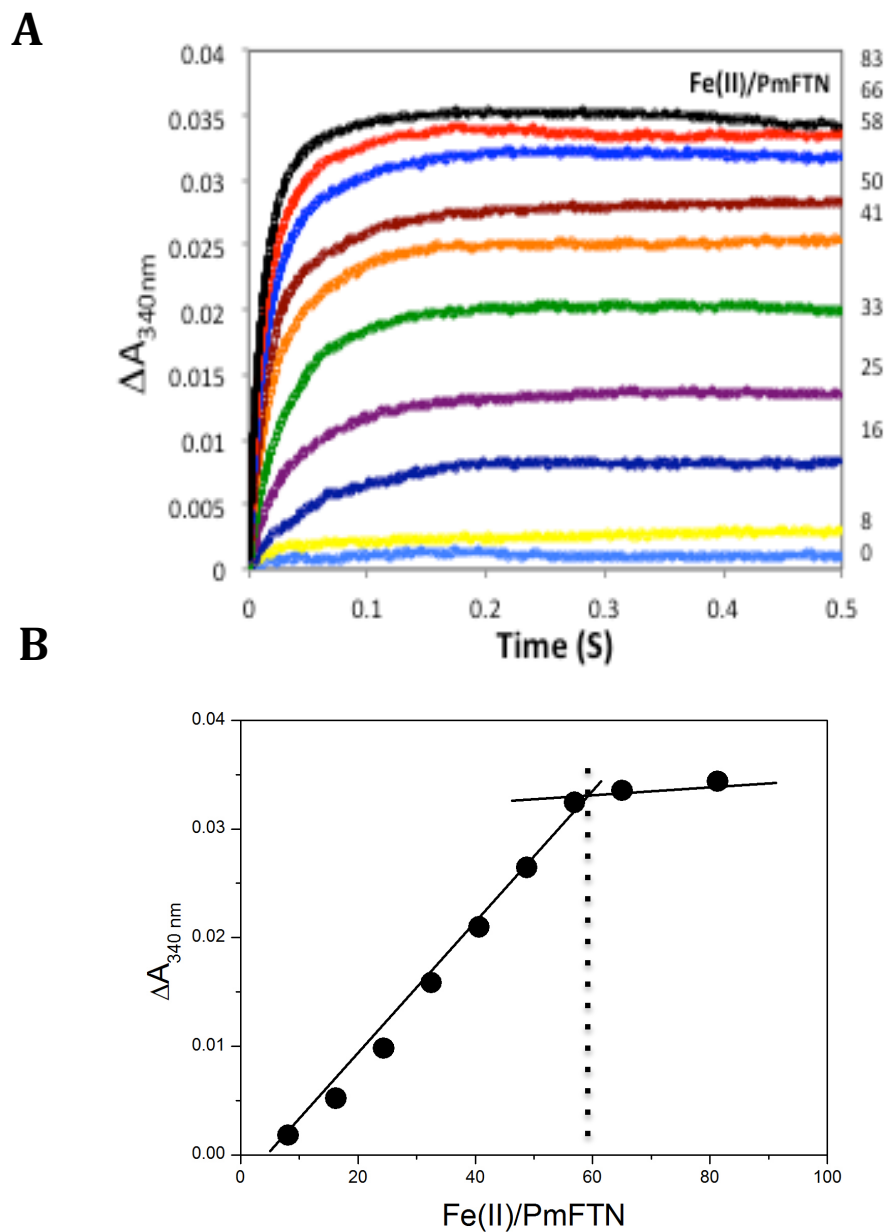


**Figure 3.4.** Kinetic analyses of Fe(II) oxidation catalysed by non-alkylated wild-type PmFTN (A) Fe(II) was added to final concentrations of 0, 10, 20, 30, 40, 50, 60, 70, 80 and 100  $\mu\text{M}$  to PmFTN wild-type alkylated protein (1.2  $\mu\text{M}$ ) in MES buffer (0.1 M, pH 6.5, 25  $^{\circ}\text{C}$ ) using a stopped-flow instrument. (B) Final absorbance change after 0.5 seconds of iron oxidation at various ratios of Fe(II)/PmFTN subunit concentration. The two clear phases are highlighted, intersecting at  $\sim 59$  Fe(II) per protein, represented by the dotted line.

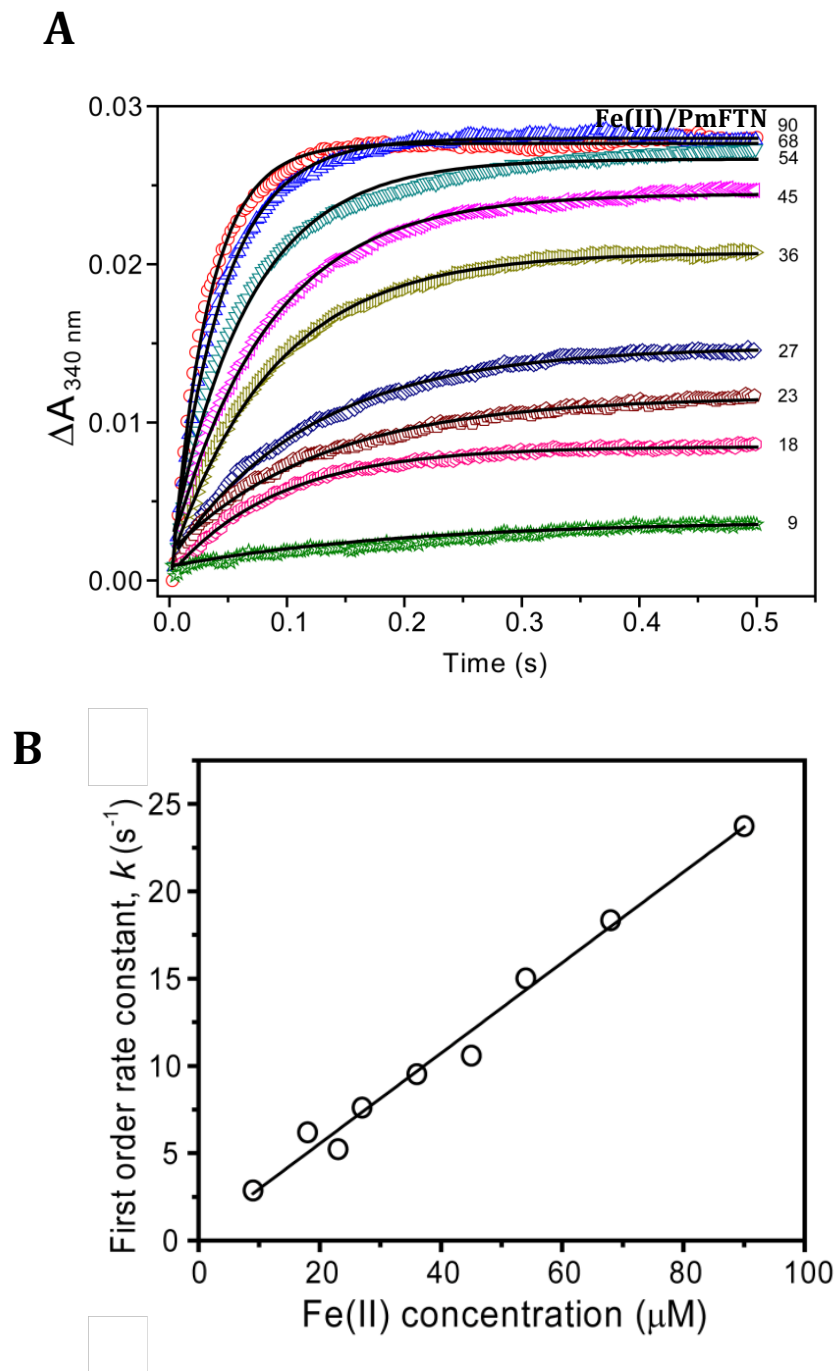


**Figure 3.5.** Kinetic analyses of Fe(II) oxidation catalysed by alkylated wild-type PmFTN (A) Final absorbance change after 0.5 seconds of iron oxidation at various ratios of Fe(II)/PmFTN subunit concentration. Each trace was fitted to a single exponential function. (B) Plot of observed (pseudo-first order) rate constants, obtained from fitting the data in Figure 3.3A, as a function of Fe(II) concentration. A linear fit of the data is drawn in.

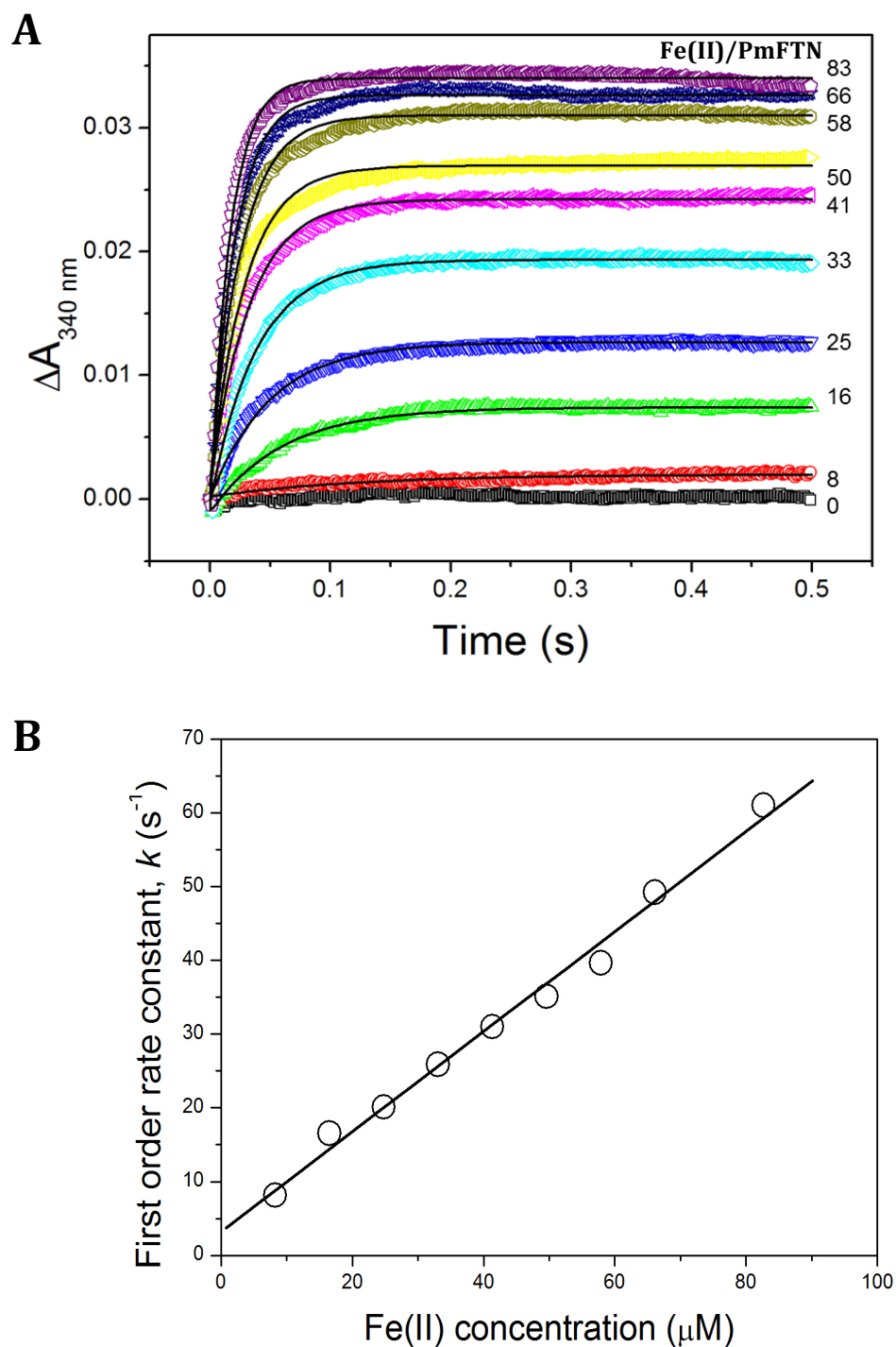


**Figure 3.6.** Kinetic analyses of Fe(II) oxidation catalysed by non-alkylated wild-typePmFTN (A) Final absorbance change after 0.5 seconds of iron oxidation at various ratios of Fe(II)/PmFTN subunit concentration. Each trace was fitted to a single exponential function. (B) Plot of observed (pseudo-first order) rate constants, obtained from fitting the data in Figure 3.4A, as a function of Fe(II) concentration. A linear fit of the data is drawn in.

Figure 3.7 shows absorbance changes for alkylated (3.7A) and non-alkylated (3.7B) following addition of Fe(II) with measurement over a much longer time period. The data demonstrate that absorbance changes continue to occur once the initial rapid ferroxidase centre reaction is complete. Above a level of 50 Fe(II)/protein, this is due to the slower oxidation of Fe(II) present in the excess of that required to saturate the ferroxidase centre. However, absorbance changes also occur below this level, suggesting that further changes in structure occur following oxidation.

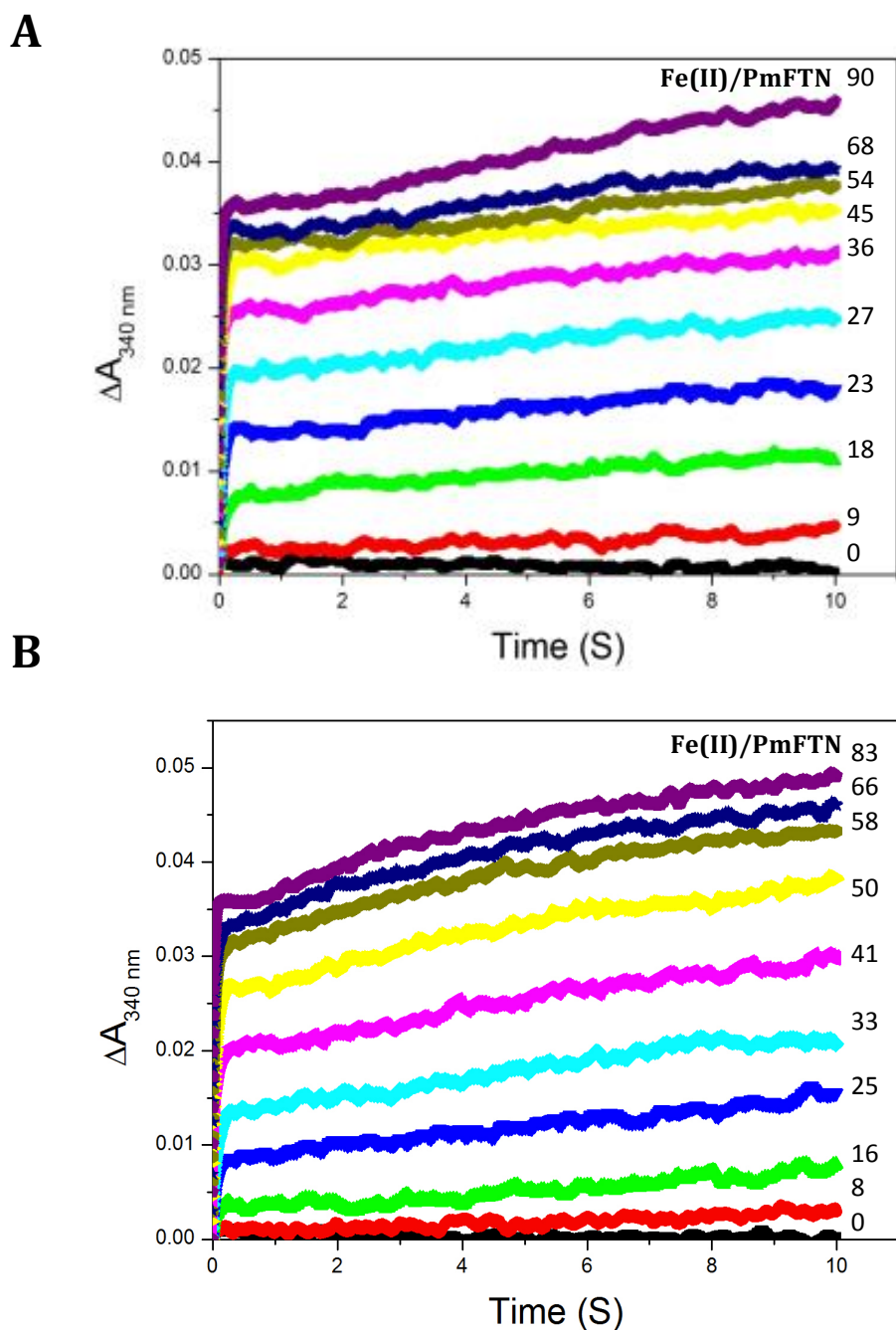


**Figure 3.7.** Kinetic analyses of Fe(II) oxidation catalysed by alkylated (A) and non-alkylated (B) wild-type PmFTN measured over a longer time period. Variable Fe(II) was added (as indicated) to apo-PmFTN wild-type alkylated (1  $\mu\text{M}$ ) and non-alkylated (1.2  $\mu\text{M}$ ) proteins in MES buffer (0.1 M, pH 6.5, 25  $^{\circ}\text{C}$ ) using a stopped-flow instrument.

### 3.4 Regeneration of rapid oxidation in PmFTN

While all ferritins contain a catalytic centre (the ferroxidase centre) that promotes Fe(II) oxidation, ferritins differ in terms of precisely how their ferroxidase centres catalyse mineralisation. In some cases, the di-Fe(III) form of the centre is unstable leading to vectorial transfer of Fe(II) into the protein cavity where it is incorporated into the growing mineral (8). In others, the di-Fe(III) form is stable and the centre functions as a redox active catalytic centre that cycles between di-Fe(II) and di-Fe(III) states. It was of great interest to determine how the ferroxidase centre of PmFTN behaves following Fe(II) oxidation. If Fe(III) at the ferroxidase centres is labile and such that the centre empties of iron following oxidation, it would be expected that the rapid phase of Fe(II) oxidation would be repeatedly observed. To test this, alkylated PmFTN was loaded with 48 Fe(II) per 24mer in the presence of O<sub>2</sub> and then subsequently incubated for 30 minutes or 20 hours. Then, a further aliquot of Fe(II) (either 40 or 80 Fe(II) per protein) was added and changes in A<sub>340</sub> nm were measured. Figure 3.8A shows changes in A<sub>340</sub> nm over 100 seconds after incubation for 30 minutes. Clearly, rapid oxidation is not seen. Furthermore, oxidation is not complete even over the course of 1000 seconds as shown in Figure 3.8B. Samples that were incubated for 20 hours between additions of Fe(II) showed similar behaviour to the 20 minutes incubation samples (the data for 20 hours not shown here). Two distinct phases are observed, though it is not clear what they correspond to. Clearly, the ferroxidase centre did not regenerate an apo-form following oxidation of the initial addition of ferrous iron.

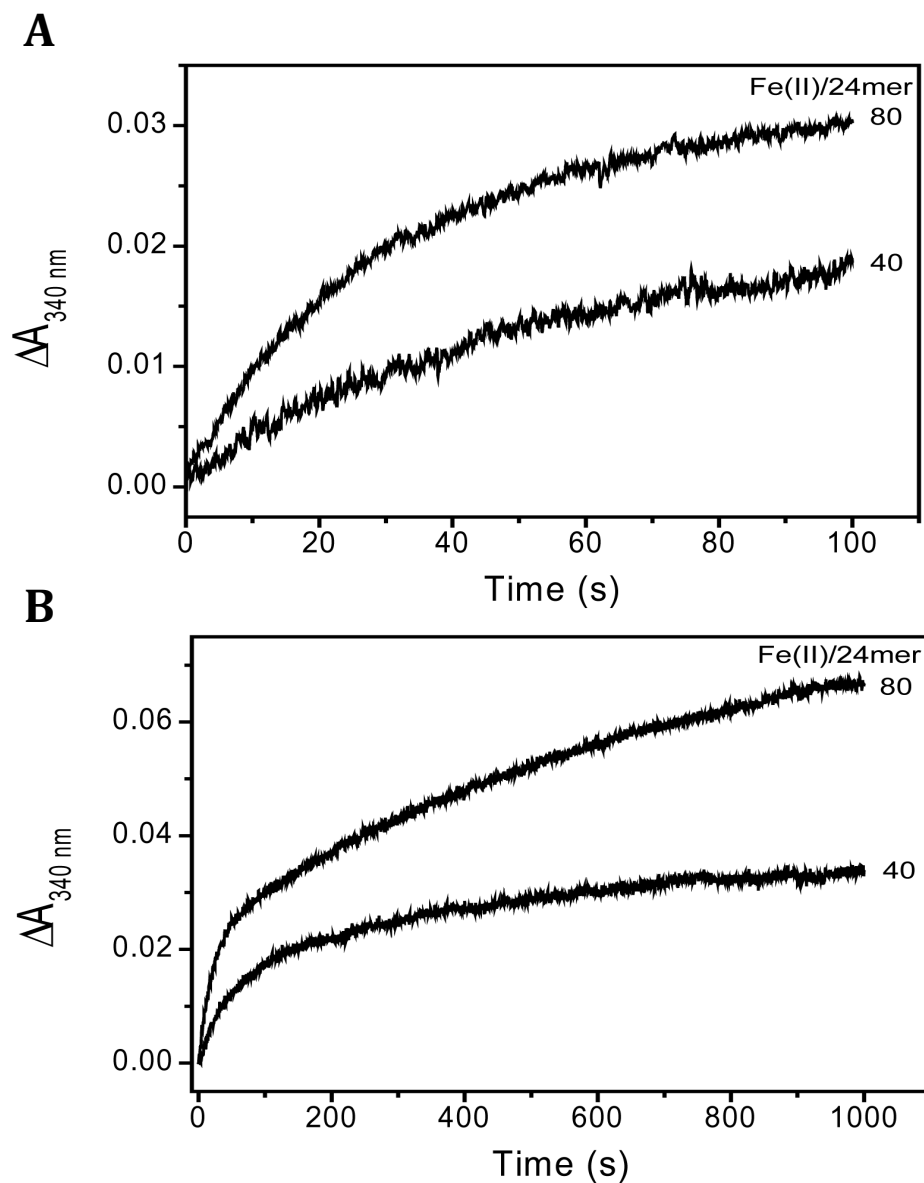


**Figure 3.8.** Kinetic analyses of Fe(II) oxidation catalysed by alkylated wild-type PmFTN. (A) and (B) stopped-flow measurements of absorbance changes at 340 nm following the addition of 40 or 80 Fe(II) ions per protein to a sample of PmFTN previously treated with 50 Fe(II) per protein under aerobic conditions. The incubation time between Fe(II) additions was 30 min. 1  $\mu$ M PmFTN was in 0.1 M MES pH 6.5.

Non-alkylated wild-type PmFTN was also investigated in an equivalent set of experiments.

Figure 3.9A shows changes  $A_{340 \text{ nm}}$  over 100 seconds after incubation for 30 minutes. Again, rapid oxidation is not seen, and oxidation is not complete even over 1000 seconds as shown in

Figure 3.9B. Incubation over 20 hours between iron additions (not shown) showed similar behaviour. The data show that the ferroxidase centre did not regenerate to an apo-form following Fe(II) oxidation. Again, there is only a small difference in behaviour between alkylated and non-alkylated samples.

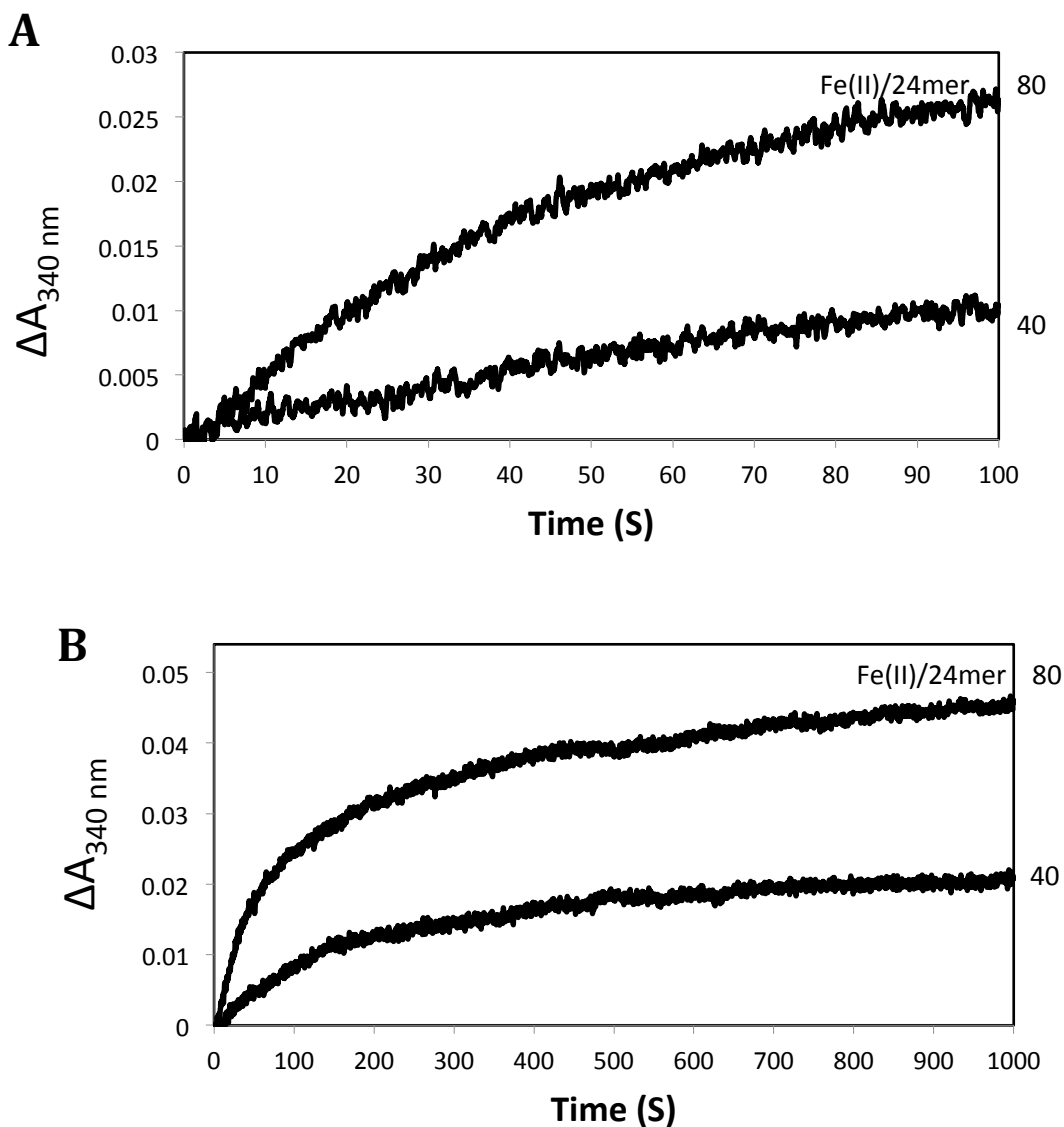


**Figure 3.9.** Kinetic analyses of Fe(II) oxidation catalysed by non-alkylated wild-type PmFTN. (A) and (B) stopped-flow measurements of absorbance changes at 340 nm following the addition of 40 or 80 Fe(II) ions per protein to a sample of PmFTN previously treated with 50 Fe(II) per protein under aerobic conditions. The incubation time between Fe(II) additions was 30 min. 1  $\mu$ M PmFTN was in 0.1 M MES pH 6.5.

### 3.5 The formation of di-Fe(III) peroxy complex formation

In some ferritins, particularly eukaryotic proteins, a di-Fe(III) peroxy species, formed upon transfer of one electron from each Fe(II) to bound O<sub>2</sub>, can be observed through a characteristic transient blue colour (giving absorbance at ~650 nm) (25, 56). Thus, it was of interest to determine whether such a species can be detected during rapid Fe(II) oxidation at the ferroxidase centre of PmFTN. Stopped-flow spectrophotometry was used to monitor changes in absorbance at 650 nm. Figure 3.10A shows 650 nm absorbance changes following mixing the apo-protein with 48 Fe(II) per protein and was monitored to 0.5 seconds where there is no decay of the intermediate. In fact, the intermediate remains even at 2 seconds as shown in Figure 3.10B. In order to check that this absorbance increase does not result from a broad band with a maximum in the 340 nm region, absorbance changes were also measured at 500 nm, see Figure 3.11. Very low intensity changes are observed that are significantly weaker than those measured at 650 nm. Therefore, the band cannot be due to tailing absorbance from the near uv/blue visible region. Data from alkylated PmFTN (Figure 3.10A) fitted well to a double exponential function, providing a rate constant of  $170.1 \text{ s}^{-1}$  ( $\pm 0.0002$ ). This rate constant is higher than that for Fe(II) oxidation which is  $\sim 25 \text{ s}^{-1}$ . These rate constants were obtained under different experimental conditions, so cannot be compared directly. However, the data are consistent with the process at 650 nm occurring more rapidly than the appearance of Fe(III)-O species.

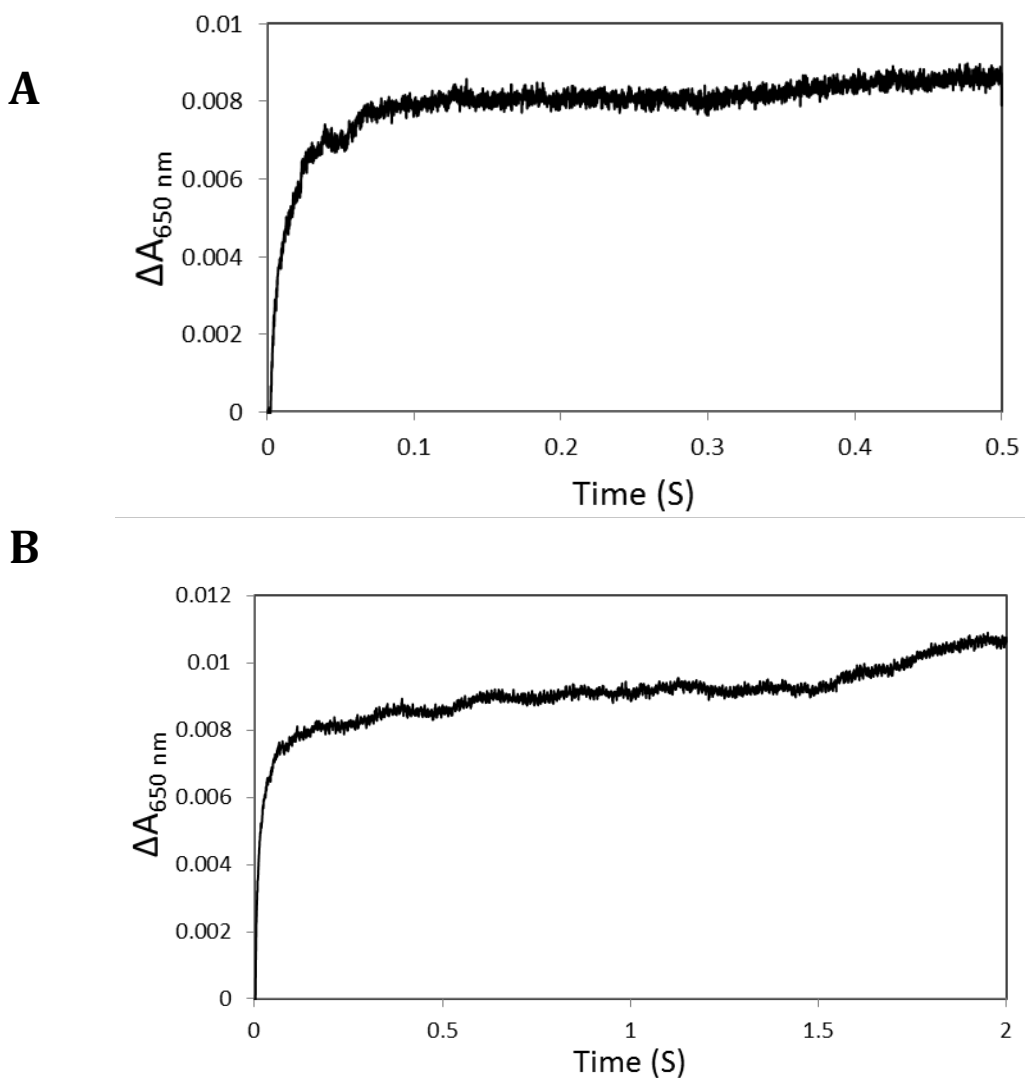


**Figure 3.10.** Stopped-flow kinetic measurements of the formation and the decay of the  $\mu$ -peroxodiferric intermediate following the absorbance changes at 650 nm after the addition of 48 Fe(II) ions per protein to a sample of PmFTN at 0.5 seconds (A) and at 2 seconds (B) 5.94  $\mu$ M alkylated wild-type PmFTN in 0.1 M MES pH 6.5.

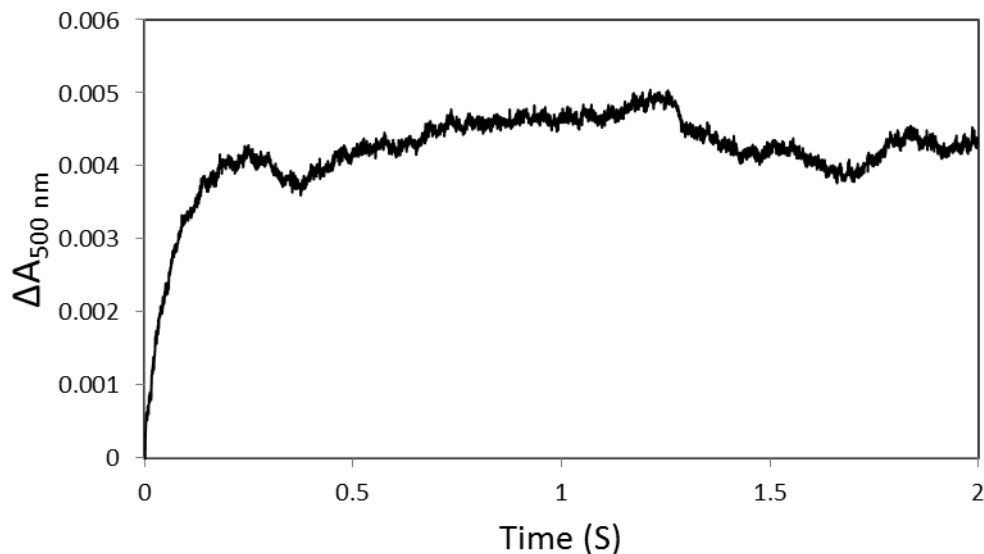


**Figure 3.11.** Stopped-flow kinetic measurements at 500 nm after the addition of 48 Fe(II) ions per protein to a sample of PmFTN (5.94  $\mu$ M) alkylated wild-type PmFTN was in 0.1 M MES pH 6.5.

### 3.6 Discussion

Ferritin are important iron storage and detoxification proteins that are widely distributed in living kingdoms. A ferritin recently found in a marine pennate diatom, unusually possesses a ferroxidase site and a site C and was therefore of interest. In the present study, it is shown that PmFTN can store iron and kinetic measurements of iron oxidation showed an exceedingly rapid initial oxidation phase involving the binding and oxidation of two Fe(II) ions per subunit. To facilitate crystallization of the PmFTN protein, cysteine residues of the protein were alkylated to prevent oxidation. There was no significant variation in behaviour between PmFTN with alkylated and non-alkylated cysteine residues. The ferroxidase centre oxidation reaction is a second order reaction that is dependent on the concentration of Fe(II), indicating that iron binding and oxidation are closely linked such that they cannot be easily distinguished. Since oxidation occurs immediately after Fe(II) binding to PmFTN, the binding event can be viewed as

the slow step of the reaction. This finding is in contrast to previous reports of ferritins, in which binding and oxidation are considered to be kinetically distinct phases with oxidation occurring much more slowly (28). Measurement of Fe(II)-binding kinetics is not generally straightforward. In *E. coli* BFR the presence of heme groups facilitated detection of Fe(II) binding, as it caused a perturbation of absorbance due to the heme, enabling iron binding and oxidation steps to be distinguished, revealing that Fe(II)-binding occurred on a much shorter timescale than the subsequent Fe(II) oxidation (57). In comparison, Fe(II) binding to BFR occurred with a second order rate constant of  $2.5 \times 10^5 \text{ M}^{-1} \text{ s}^{-1}$  (at 30 °C) (58), a value similar to that measured here (at 25 °C) for PmFTN catalysed Fe(II) oxidation.

A previous study has shown that the ferroxidase centre reaction of PmFTN consumed dioxygen in a ratio of  $1.9 \pm 0.2 \text{ Fe(II):O}_2$  (30). Furthermore, addition of catalase to the assay solution resulted in the stoichiometric regeneration of one  $\text{O}_2$ , per two original diFe(II) centres, indicating the production of  $\text{H}_2\text{O}_2$  by the ferroxidase reaction, as seen with many ferritins, (30) but not with BFR (20) or DPS ferritin (2). This is different to the oxidation stoichiometry of *E. coli* FtnA, in which the  $\text{Fe(II):O}_2$  consumption ratio was 3-4 (55). This was found to be due to the binding of three iron atoms, two at the ferroxidase centre and one at the site C (and a potential fourth iron at an unknown metal site) leading to the reduction of  $\text{O}_2$  to water instead of  $\text{H}_2\text{O}_2$ . The *E. coli* FtnA ferroxidase reaction is similar to that seen in human H-chain ferritin, yet is more complex due to present of the third iron in site C (33). However, in *E. coli* FtnA site C is not required for ferroxidase activity; studies of site C variants showed only a slight decrease in the overall oxidation rate with a change in the  $\text{Fe(II):O}_2$  ratio to 2. The data presented here showed that only two Fe(II) ions are initially bound and oxidised per PmFTN subunit and site C is not occupied during the initial oxidation reaction. An important structural difference in PmFTN is that site C is

only 3.5-3.7 Å from site B, compared to 7-8 Å in EcFtnA. Also, a third iron binding site was detected site in EcBFR and human mitochondrial ferritin (59, 60). However, these iron sites were seen to be at the inner surface and are more likely involved in the nucleation/mineralisation reaction rather than in ferroxidase centre catalysed iron oxidation (61).

PmFTN crystals soaked in Fe(II) solution under anaerobic conditions revealed that site A is occupied by ferrous iron (30). Soaking experiment under aerobic conditions showed that iron is observed at all three sites in a time-dependent manner. The data from crystallographic studies demonstrates that, in the absence of O<sub>2</sub>, Fe(II) only binds at site A of the ferroxidase centre. Occupation of sites B and C occurs only following oxidation of Fe(II) to Fe(III). The stopped-flow data presented shows saturation of the rapid phase 2 at a level of two Fe(II) ions per monomer of PmFTN. Together these results indicate a likely stepwise binding of the Fe(II) and O<sub>2</sub> to ferroxidase sites. A possible mechanism is one in which ferrous iron binding to site A is followed by the binding of the oxidant. Binding of the second ferrous iron to site B, occurs only when O<sub>2</sub> is bound. A similar mechanism was proposed for the two Dps proteins from *B. anthracis*. They are mini-ferritins with a 12mer structure that contains inter-subunit dinuclear ferroxidase centres that are distinctive from those of maxi-ferritin 24mers, but regardless share some common features (62). Such a mechanism accounts for the observed rate dependence, because once the second Fe(II) binds, oxidation can occur immediately. Therefore, Fe(II) binding to site B of the ferroxidase site is suggested to be the rate determining step, with binding and oxidation events intimately connected.

So far two general models have been suggested for the mechanism of iron uptake in ferritins. In the first model, as observed in human H ferritin (63), EcFtnA (64), and frog M ferritin (65), the ferroxidase site function as a substrate site. Fe(II) ions binds to the ferroxidase site, becomes

oxidised and the resulting Fe(III) ion rapidly migrates to the mineral core. In the second model, the ferroxidase site is a stable di-iron site that functions as a cofactor after the binding of two equivalents of Fe(II) ion per subunit, as seen in EcBFR (59) and *P. furiosus* ferritin (66). The ferroxidase site functions exclusively in oxygen or peroxide reduction, and additional Fe(II) ions are then added directly to the mineral core and oxidised with resulting electrons re-reducing the ferroxidase centre. Recently, it was suggested that a unifying mechanism, in which the Fe(III) product at the ferroxidase site remains bound to the ferroxidase site but is rapidly displaced by incoming Fe(II) could account for the behaviour of all ferritins (67). This unifying mechanism could possibly explain the observation of a fully Fe(III) loaded ferroxidase site in crystals after an extended soaking in Fe(II) (57). However, the ferroxidase site of PmFTN was not fully occupied after soaking aerobic crystals in ferrous iron for 45 min, suggesting that iron movement occurred at the ferroxidase site during iron loading with 2 mM ferrous iron over prolonged time period (57). Immediately following oxidation of Fe(II) at the ferroxidase centre small absorbance changes were observed which are consistent with the idea that the di-Fe(III) from of the centre is unstable, leading to occupation of site C. The rapid ferroxidase centric-catalysed oxidation of ferrous iron in PmFTN was not regenerated upon incubation up to 20 hours, specifying that at least some iron remains present at the ferroxidase site. Thus, if Fe(III) is displaced, the subsequent iron oxidation is much slower than the initial oxidation. The mechanism of mineralisation in PmFTN appears to be more complex than either of the two general mechanisms outlined above with partial iron migration to the core. The two distinct kinetic phases observed after the second addition of 48 Fe(II) iron may also be associated with slow iron migration to the core, likely involving the third iron binding site (site C). In frog ferritin, the transit of Fe(III) from the ferroxidase centre to the cavity has been observed to occur via a pathway through the

subunit towards a four-fold channel (26). Site C may function to direct Fe(III) along a different path to the mineral core.

## Chapter 4: Mechanistic studies of iron mineralisation variants of diatom ferritin

### 4.1 Non-Cys variant of PmFTN

Protein crystallography required alkylation of free accessible Cys thiol residues to prevent slow oxidation. An alternative to alkylation is simply to remove the Cys residues altogether. A variant of PmFTN was generated, in which all three naturally occurring Cys residues are replaced with Alanine. The properties of such a non-Cys variant of PmFTN are examined here.

To examine the capacity of the non-Cys variant of PmFTN to store iron, sequential additions of 400 Fe(II) ions to PmFTN were made. Figure 4.1A shows absorbance changes at 340 nm as a function of time following sequential additions of 400 Fe(II) ions to apo non-Cys PmFTN.

Precipitation was observed in the cuvette after the addition of a total of 1600 Fe(II) ions per PmFTN. Figure 4.1B shows a plot of the rate of Fe(II) oxidation as a function of Fe(II) ions added per non-Cys PmFTN. It shows a maximum initial rate at around 800 Fe(II) ions, which is different from alkylated wild-type PmFTN, which shows a maximum initial rate around 400 Fe(II) ions.

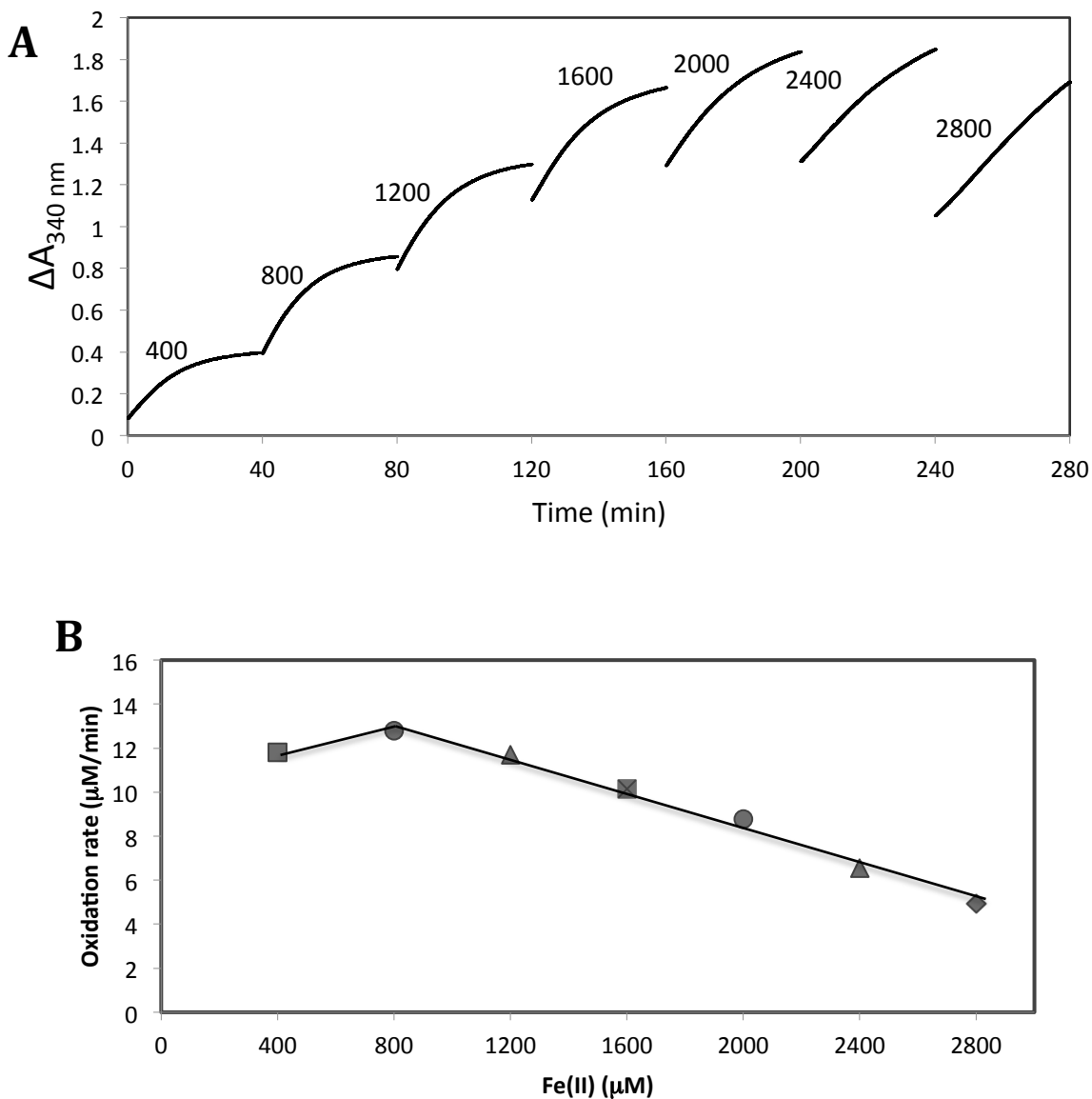


**Figure 4.1.** Iron mineralisation in non-Cys PmFTN. (A) Absorbance changes at 340 nm showing Fe(II) oxidation in the presence of 0.5  $\mu\text{M}$  PmFTN in 0.1 MES pH 6.5. Numbers indicate total Fe(II) ion additions (sequentially added 400 Fe(II) ions per PmFTN) at 25 °C and pathlength 1 cm. (B) Plot of rate of Fe(II) oxidation, catalysed by 0.5  $\mu\text{M}$  PmFTN in 0.1 MES pH 6.5, as a function of Fe(II) ions added per PmFTN.

#### 4.1.1 Fe(II) oxidation kinetics at the ferroxidase centre

A stopped-flow instrument was used to measure the kinetics of Fe(II) oxidation after addition of ferrous ammonium sulphate to apo-non-Cys PmFTN by monitoring absorption change at 340 nm. Figure 4.2 shows the absorption changes following the mixing of 1.2  $\mu\text{M}$  apo-non-Cys PmFTN, in 0.1 M MES buffer at pH 6.5, with various amounts of ferrous iron as function of time, as indicated. An extremely rapid oxidation of ferrous ion was observed similar to wild-type alkylated and non-alkylated PmFTN (see chapter 3), the oxidation being completed within 0.5 seconds. Similar to the wild-type protein a clear saturation is seen as the change in absorbance at 340 nm reaches a maximum when  $\sim 55$  Fe(II) ions per protein, i.e.  $\sim 2$  equivalents of  $\text{Fe}^{2+}$  per PmFTN subunit are added (Figure 4.2B). Each of the kinetic traces at 340 nm fitted well to a single exponential function (Figure 4.2C) providing an observed (pseudo-first order) rate constant,  $k_o$ . Figure 4.2D shows a plot of  $k_o$  as a function of Fe(II) concentration. As in the case of wild-type (alkylated) PmFTN, there is a linear relationship, demonstrating a first order dependence of the rate of oxidation on the concentration of Fe(II). This indicates that Fe(II)-binding, rather than Fe(II) oxidation, is the rate-determining step of the reaction. The data for non-Cys PmFTN, Figure 4.2D, gives an apparent second order rate constant,  $k$ , of  $6.70(\pm 0.25) \times 10^5 \text{ M}^{-1} \text{ s}^{-1}$ , which is slightly higher than that for the alkylated wild-type protein.

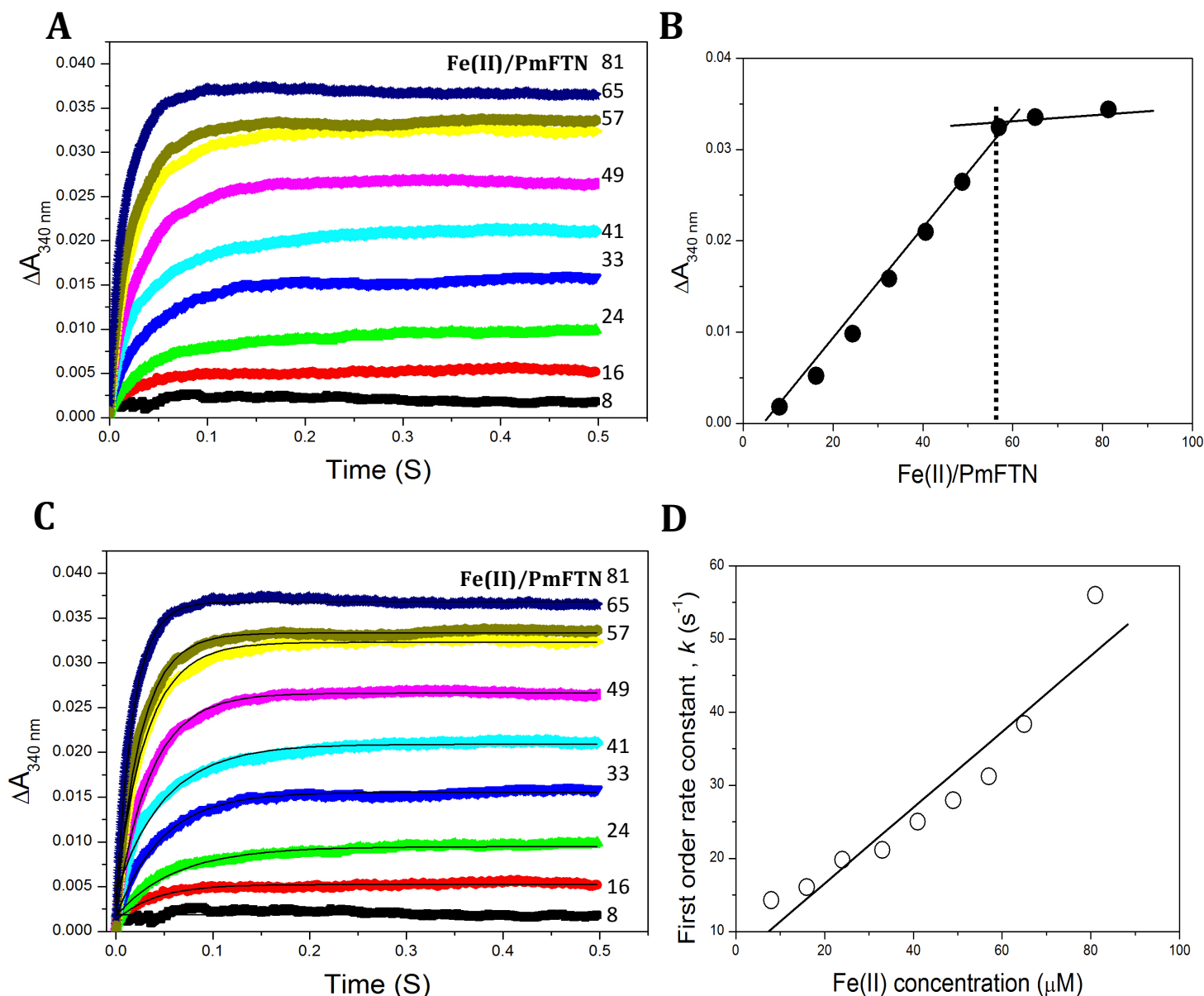


**Figure 4.2.** Kinetic analyses of Fe(II) oxidation catalysed by non-Cys PmFTN (A) Fe(II) was added to final concentrations of 0, 10, 20, 30, 40, 50, 60, 70, 80 and 100  $\mu\text{M}$  to PmFTN non-Cys (1.2  $\mu\text{M}$ ) in MES buffer (0.1 M, pH 6.5, 25  $^{\circ}\text{C}$ ) using a stopped-flow instrument. (B) Final absorbance change after 0.5 seconds of iron oxidation at various ratios of Fe(II)/PmFTN subunit concentration. The two clear phases are highlighted, intersecting at  $\sim 55$  Fe(II) per protein, represented by the dotted line. (C) Fitting of PmFTN-catalysed Fe(II) oxidation data. Each of the A<sub>340 nm</sub> traces corresponding to additions of 8 – 81 Fe(II) ions per PmFTN were fitted to a single exponential function. The solid line fits are shown along with the data from part A. (D) Plot of observed (pseudo-first order) rate constants, obtained from fitting the data in A, as a function of Fe(II) concentration. A linear fit of the data is drawn in.

### 4.1.2 Regeneration of rapid oxidation in PmFTN

To examine whether the extremely rapid oxidation of Fe(II) observed upon addition of 48 Fe(II) per PmFTN can be regenerated, non-Cys PmFTN was loaded with 48 Fe(II) per 24mer in the presence of O<sub>2</sub> and then subsequently incubated for 30 minutes or 20 hours. Then, a further aliquot of Fe(II) (either 41 or 83 Fe(II) per protein) was added and changes in A<sub>340</sub> nm were measured. Figure 4.3A shows changes A<sub>340</sub> nm over 100 seconds after incubation for 30 minutes. Clearly, rapid oxidation is not seen. Furthermore, oxidation is not complete even over 1000 s as shown in Figure 4.3B. The incubation over 20 hours showed similar behaviour to the 30 minutes incubation (not shown). Two distinct phases are observed. As for (alkylated) wild-type protein, it is not clear what they correspond to. Clearly, the ferroxidase centre did not regenerate an apo-form following oxidation of the initial addition of ferrous iron, similar to wild-type alkylated and non-alkylated PmFTN.

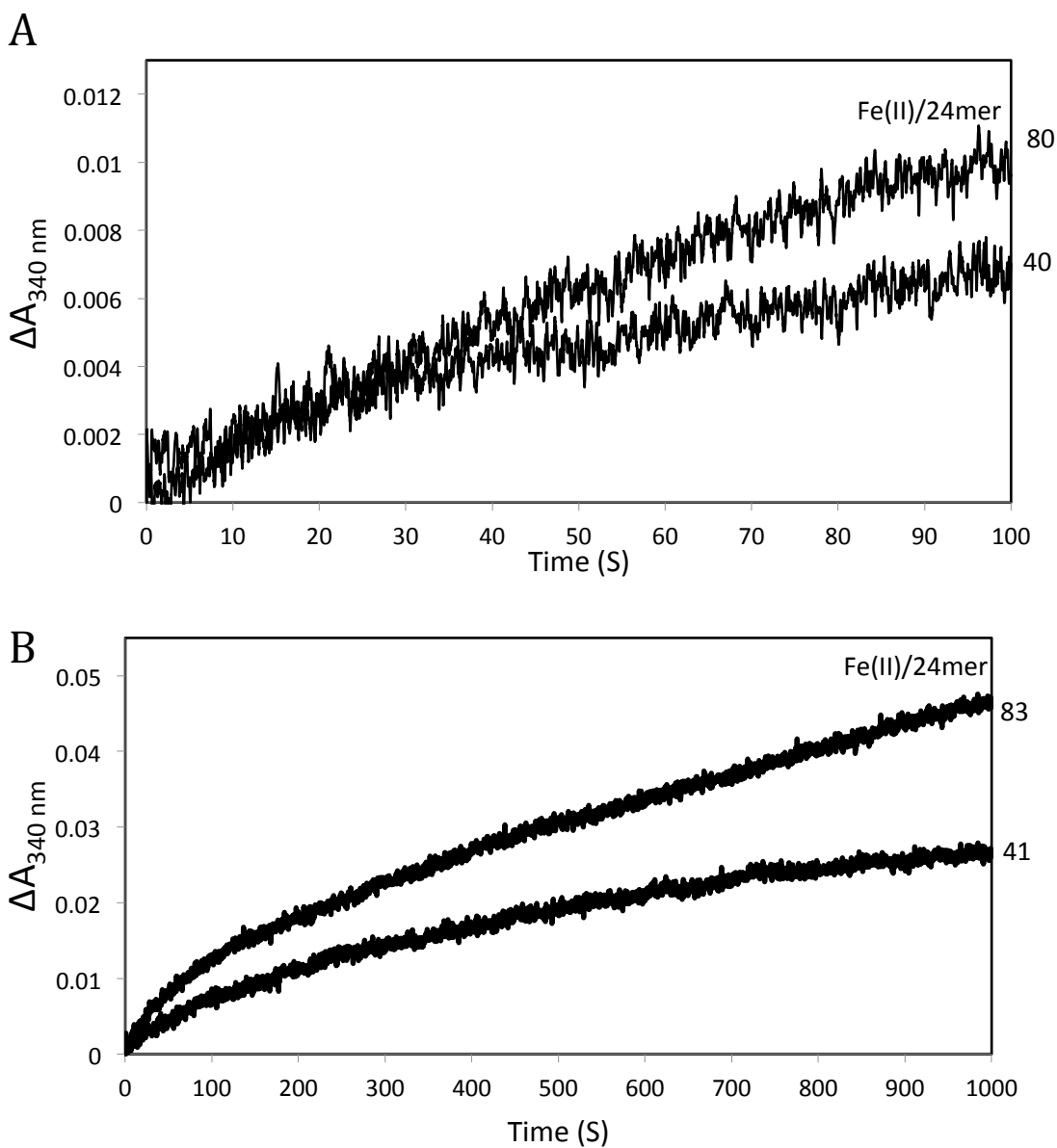


**Figure 4.3.** Kinetic analyses of Fe(II) oxidation catalysed by non-Cys PmFTN. (A) and (B) stopped-flow measurements of absorbance changes at 340 nm following the addition of 41 or 83 Fe(II) ions per protein to a sample of PmFTN previously treated with 50 Fe(II) per protein under aerobic conditions. The incubation time between Fe(II) additions was 30 min. 1.2  $\mu\text{M}$  PmFTN was in 0.1 M MES pH 6.5.

## **4.2 Variations of PmFTN at site C**

To discover more about the mechanism of mineralisation in the diatom ferritin, and particularly, the role of site C, a number of site-directed variants were generated (by the Murphy Lab, Department of Microbiology and Immunology, University of British Columbia, Canada) for kinetic studies. These were: E44Q (non-Cys), E44H and E130A (both alkylated). Glu44 coordinates iron at site C. Substitution of Glu with Gln is intended to test for the importance of the negative charge at site C, while substitution with His is intended to explore the flexibility of coordination at site C. Glu130 is observed to coordinate iron at both site B and site C, usually as a bridging ligand between the two simultaneously occupied sites, but it has also been observed bound only to site C. By substituting this residue with Ala, a non-coordinating residue, the intention was to test the importance of a ligand that connects site B and C.

## **4.3 E44Q variant of PmFTN**

Having established that the substitution of the three Cys residues of PmFTN does not significantly affect the iron-storage properties of the protein, a further mutation was introduced, resulting in the substitution of Glu44 with glutamine (E44Q). For the sake of brevity, that the substitution is in a Cys-free background won't be referred to again.

To test the capacity of the E44Q variant to store iron, sequential additions of 400 Fe(II) were made, see Figure 4.4A. This shows that significant precipitation occurs after 1600 Fe(II) ions were added, and after 2800 Fe(II) ions the protein was completely precipitated. Figure 4.4B shows a plot of the initial rate of Fe(II) oxidation as a function of Fe(II) ions added per E44Q PmFTN. It shows a maximum initial rate at around 1200 Fe(II) ions. At 2400 Fe(II) ions added, the rate of oxidation increased again, with the lowest initial rate of oxidation at 400 Fe(II) ions

and 2800 Fe(II) ions. However, above 1600 irons per protein, it is clear that very little additional iron is actually stored in the protein.

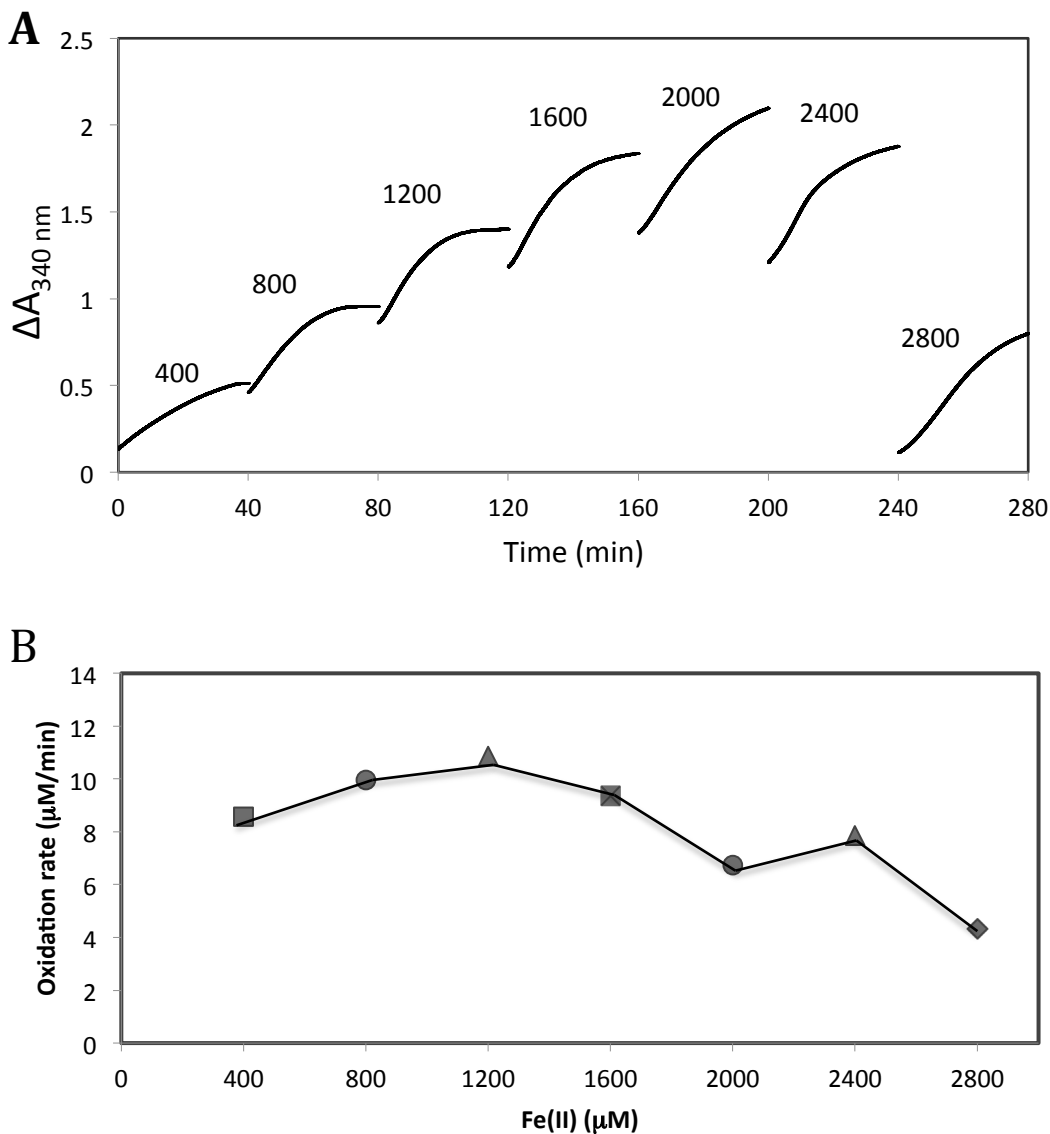


**Figure 4.4.** Iron mineralisation in E44Q PmFTN. (A) Absorbance changes at 340 nm showing Fe(II) oxidation in the presence of 0.5  $\mu\text{M}$  PmFTN in 0.1 MES pH 6.5. Numbers indicate total Fe(II) ion additions (sequentially added 400 Fe(II) ions per PmFTN) at 25  $^{\circ}\text{C}$  and pathlength 1 cm. (B) Plot of rate of Fe(II) oxidation, catalysed by 0.5  $\mu\text{M}$  PmFTN in 0.1 MES pH 6.5, as a function of Fe(II) ions added per PmFTN.

### 4.3.1 Fe(II) oxidation kinetics at the ferroxidase centre

Figure 4.5A shows the absorption changes at 340 nm following the mixing of 1.2  $\mu\text{M}$  apo-E44Q PmFTN variant, in 0.1 M MES buffer at pH 6.5, with various amounts of ferrous iron as function of time. Similar to wild-type proteins, it shows a very rapid oxidation phase, the oxidation being completed within 0.5 seconds. A plot of  $\Delta A_{340\text{ nm}}$  as a function of Fe(II), Figure 4.5B, reveals quite different behaviour to that of the wild-type protein, however. Absorption changes are small up to a level of  $\sim 30$  Fe(II) per protein, after which they significantly increase, levelling off when all 24 subunits have bound  $\sim 2$  equivalents of Fe(II), consistent with binding and oxidation of two Fe(II) ions per ferroxidase centre. This initial shallow slope is indicative of negative cooperatively with binding of one Fe(II) at each ferroxidase centre favoured over double occupancy. If two Fe(II) ions are required for oxidation to occur, this would account for why  $\Delta A_{340\text{ nm}}$  increases significantly above a level of  $\sim 1$  Fe(II) per subunit.

Figure 4.5C shows the fits of the E44Q variant data to either single or double exponential functions (as needed), providing an observed (pseudo-first order) rate constant,  $k$ . A plot of  $k$  as a function of Fe(II) concentration, Figure 4.5D, reveals a linear relationship, demonstrating a first order dependence of the rate of oxidation on the concentration of Fe(II), as observed for the wild-type protein, giving an apparent second order rate constant,  $k$ , of  $3.13(\pm 0.0027) \times 10^5 \text{ M}^{-1} \text{ s}^{-1}$ . This is slightly higher than the wild-type protein rate constant. In terms of rate, the ferroxidase centre reaction in the E44Q variant is not significantly affected.

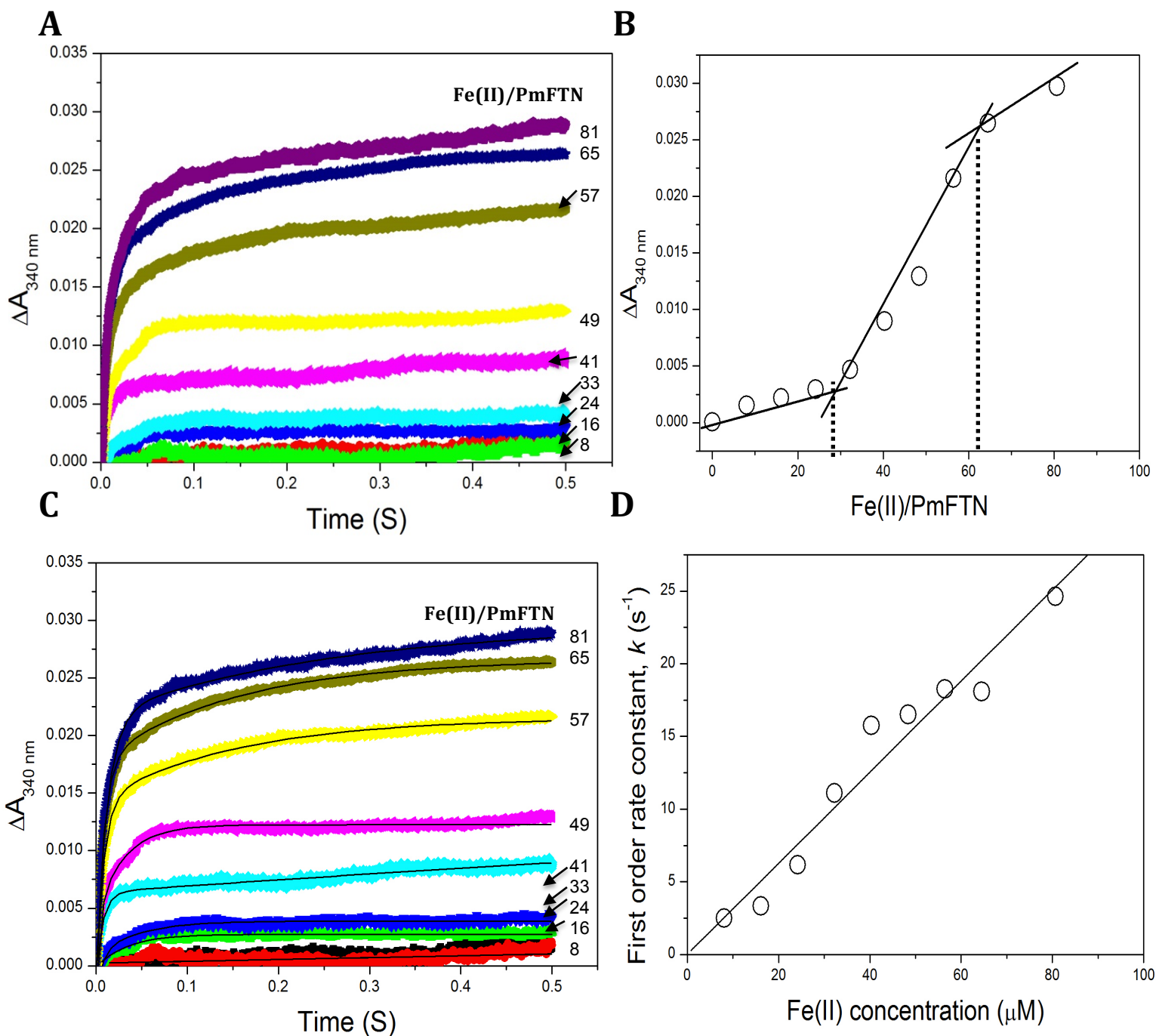


**Figure 4.5.** Kinetic analyses of Fe(II) oxidation catalysed by E44Q PmFTN (A) Fe(II) was added to final concentrations of 0, 10, 20, 30, 40, 50, 60, 70, 80 and 100  $\mu\text{M}$  to PmFTN (1.2  $\mu\text{M}$ ) in MES buffer (0.1 M, pH 6.5, 25  $^{\circ}\text{C}$ ) using a stopped-flow instrument. (B) Plot of observed (pseudo-first order) rate constants, obtained from fitting the data in A, as a function of Fe(II) concentration. A linear fit of the data is drawn in. (C). Final absorbance change after 0.5 seconds of iron oxidation at various ratios of Fe(II)/PmFTN subunit concentration. The three clear phases are highlighted, intersecting at  $\sim 30$  and  $\sim 60$  Fe(II) per protein, represented by the dotted line. (D). Fitting of PmFTN-catalysed Fe(II) oxidation data. Each of the A340 nm traces corresponding to additions of 8 – 81 Fe(II) ions per PmFTN were fitted to a single and double exponential function. The solid line fits are shown along with the data from part A.

### 4.3.2 Regeneration of rapid oxidation in PmFTN

Variant E44Q was also examined to determine whether the extremely rapid oxidation of Fe(II) observed upon addition of 48 Fe(II) per PmFTN can be regenerated. PmFTN was loaded with 48 Fe(II) per 24mer and then subsequently incubated for 30 minutes or 20 hours. Then, a further aliquot of Fe(II) (either 41 or 83 Fe(II) per protein) was added and changes in A<sub>340</sub> nm were measured. Figure 4.6A shows changes A<sub>340</sub> nm over 100 seconds after incubation for 30 minutes. Figure 4.6B shows A<sub>340</sub>nm over 1000 seconds with similar conditions. Clearly, rapid oxidation is not observed. The incubation over 20 hours showed similar behaviour to the 20 minutes incubation (not shown). The data are distinct from that of wild-type in that oxidation is complete within ~ 300 seconds for the addition of 40 Fe(II) per protein and ~600 seconds for 80 Fe(II) per protein.

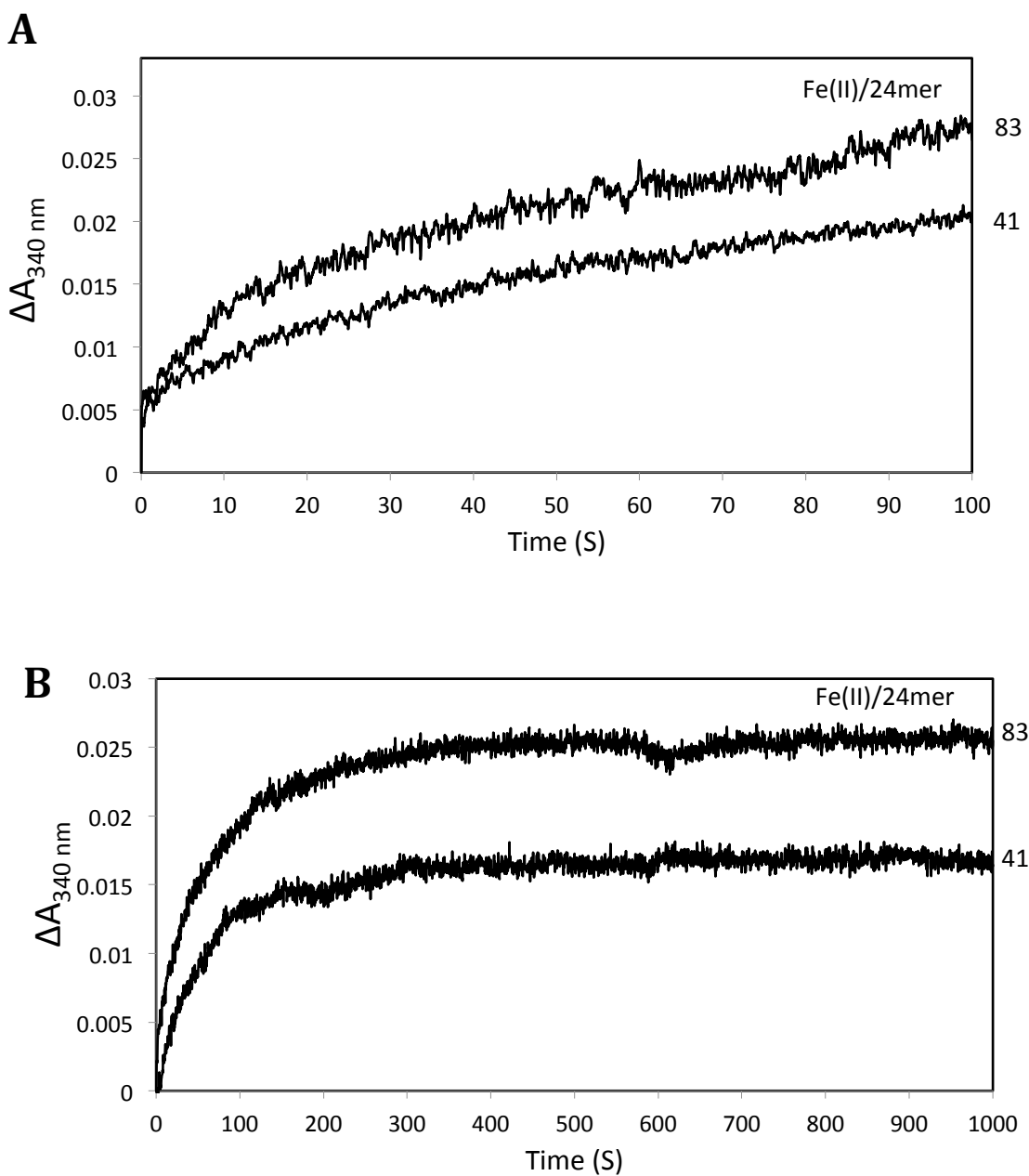


**Figure 4.6.** Kinetic analyses of Fe(II) oxidation catalysed by E44Q PmFTN. (A) and (B) stopped-flow measurements of absorbance changes at 340 nm following the addition of 41 or 83 Fe(II) ions per protein to a sample of PmFTN previously treated with 50 Fe(II) per protein under aerobic conditions. The incubation time between Fe(II) additions was 30 min. 1.2  $\mu\text{M}$  PmFTN was in 0.1 M MES pH 6.5.

#### 4.4 E44H variant of PmFTN

Another Glu44 variant, E44H, was also investigated. In this case, the substitution was introduced to the wild-type protein and the variant protein was alkylated prior to study.

##### 4.4.1 Fe(II) oxidation kinetics at the ferroxidase centre

Figure 4.7A shows the absorption changes at 340 nm following the mixing of 1.2  $\mu\text{M}$  apo-E44H PmFTN variant, in 0.1 M MES buffer at pH 6.5, with various amounts of ferrous iron as function of time. Similar to alkylated-wild type it showed a very rapid oxidation of ferrous ion, the oxidation being completed within 0.5 seconds. As with E44Q, a plot of  $\Delta A_{340\text{nm}}$  (Figure 4.7B) versus Fe(II) consists of an initial low amplitude phase up to  $\sim 24$  Fe(II) per protein (1 Fe(II) per subunit) followed by a much larger increase in  $\Delta A_{340\text{nm}}$  up to  $\sim 56$  Fe(II) per protein. As for E44Q, this indicates the presence of negative cooperativity.

Each Fe(II) oxidation trace was fitted to either a single or double exponential function, providing an observed (pseudo-first order) rate constant,  $k$ , Figure 4.7C. A plot of  $k_0$  as a function of Fe(II) concentration, Figure 4.7D, revealed, as for wild-type PmFTN, a linear relationship, demonstrating a first order dependence of the rate of oxidation on the concentration of Fe(II). The slope of the line provides an apparent second order rate constant,  $k$ , of  $1.02(\pm 0.74) \times 10^5 \text{ M}^{-1} \text{ s}^{-1}$ . This value is lower than that of the wild-type protein indicating that the lack of Glu at position 44 has some effect on the rate of ferroxidase reaction.

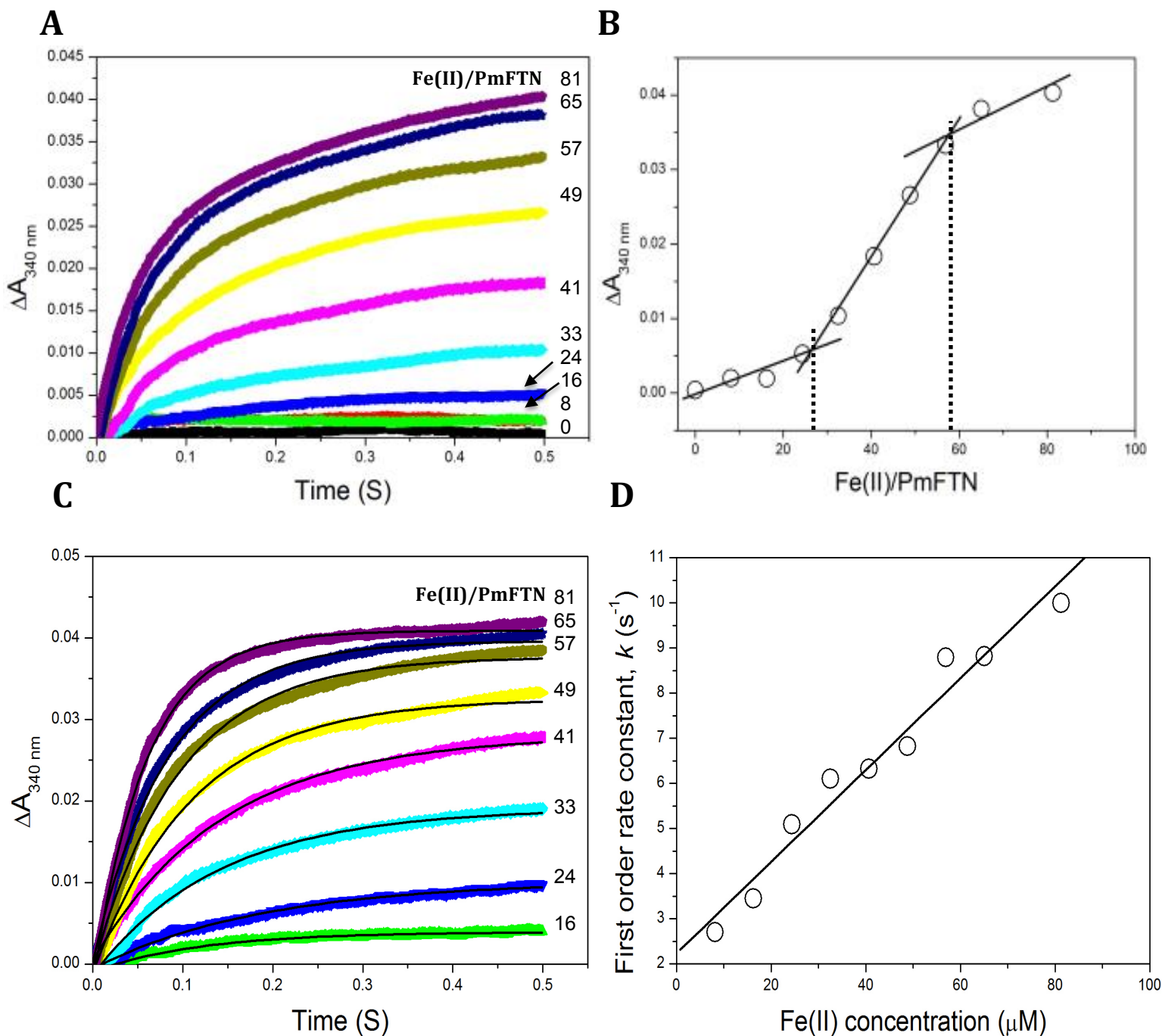


**Figure 4.7.** Kinetic analyses of Fe(II) oxidation catalysed by E44H PmFTN (A) Fe(II) was added to final concentrations of 0, 10, 20, 30, 40, 50, 60, 70, 80 and 100  $\mu\text{M}$  to PmFTN (1.2  $\mu\text{M}$ ) in MES buffer (0.1 M, pH 6.5, 25  $^{\circ}\text{C}$ ) using a stopped-flow instrument. (B) Plot of observed (pseudo-first order) rate constants, obtained from fitting the data in A, as a function of Fe(II) concentration. A linear fit of the data is drawn in. (C). Final absorbance change after 0.5 seconds of iron oxidation at various ratios of Fe(II)/PmFTN subunit concentration. The three clear phases are highlighted, intersecting at  $\sim 24$  and  $\sim 56$  Fe(II) per protein, represented by the dotted line. (D). Fitting of PmFTN-catalysed Fe(II) oxidation data. Each of the  $A_{340 \text{ nm}}$  traces corresponding to additions of 8 – 81 Fe(II) ions per PmFTN were fitted to a single and double exponential function. The solid line fits are shown along with the data from part A.

#### 4.4.2 Regeneration of rapid oxidation in PmFTN

E44H PmFTN was also examined to determine whether the extremely rapid oxidation of Fe(II) observed upon addition of 48 Fe(II) per PmFTN can be regenerated. PmFTN was loaded with 48 Fe(II) per 24mer and then subsequently incubated for 30 minutes or 20 hours. Then, a further aliquot of Fe(II) (either 41 or 83 Fe(II) per protein) was added and changes in A340 nm were measured. Figure 4.8A shows changes in A340 nm over 100 seconds after incubation for 30 minutes. As for the other proteins in this study, rapid oxidation is not seen. Furthermore, oxidation is not complete even over 1000 s as shown in Figure 4.8B. The incubation over 20 hours showed similar behaviour to the 20 minutes incubation. The data are very similar to that of wild-type PmFTN and therefore distinct from E44Q (in the Cys-free background).

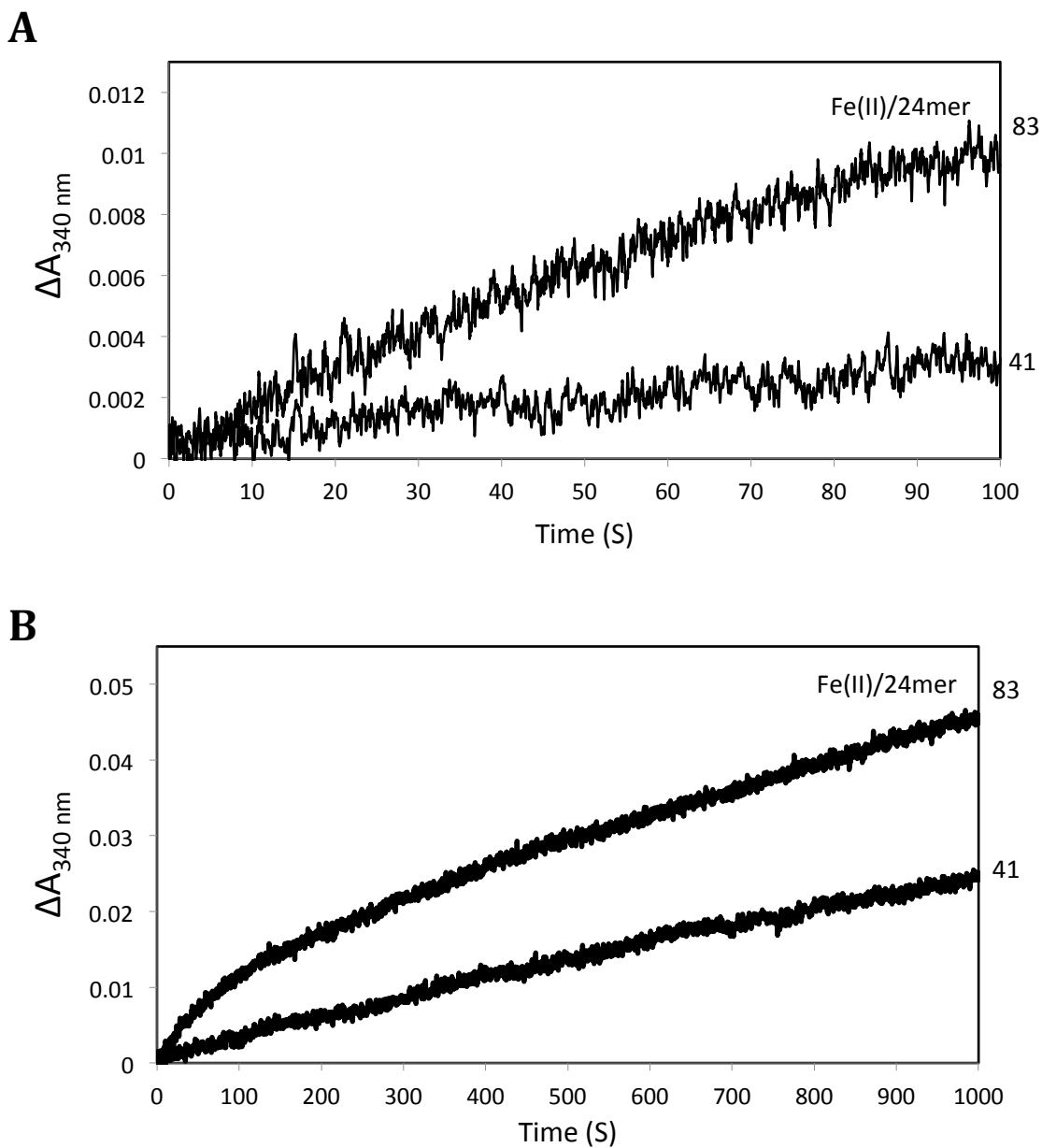


**Figure 4.8.** Kinetic analyses of Fe(II) oxidation catalysed by E44H PmFTN. (A) and (B) stopped-flow measurements of absorbance changes at 340 nm following the addition of 40 or 80 Fe(II) ions per protein to a sample of PmFTN previously treated with 50 Fe(II) per protein under aerobic conditions. The incubation time between Fe(II) additions was 30 min. 1.2  $\mu\text{M}$  PmFTN was in 0.1 M MES pH 6.5.

## 4.5 E130A variant of PmFTN

The final site directed variant that was studied was E130A which was generated in a wild-type background and alkylated.

### 4.5.1 Fe(II) oxidation kinetics at the ferroxidase centre

Figure 4.9A shows the absorption changes following the mixing of 1.2  $\mu\text{M}$  apo-E130A PmFTN, in 0.1 M MES buffer at pH 6.5, with various amounts of ferrous iron as function of time. Similar to wild-type protein it shows a very fast rapid oxidation of ferrous ion, the oxidation being completed within 0.5 seconds. As in the Glu44 variants, a plot of  $\Delta A_{340\text{ nm}}$  as a function of Fe(II)/protein consists of three phases: an initial shallow phase breaking at  $\sim 1$  Fe(II) per subunit, a steep second phase saturating at  $\sim 2$  Fe(II) per subunit, and a third shallow phase (Figure 4.9B). As for both Glu44 variants, E130A exhibits negative cooperativity in terms of Fe(II) binding.

Figure 4.9C shows that each trace for E130A fitted well to a single exponential function, providing an observed (pseudo-first order) rate constant,  $k$ . A plot of  $k$  as a function of Fe(II) concentration, gave a straight line, again demonstrating a first order dependence of the rate of oxidation on the concentration of Fe(II). The slope of the line in Figure 4.9D provides an apparent second order rate constant,  $k$ , of  $1.75(\pm 0.17) \times 10^5 \text{ M}^{-1} \text{ s}^{-1}$ , which is somewhat lower than that of the wild-type protein.

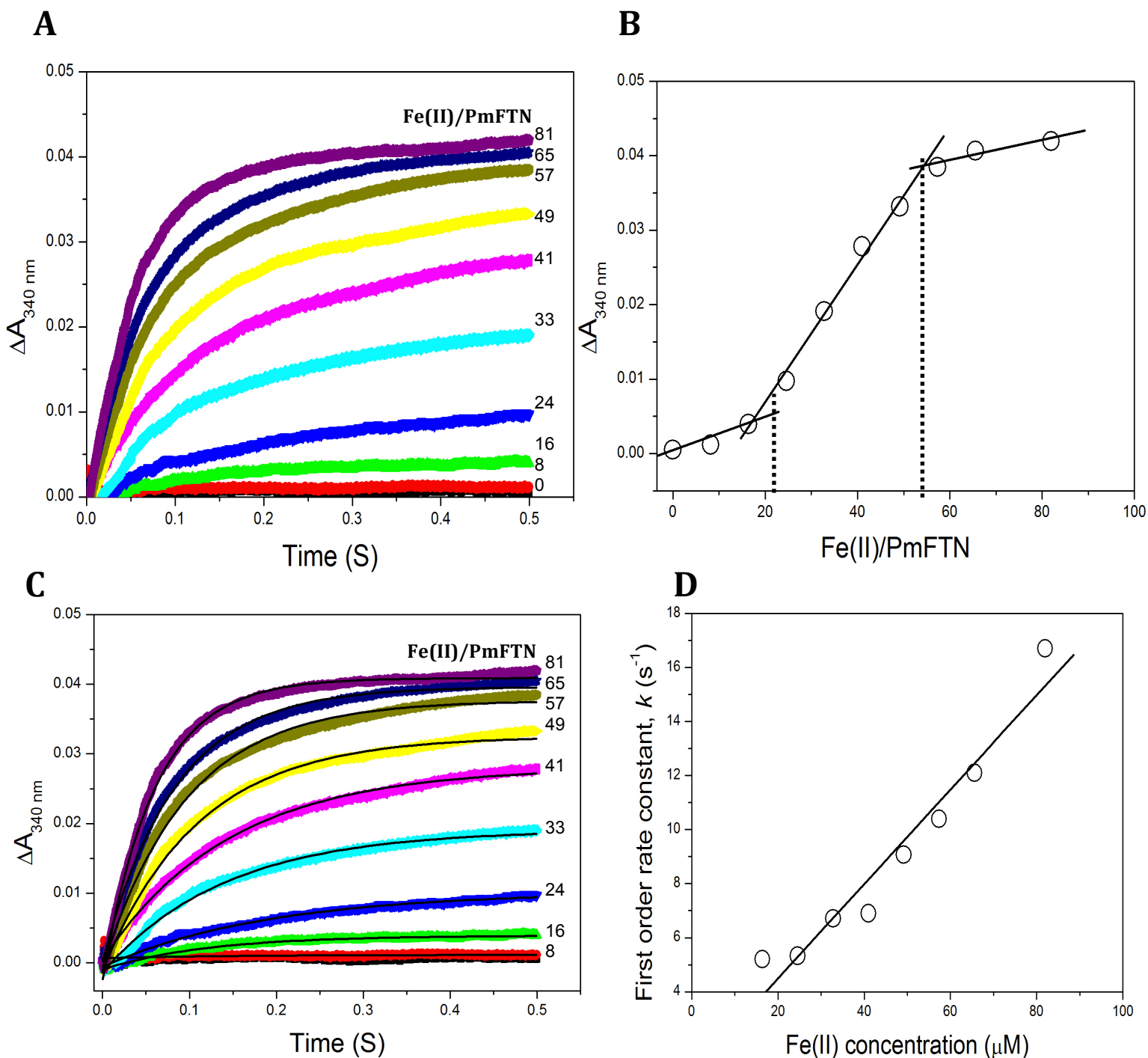


**Figure 4. 9.** Kinetic analyses of Fe(II) oxidation catalysed by E130A PmFTN (A) Fe(II) was added to final concentrations of 0, 10, 20, 30, 40, 50, 60, 70, 80 and 100  $\mu\text{M}$  to PmFTN protein (1.2  $\mu\text{M}$ ) in MES buffer (0.1 M, pH 6.5, 25  $^{\circ}\text{C}$ ) using a stopped-flow instrument. (B) Plot of observed (pseudo-first order) rate constants, obtained from fitting the data in A, as a function of Fe(II) concentration. A linear fit of the data is drawn in. (C). Final absorbance change after 0.5 seconds of iron oxidation at various ratios of Fe(II)/PmFTN subunit concentration. The three clear phases are highlighted, intersecting at  $\sim 24$  and  $\sim 52$  Fe(II) per protein, represented by the dotted line. (D). Fitting of PmFTN-catalysed Fe(II) oxidation data. Each of the  $A_{340 \text{ nm}}$  traces corresponding to additions of 8 – 81 Fe(II) ions per PmFTN were fitted to a single exponential function. The solid line fits are shown along with the data from part A.

#### **4.5.2 Regeneration of rapid oxidation in PmFTN**

The ability of E130A PmFTN to regenerate its rapid oxidation phase was investigated. E130A PmFTN was loaded with 48 Fe(II) per 24mer and then subsequently incubated for 30 minutes or 20 hours. Then, a further aliquot of Fe(II) (either 41 or 83 Fe(II) per protein) was added and changes in A340 nm were measured. Figure 4.10A shows changes in A340 nm over 100 seconds after incubation for 30 minutes, and Figure 4.10B shows over 1000 seconds. As for all other PmFTN in proteins studied here, rapid oxidation is not seen. However, oxidation was complete for addition of 40 and 80 Fe(II) per protein within 200 seconds, much more rapidly than in a wild-type PmFTN or the Glu44 variants. The incubation over 20 hours showed similar behaviour to the 20 minutes incubation (not shown).

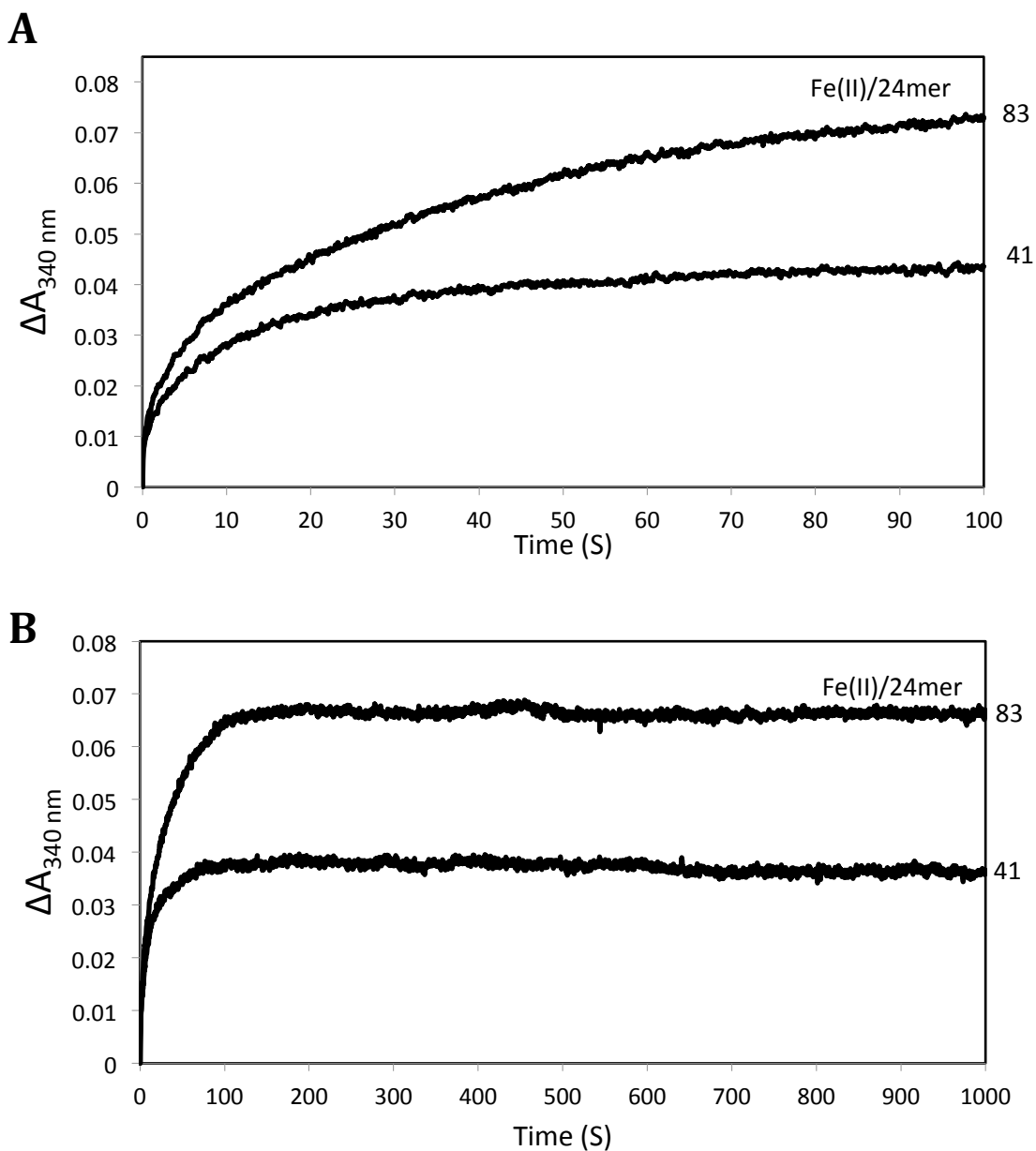


**Figure 4.10.** Kinetic analyses of Fe(II) oxidation catalysed by E130H PmFTN. (A) and (B) stopped-flow measurements of absorbance changes at 340 nm following the addition of 41 or 83 Fe(II) ions per protein to a sample of PmFTN previously treated with 50 Fe(II) per protein under aerobic conditions. The incubation time between Fe(II) additions was 30 min. 1.2  $\mu\text{M}$  PmFTN was in 0.1 M MES pH 6.5.

#### 4.6 Iron core formation kinetics in PmFTN

Given the difference observed in the kinetics of Fe(II) oxidation in regeneration experiments, the ability of the E130A to store iron was investigated further and compared directly with the other variants. Iron core formation kinetics following addition of 400 of Fe(II) ions per apo-PmFTN (wild-type and variant proteins) were followed by monitoring absorbance changes at 340 nm for 1000 seconds, as shown in Figure 4.11. Mineralisation involves the binding and oxidation of Fe(II) but the mechanism for this process in PmFTN is not known. The data for E44Q is similar to that for wild-type PmFTN, while mineralisation in E44H PmFTN is significantly slower. Remarkably, mineralisation in the variant E130A occurs much more rapidly and is complete within 400 seconds (compared to 1800 seconds for the wild-type protein).

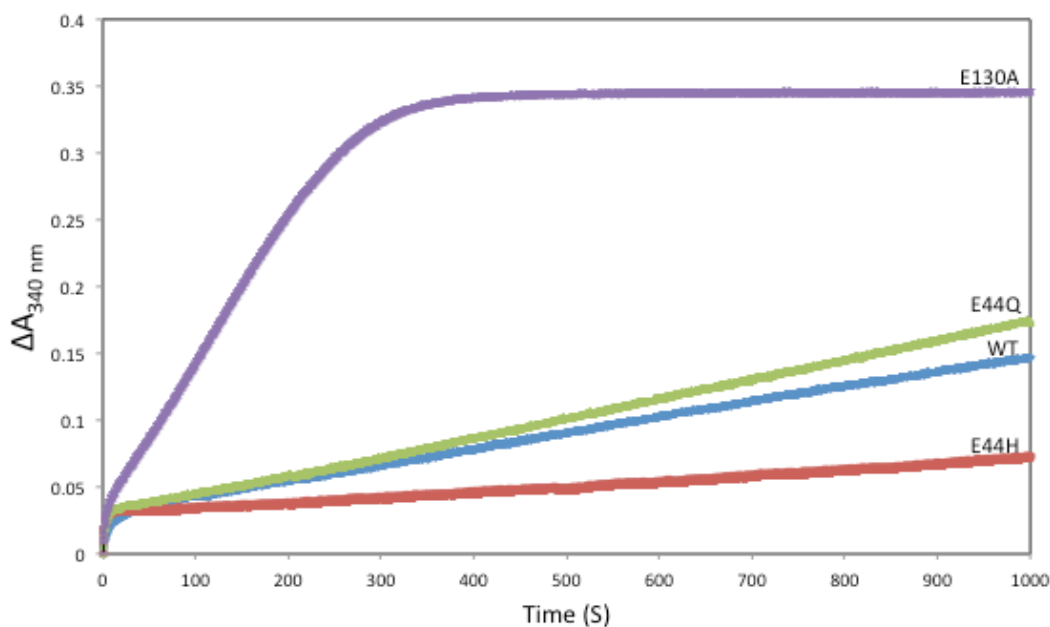


**Figure 4.11.** Absorbance changes at 340 nm showing Fe(II) oxidation in the presence of 0.5  $\mu\text{M}$  wild-type and various PmFTN in 0.1 MES pH 6.5. 400 Fe(II) ions per PmFTN were added at 25  $^{\circ}\text{C}$  and pathlength 1 cm.

## 4.7 Discussion

Third iron site is generally not associated with ferritin ferroxidase sites. The site C has been observed in some non-heme ferritins from bacteria and archaea: *E. coli* (EcFtnA) (33, 55), *Pyrococcus furiosus* (PfFtn) (34), and *Archaeoglobus fulgidus* (AfFtn) (68). However, these sites vary from that of PmFTN in terms of the number and origin of coordinating glutamate residue. One of these residues is Glu130, which is seen to bridge the iron atom of site B and C (Figure 4.12) and is conserved in prokaryotic ferritins. In EcFtnA Glu130 is proposed to adjust its position so it can bind iron ions in sites B and C as well as gating the passage of the iron through these sites (69). Similarly, in PmFTN Glu44 and Glu130 may provide similar function of gating the passage of iron from site B to site C.

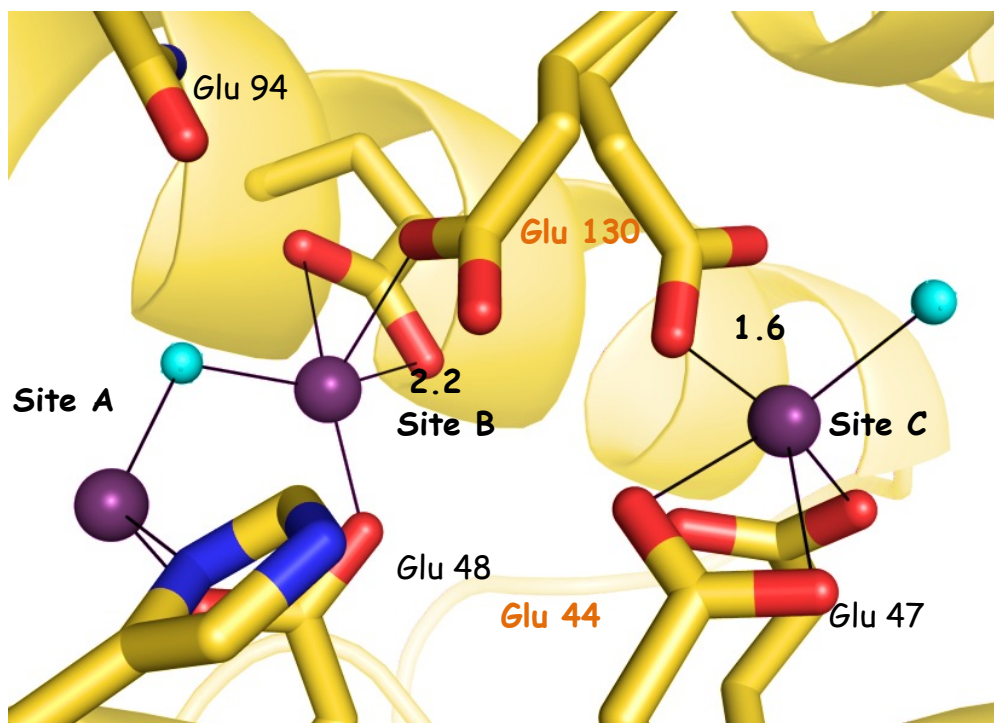


**Figure 4.12.** The substituted residues Glu44 and Glu130, shown in red, exhibits coordination at site C. Iron Glu130 is also observed coordinating to site B. Water molecule show in blue sphere.

PmFTN contains three Cys residues, which presented a challenge during crystallization; therefore, they were alkylated or removed in order to improve the stability of the protein. Here, the alternative strategy of substitution with alanines was attempted. Our results suggest that substitution of three Cys residues of PmFTN (Figure 4.2) resulted in a protein with properties similar to those of the alkylated (and non-alkylated) wild-type protein, as seen in Chapter 3. This suggests the three Cys residues do not play an important role in Fe(II) oxidation and iron uptake. The data suggest that variants E44Q (in Cys-free background), E44H (alkylated) and H130A (alkylated) all exhibited rapid phase 2 oxidation of Fe(II) at the ferroxidase centre with a rate only slightly lower than that of the wild-type protein. However, the shape of the  $\Delta A_{340\text{ nm}}$  versus Fe(II) plot was different, in each case, to that of the wild-type protein. Rather than a linear increase toward a point of saturation corresponding to 2 Fe(II) ions per subunit, distinct phases below and above a level of 1 Fe(II) per subunit were observed. At low Fe(II) levels (up to 1 Fe(II) per subunit) very low intensity increases in  $\Delta A_{340\text{ nm}}$  were observed, indicating that very little Fe(II) oxidation had occurred. Above a level of 1 Fe(II) per subunit, much larger absorbance changes were detected, indicating that the majority of Fe(II) oxidation occurred here. This is interpreted in terms of negative cooperativity of Fe(II) binding to the ferroxidase centre variants. Thus, in these variants, Fe(II) binds to the apo-ferroxidase centre in preference to a centre that already contains an Fe(II) ion. Because Fe(II) oxidation only occurs when the centre contains two Fe(II) ions, significant oxidation only occurs when more than 24 Fe(II) ions are added to the protein. It is likely that the affinity of Fe(II) for site B is affected in the variants, since the substitution are close to site B. In the case of E130A, the residue actually coordinates Fe(II) at site B. However, it is noticeable that the two Glu44 variants exhibit cooperativity to a greater extent. As for the wild-type protein, none of the variants exhibited a regeneration of the rapid ferroxidase reaction. E44Q and E130A exhibited some differences from wild-type protein in that oxidation of a

second aliquot of Fe(II) was complete much sooner than for the wild-type protein. This was much more apparent in E130A than in E44Q.

Addition of 400 Fe(II) per E130A PmFTN revealed a very significantly enhanced rate of mineralisation compared to wild-type and E44Q and E44H proteins (Figure 4.11). This is an unusual observation in that mutations do not normally significantly enhance activity. Mutation of site C in EcFtnA leads to a small reduction in the oxidation rate, and also an increase of iron movement to the iron core. These observations with EcFtnA led to the suggestion that the presence of site C offers advantages, for example, an increase of iron oxidation stoichiometry from 2 Fe(II)/O<sub>2</sub> in HuHF to 3–4 in EcFtnA perhaps avoids the production of reactive oxygen species. Also iron is retained longer at the ferroxidase centre/site C in the protein shell and is perhaps more easily accessible to iron-requiring anabolic processes in the cell (55). Similarly, in E130A iron mobility may be affected.

## Chapter 5: Mechanistic study of iron release from Bacterioferritin

### 5.1 Purifications in BFR

The BFR protein, expressed in *E. coli* pALN1 cells, was purified as described in chapter 2.

SDS-PAGE analysis was used to monitor purity during the preparation, see the gels shown in Figure 5.1A and 5.1B. The band corresponds to an approximate Mw of 18.6 kDa, in agreement with the Mw calculated from the amino acid sequence of a BFR subunit (18,553 Da). Note that anion exchange was employed to remove DNA contamination of the protein.

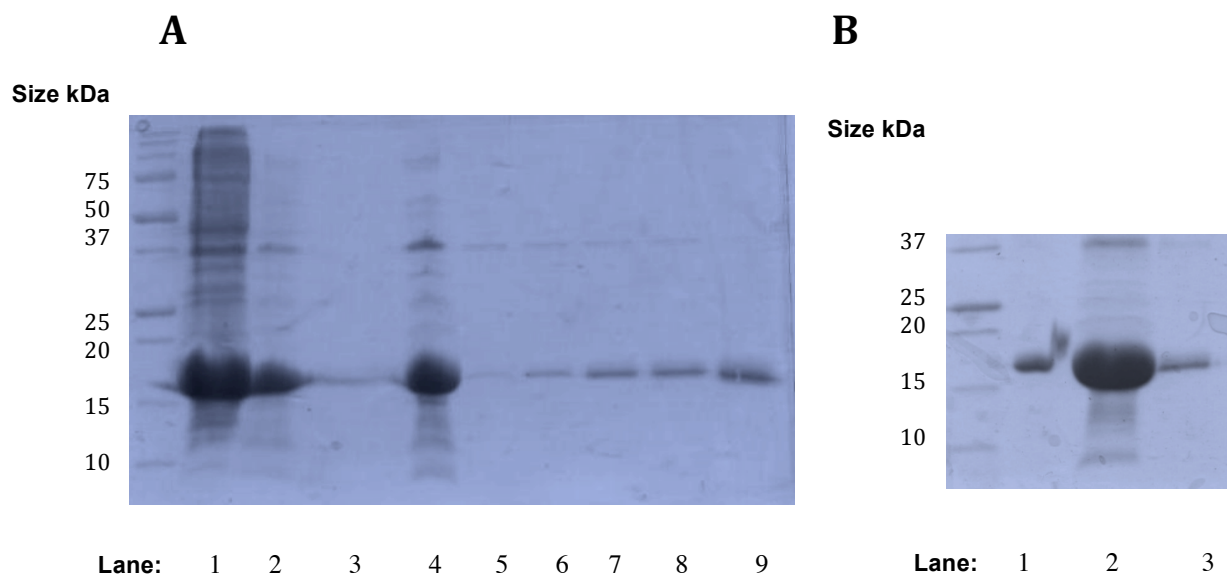


**Figure 5.1.** SDS-PAGE analysis of wild-type BFR purification. Lane 1, post sonication step (after centrifugation); lane 2, after heat shock step (after centrifugation); lane 3, ammonium sulphate step (55 percent cut, before centrifugation); lane 4, dialysis step (before centrifugation); lane 5, after gel filtration column (outer pool); lane 6, after gel filtration column (outer pool); lane 7 and 8, after gel filtration column (inner pool); lane 9, after gel filtration column (inner pool). (B) SDS-PAGE analysis of BFR following anionic exchange chromatography. Lane 1, 2 and 3, Wt BFR (inner pool).

## **5.2 Heme loading of *E. coli* BFR via a heat-treatment method**

### **5.2.1 The addition of exogenous heme to wild-type BFR**

In order to examine the role of heme in iron release from BFR it is necessary to have access to as wide a range of heme loadings as possible. However, the heme-binding site of BFR is not accessible from the outside of the protein and so, previously, heme incorporation needed to occur during protein assembly. Addition of exogenous heme to BFR in a high salt buffer (1 M NaCl 0.1 MES pH 6.5) at 25 °C result in changes in the UV-visible absorbance spectrum that are not consistent with specific binding of heme at its native site (Figure 5.2). In comparison, addition of heme to an identical sample of BFR followed by heating to 80 °C for 15 minutes resulted in very different changes in the UV-visible absorbance spectrum, without any significant precipitation of the protein. Following the addition of heme, the sample was cooled to room temperature and free and non-specifically bound heme was removed by passage of the sample through a PD-10 desalting column. This resulted in BFR containing an increased level of heme (Figure 5.3). The spectroscopic characteristics of the bound heme, in particular the Soret maximum at 418 nm and the absorbance at ~739 nm, which is indicative of bis-methionine ligation of heme, are identical to those of the naturally heme loaded protein (38).

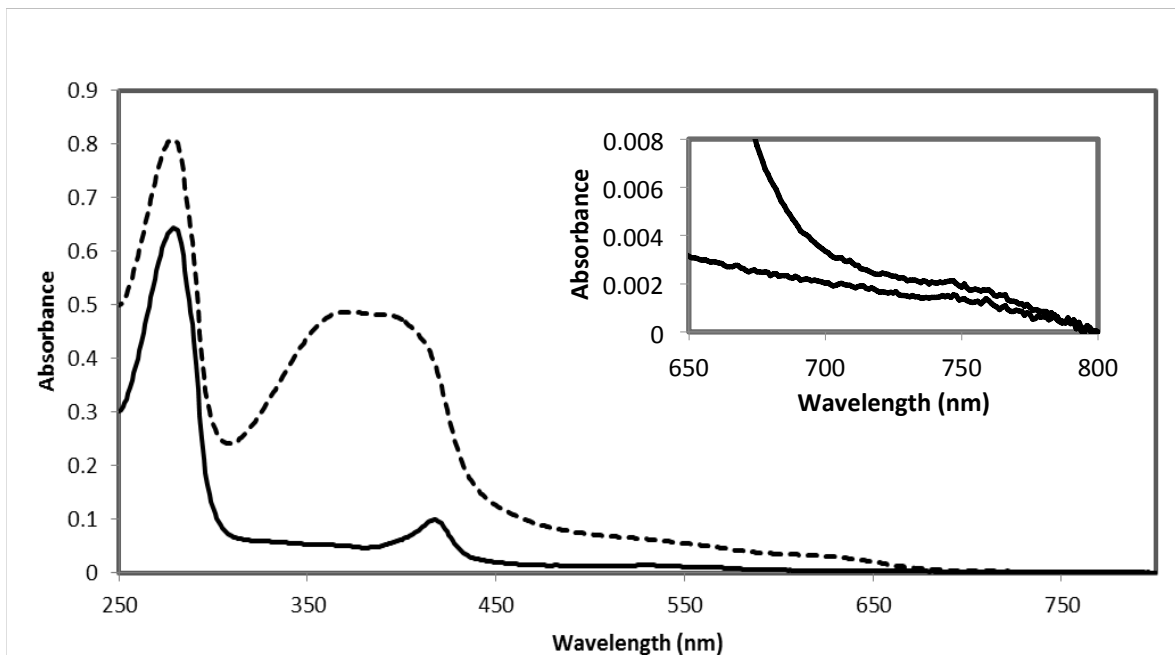


**Figure 5.2.** Addition of exogenous heme to BFR at 25 °C. UV-visible spectra 0.5  $\mu\text{M}$  BFR in 0.1 M MES pH 6.5 and 1 M NaCl before heme addition (solid line) and after addition of heme (dashed line). Pathlength 1 cm.

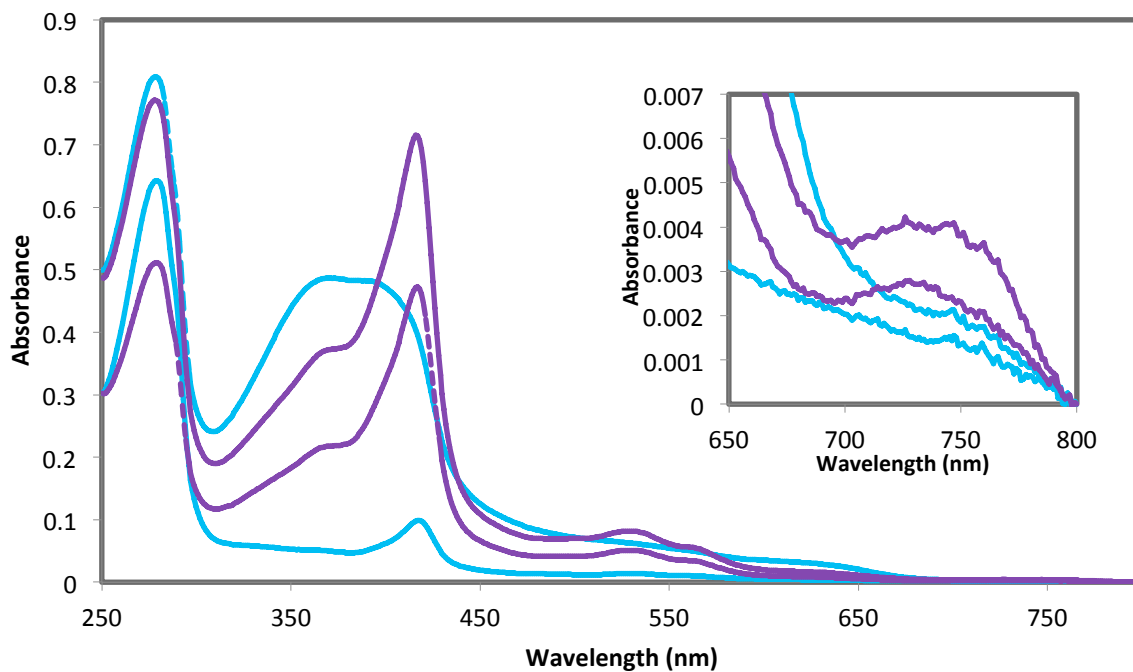


**Figure 5.3.** Addition of exogenous heme to BFR in a high salt buffer at 80 °C. spectra of 0.5  $\mu\text{M}$  BFR in 0.1 M MES pH 6.5 and 1 M NaCl before heme addition (—), after addition of heme (---), after addition of heme and heating to 80 °C (-.-), and (- -) passing through a desalting column. Inset is an expanded plot of absorbance showing the region of the spectrum in which a charge transfer band characteristic of bis-Methionine axial coordination occurs. Pathlength 1 cm.

Furthermore, addition of variable amounts of heme followed by the heat treatment yielded protein samples with various amounts of heme. Figure 5.4 shows BFR with 5, 6, 7, and 11 hemes. Note that overexpressed recombinant BFR usually contains very low levels of heme (approximately one hemes per 24mer). Thus, through this method, nearly fully heme loaded BFR was obtained.

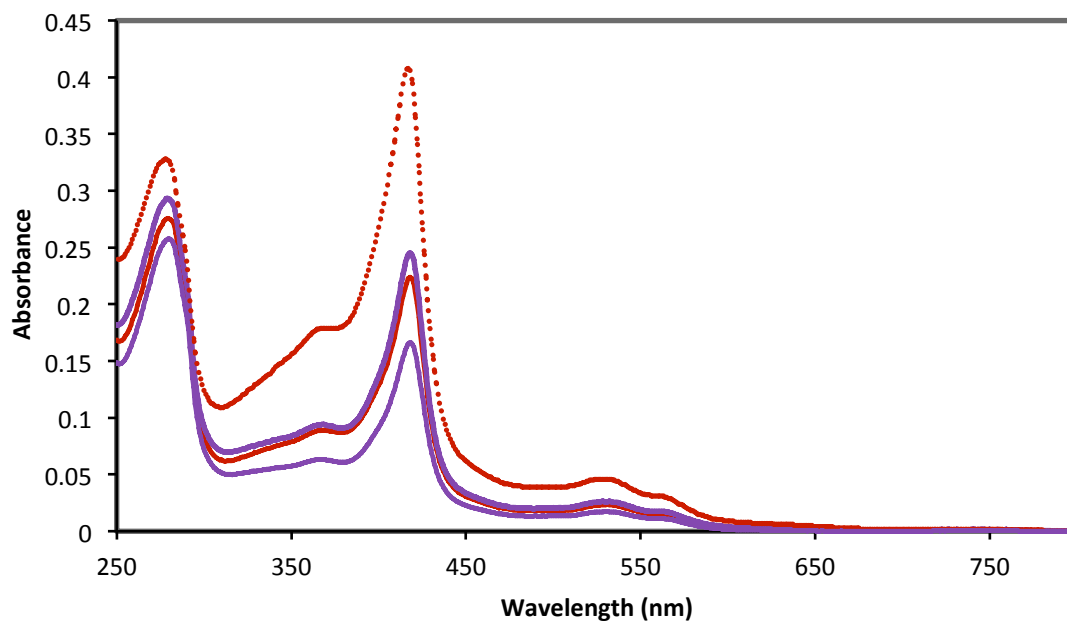


**Figure 5.4.** UV-visible spectra of heme-binding to BFR. Spectra of 0.5  $\mu$ M BFR in 0.1 M MES pH 6.5 and 1 M NaCl with varying levels of heme content after heme addition, heating to 80  $^{\circ}$ C and passage through a desalting column. BFR containing 5 (—), 6 (—), 7 (---), and 11 (---) hemes per protein. Pathlength 1 cm.

### 5.2.2 The addition of exogenous heme to heme-free (M52H) variant of BFR

To provide further evidence that the heme bound by wild-type BFR following heat treatment is bound at the native Met52/Met52 coordinated site, a site directed variant of BFR, M52H was employed. Previous studies of M52H BFR showed that the protein is isolated in a heme-free state, regardless of the fact that histidine is a typical coaxial heme ligand, found in many other

hemoproteins. This points to lack of flexibility at the heme site such that His is not positioned sufficiently well to coordinate heme above and below the plane, and the importance of Met52 in mediating the tight fit of the heme at its binding site in BFR (39).

Addition of heme with similar treatment as wild-type BFR, as described above, prompted approximately 25-35% of the variant protein to precipitate when heated at 80 °C. Heating M52H in the absence of heme did not unfavorably affect the protein stability. Addition of heme without heating also did not lead to precipitation. Hence, the combination of heating at 80 °C and the presence of heme caused instability and loss of the protein from solution. To overcome this problem, M52H BFR containing 12 equivalents of heme per BFR (24mer) was heated to 65 °C. This resulted in <10% precipitation of the variant protein. The removal of free and adventitiously bound heme was achieved by passage of the sample through a PD-10 desalting column. This resulted in the absorbance spectrum shown in Figure 5.5. The spectrum shows that a small amount of heme is bound to the protein. On closer inspection, see inset of Figure 5.5, the heme Soret band is not located at 418 nm, but rather at 405 nm. This is similar to the spectrum of met myoglobin and heme oxygenase (70, 71). This suggests that the ferric heme iron is bound by a single histidine residue. If it is assumed that this heme has the same heme molar absorptivity as that reported for heme oxygenase for its Soret absorbance at 405 nm ( $1.4 \times 10^5 \text{ M}^{-1} \text{ cm}^{-1}$ ) (72), about 0.3-0.4 mol of heme is bound to the M52H (24mer). Thus, the M52H variant is incapable of binding significant amounts of heme through the described post-purification method.

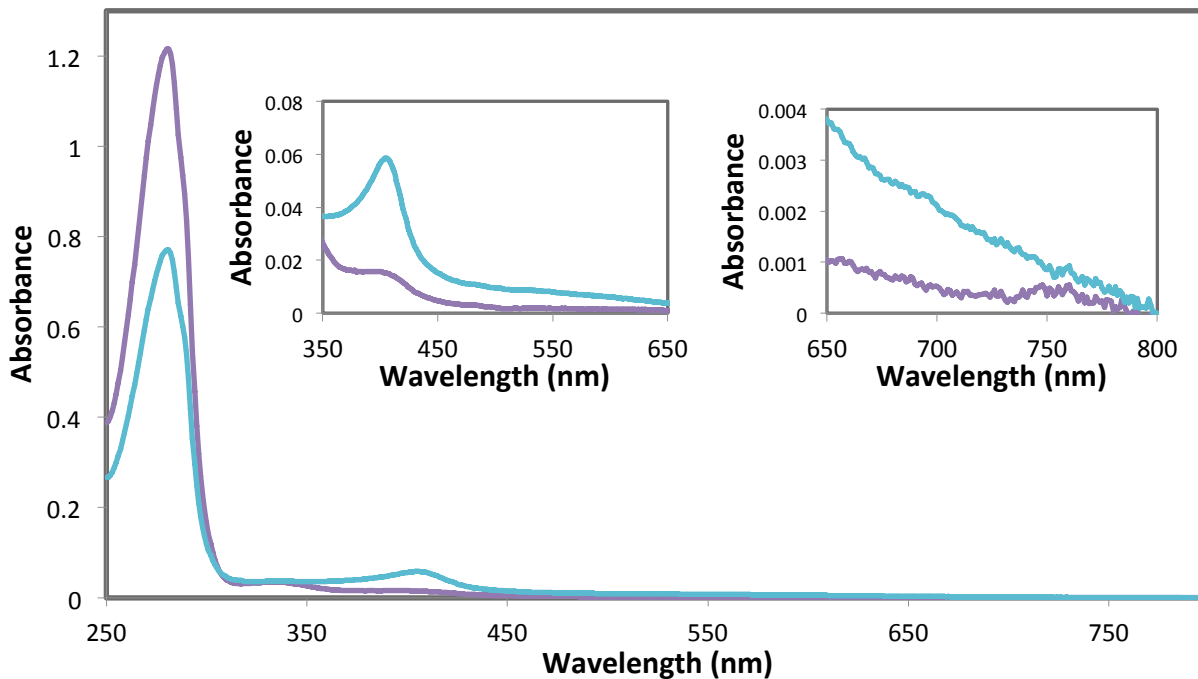


**Figure 5.5.** UV-visible absorbance spectra of M52H before and after addition of heme. 0.5  $\mu$ M M52H in 0.1 M MES pH 6.5 and 1 M NaCl before (–) and after (–) heme addition. Note that elution from a PD-10 desalting column results in a 1.5 x dilution of the protein. Insets are expanded plots of the 350-450 and 650-800 nm regions. Pathlength 1 cm.

To further confirm that the inability of M52H BFR to bind significant amounts of heme was not a result of the lower temperature employed during the procedure, wild-type BFR was treated with 12 mol equivalents of heme at 65 °C and eluted through a PD-10 column. In comparison to treatment at 80 °C, this method was not as efficient in promoting heme-binding, see Figure 5.6. The absorbance spectrum was identical with that following treatment at 80 °C, with the Soret band at 418 and absorbance at ~739 nm, which is indicative of bis-methionine ligation of heme. However, binding was limited to about 8 hemes per BFR (24mer). Furthermore, a low intensity band at approximately 650 nm was observed that was not apparent previously. This indicates the presence of some high-spin ferric-heme possibly due to heterogeneity of heme-binding at the

native binding site, with coordination of one Met52 instead of two. Overall, the data indicate that wild-type BFR, even at lower temperature, binds heme at the natural bis-methionine coordination site (51).

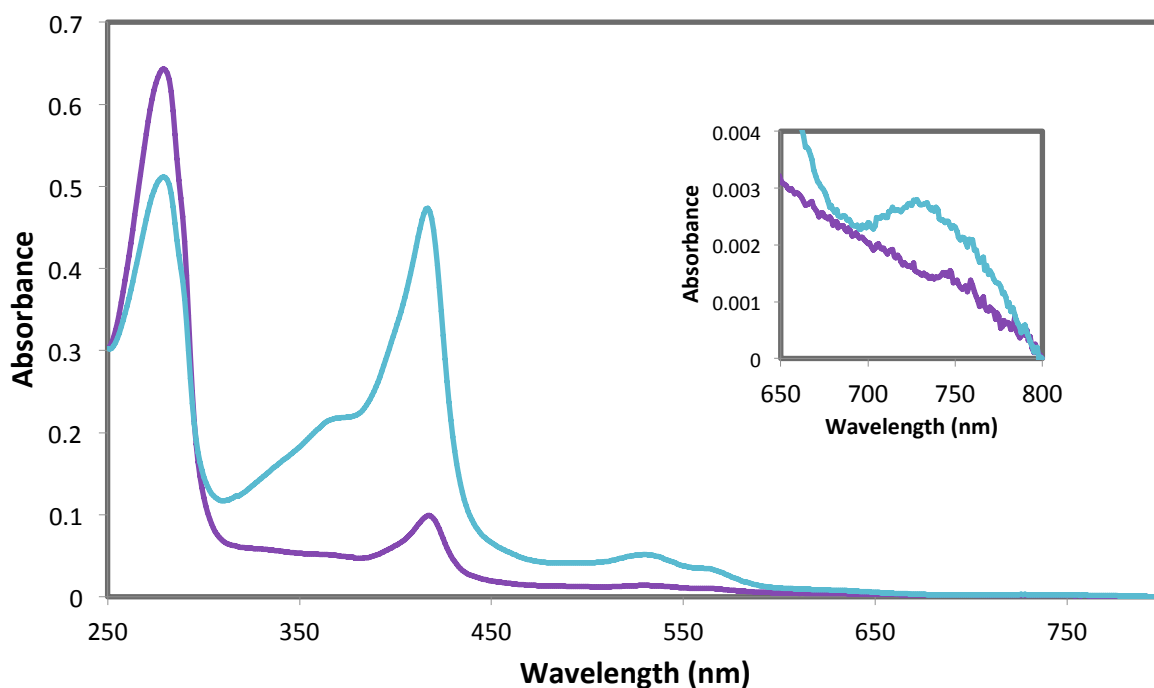


**Figure 5.6.** UV-visible absorbance spectra of wild-type BFR before (–) and after (–) heme addition at 65 °C. BFR (0.5  $\mu$ M) was in 0.1 M MES pH 6.5 and 1 M NaCl before heme addition. The sample was diluted during desalting to remove unbound or weakly bound heme. Inset is an expanded plot of absorbance at  $\sim$ 739 nm which is indicative of bis-methionine ligation of heme. Pathlength 1 cm.

In order to further characterize the low amount of heme bound to M52H, a more concentrated sample was needed. However, an effort to concentrate samples of M52H BFR resulted in loss of heme. This suggests that the heme is not stably coordinated to this variant of BFR, which is consistent with previous studies of expression in *E. coli*, which led to a protein without heme bound. Also, an attempt was made to reduce heme-M52H BFR using excess sodium dithionite. Wild-type BFR loaded with 9 hemes per protein was also treated with excess dithionite. The

absorption peaks at 418, 525, and 560 nm associated with the Soret,  $\beta$ , and  $\alpha$  band of the oxidised heme moiety, observed in 9 heme loaded BFR, were absent from the spectrum of M52H BFR (Figure 5.7 and Figure 5.8). Instead, a reduction in heme intensity was observed, with a minor increase in intensity in the 700 nm region.

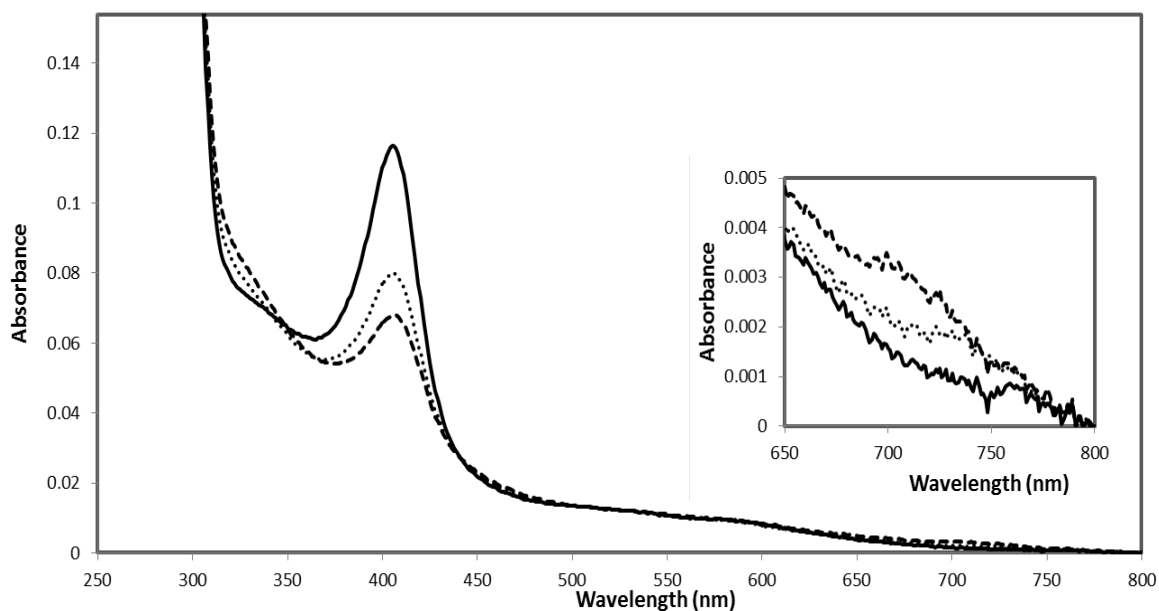


**Figure 5.7.** U.V- visible spectra of *E. coli* M52H BFR as isolated (solid line) and following treatment with excess sodium dithionite (dotted line). 2.8  $\mu$ M M52H BFR in 0.1 M MES pH 6.5 and 1 M NaCl. Inset is an expanded plot of the 650-800 nm region. Pathlength 1 cm.

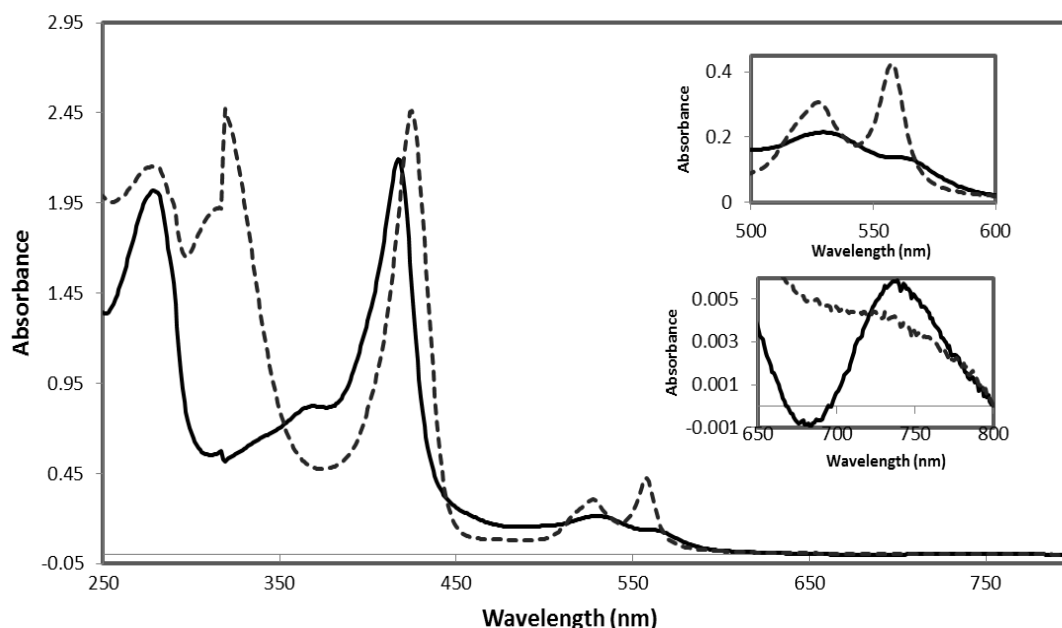


**Figure 5.8.** U.V-visible spectra of heme-loaded *E. coli* wild-type BFR (solid line) and following treatment with excess sodium dithionite (dotted line). 2.5  $\mu\text{M}$  BFR in 0.1 M MES pH 6.5 and 1 M NaCl. Insets are expanded plots of the 500-600 and 650-800 nm regions. Pathlength 1 cm.

### 5.3 The effect of heme on mineralisation and iron release from *E. coli* BFR

#### 5.3.1 Effect of heme on *E. coli* BFR iron core formation

The effect of heme bound to BFR on Phase 3 of mineralisation was studied by monitoring absorption changes at 340 nm after three sequential additions of 200  $\mu\text{M}$  Fe(II) to 0.5  $\mu\text{M}$  wild-type BFR in 0.1 M MES buffer at pH 6.5, and at 25 °C. Similar procedures were performed (0.5  $\mu\text{M}$  protein in 0.1 M MES buffer at pH 6.5, and at 25 °C) using heme loaded BFR (added via the method described above) and heme-free M52H BFR. The absorption changes with the first addition of iron resulted in an initial increase in absorbance. This instant jump (referred to as phase 2) is due to two Fe(II) ions becoming oxidised to Fe(III) ions at the dinuclear ferroxidase

centre located within each subunit. After the completion of Phase 2, if sufficient Fe(II) is present, iron is slowly oxidised (phase 3) leading to iron core formation. This is observed only under conditions where more Fe(II) is added than is required for full occupancy of the dinuclear sites. Figure 5.9 shows absorbance changes at 340 nm following sequential additions of 400 Fe(II) per protein. There is a clear difference in behaviour between the as isolated protein, which contains ~ 1 heme per 24mer, and the artificially heme loaded protein (containing 11 hemes per 24mer). For the first addition of iron, BFR with 11 hemes exhibited a lower rate of nucleation and initial iron core formation and essentially a sigmoidal shape. For the second and third additions of iron, the BFR with 11 hemes displayed significantly higher mineralisation rates, see Figure 5.10.

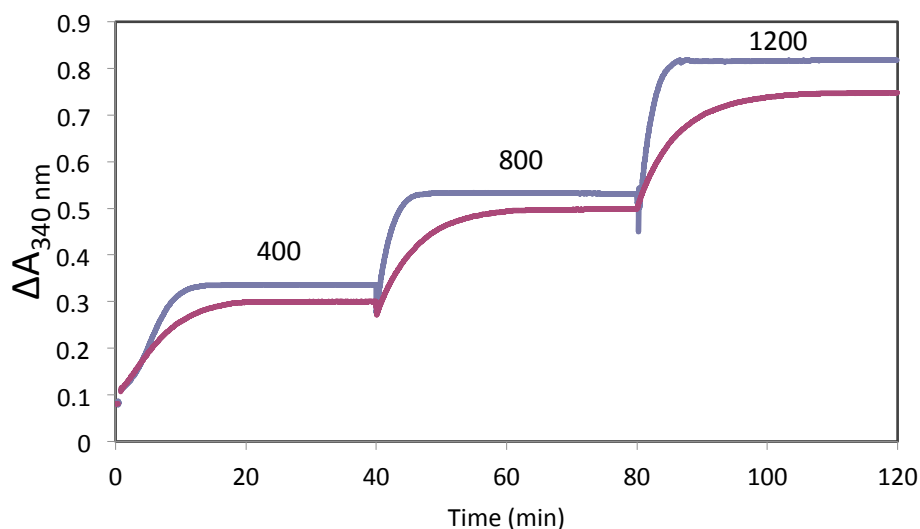


**Figure 5.9.** Iron uptake into *E. coli* BFR. 200  $\mu\text{M}$   $\text{Fe}^{2+}$  was added to 0.5  $\mu\text{M}$  BFR as isolated BFR (—), and BFR with 11 hemes (—) in MES buffer 0.1M, pH 6.5, 25 °C. Pathlength 1 cm.

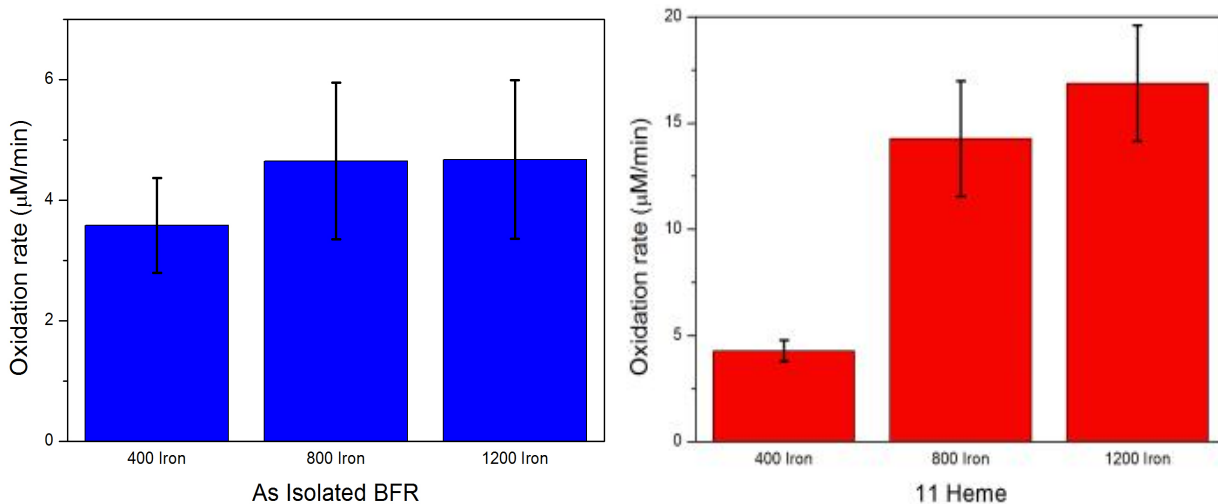


**Figure 5.10.** Phase three Fe(II) oxidation rates for isolated BFR containing 1 heme and heme loaded BFR with 11 hemes. The first initial rates of iron oxidation (400), second initial rates of iron oxidation (800 iron), third oxidation rate with addition of iron to BFR 11 hemes are shown (1200 iron). See Figure 5.9 for experimental details.

Similar experiments were conducted with BFR loaded with 6 hemes, see Figure 5.11. Again, behaviour was somewhat different from that of as isolated BFR.

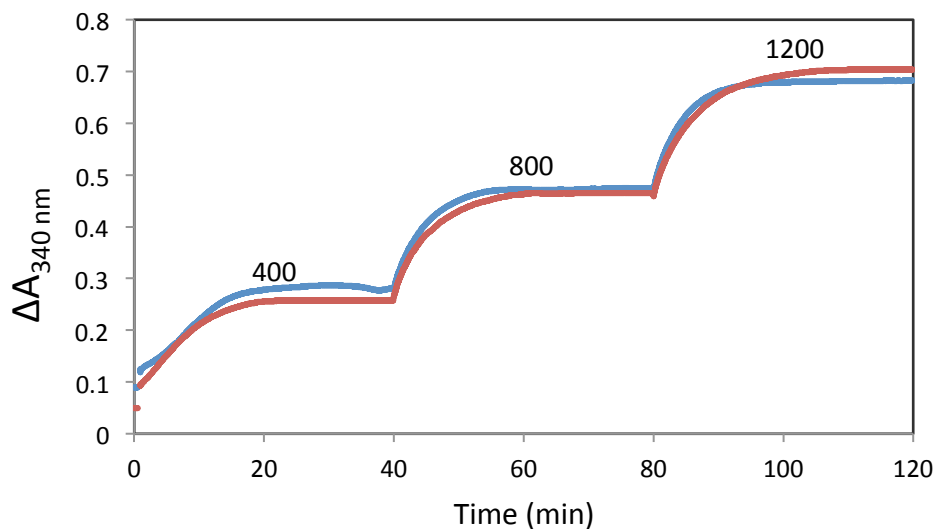


**Figure 5.11.** Iron uptake into *E. coli* BFR. 200 μM Fe<sup>2+</sup> was added to 0.5 μM BFR as isolated BFR (—), and BFR with 6 hemes (—) in MES buffer 0.1 M, pH 6.5, 25 °C. Pathlength 1 cm.

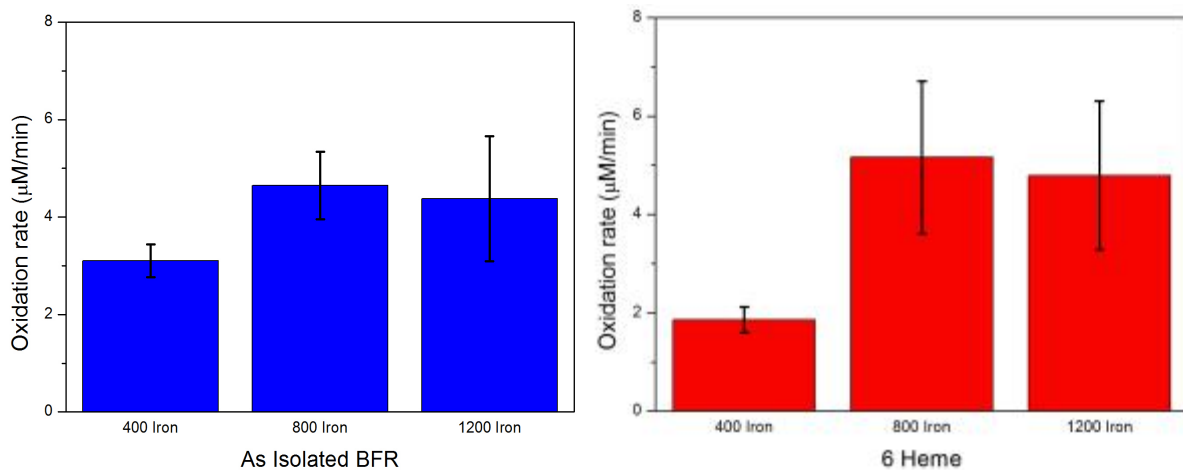
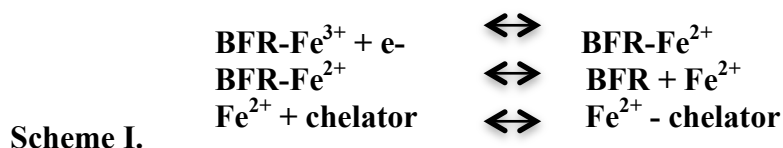


**Figure 5.12.** Phase three oxidation in BFR with isolated BFR (1 heme) and BFR with (6 heme). The first initial rates of iron oxidation (400 iron), second initial rates of iron oxidation (800 iron), third oxidation rate with addition of iron to BFR 6 heme are shown (1200). See Figure 5.11 for experimental details.

### 5.3.2 Effect of heme on iron release from *E. coli* BFR

BFRs are distinct from other ferritin-like proteins in that they contain heme. The BFR 24mer possesses 12 heme-binding sites that are located at intersubunit sites coordinated by Met52 of each subunit, generating unusual bis-methionine axial ligation. Previous studies demonstrated that heme does not play a crucial role in the early stages of iron core formation (39). Recent studies of *E. coli* BFR with higher heme bound revealed a decrease in the rate of iron oxidation at the ferroxidase sites (phase 2) and an increase in the rate of iron core formation (phase 3), consistent with the data in Figure 5.9 (51). However, it was demonstrated recently that heme also plays an important role in iron release (27), although, that study was confined to BFR containing zero, one and five hemes per 24mer (27). A full investigation of the functional role of heme in *E. coli* BFR has been hampered by the difficulty in preparing BFR samples containing high heme levels. Overexpression of recombinant BFR usually yields very low levels of heme, and exogenous heme cannot be added to reconstitute the unoccupied heme-binding sites. Heme levels were increased to ~5 per protein by induction of protein production with very low

concentration of the inducer, IPTG. In order to overcome this difficulty, we utilized the procedure that allows the reconstitution of *E. coli* BFR sample with higher amounts of bound heme. We wished to evaluate, using BFR samples containing a range of heme loadings, whether higher heme levels are important for iron release and the influence of varying heme on the kinetics of iron release. Therefore, these investigations were directed at studying the mobilization of core iron from as isolated wild-type BFR, BFR with various heme added, and heme free M52H BFR. A commonly used chelator-based assay was initially employed. This assay is used was initially employed with the assumption that the chelator does not interfere with the release of iron reaction, see scheme 1.



In the assay, the reaction was initiated by addition of the reductant system, sodium dithionite/FMN, to a cuvette containing a solution of ferrozine (1 mM) and BFR mineralized with ~1200 iron ions. The process was monitored by following the absorbance change at 562 nm due to time-dependent formation of  $[\text{Fe(II)(ferrozine)}_3]^{4-}$ . In the absence of reductant a rapid increase at 562 nm was not observed, due to lack of free  $\text{Fe}^{2+}$  (27). The addition of sodium dithionite 100  $\mu\text{M}$ , 100  $\mu\text{M}$  FMN to BFR containing ~1200  $\text{Fe}^{3+}$ /protein and 6 hemes resulted in an increase of absorption overtime, indicating that electrons were supplied to the mineral core to reduce iron from  $\text{Fe}^{3+}$  to  $\text{Fe}^{2+}$  leading to formation of the  $\text{Fe}^{2+}$ -chelator complex. The kinetic profile of iron release at pH 6 and pH 7 demonstrated that, although some differences were observed, there was no great variation in iron release kinetics upon varying pH (Figure 5.13). This behaviour is similar to that previously reported for BFR; some variation was seen when

comparing ferrozine and bipyridyl at the two pH values but it was concluded that variation is due to the effect of chelator and not to pH (27). The data were relatively similar with a rapid phase occurring in less than five minutes, and a slower phase that occurs after 5 minutes. The data showed wild-type BFR with 1 heme had a slightly lower rate of iron release than BFR with 6 hemes. Data was fitted well to a double exponential function, with the majority of the amplitude associated with the first phase. For pH 7, fits provided rate constants of  $1.82 (\pm 0.006) \text{ min}^{-1}$  and  $1.876 (\pm 0.007) \text{ min}^{-1}$  for as isolated BFR and 6 heme BFR, respectively. For pH 6, rate constants of  $1.44 (\pm 0.01) \text{ min}^{-1}$  and  $1.46 (\pm 0.02) \text{ min}^{-1}$  were obtained for as isolated BFR and 6 heme BFR, respectively. The extent of iron release was also calculated using  $[\text{Fe(II)(ferrozine)}_3]^{4-}$  complex using ( $\epsilon_{562 \text{ nm}} = 28,000 \text{ M}^{-1} \text{ cm}^{-1}$ ) and absorbance at the end of each release reaction. The extent of iron release at pH 7, 52.0% and 44.1% were obtained for as isolated BFR and 6 heme BFR, respectively. For pH 6, 45.2% and 43.1% value were acquired for as isolated BFR and 6 heme BFR. Thus, the rate constants for iron release are not significantly different. The extent of iron release was reduced for the 6-heme containing sample.

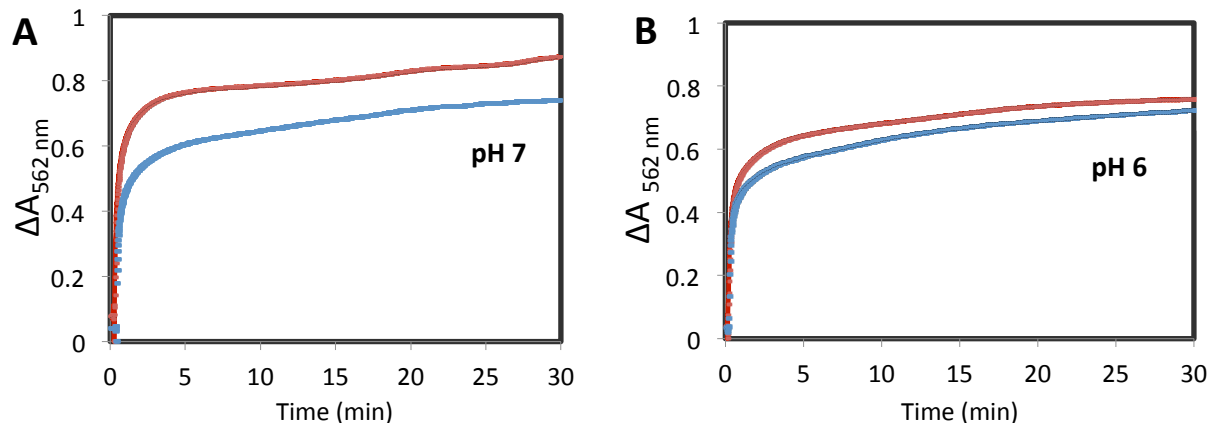


**Figure 5.13.** The influence of heme on iron release from *E. coli* BFR, utilizing dithionite/FMN as reductant and ferrozine as chelator. Time-dependent increases of  $A_{562\text{nm}}$  following the addition of 100  $\mu\text{M}$  dithionite and 100  $\mu\text{M}$  FMN to either 6 heme loaded BFR (blue line) or as isolated wild-type containing 1 heme BFR (red line) in the presence of 1 mM Ferrozine. Both BFRs were loaded with 1200 iron ions (0.05  $\mu\text{M}$  BFR) in MBS. The release reaction was carried out at 25  $^{\circ}\text{C}$ . (A) pH 7 and (B) pH 6. Pathlength 1 cm.

The data suggest there are two phases in iron release, a very rapid phase and a slower phase that increased overtime in the presence of excess reductant. Furthermore, additions of sodium dithionite (200  $\mu\text{M}$ ) to 0.05  $\mu\text{M}$  BFR loaded with 11 hemes and as isolated wild-type BFR in MBS buffer in the presence of the chelator Ferrozine (1 mM) at pH 7, also resulted in a much reduced extent of iron release for the 11 hemes sample compared to as isolated wild-type BFR that contains 1 heme (Figure 5.14). The data demonstrated lower iron release in the presence of higher heme levels. The data was fitted well to a double exponential function, with the majority of the amplitude associated with the first phase. This gave rate constants of 0.785 ( $\pm 0.005$ )  $\text{min}^{-1}$ , and 1.045 ( $\pm 0.008$ )  $\text{min}^{-1}$  for as isolated BFR and 11 hemes BFR, respectively. The extent of iron release was also calculated, 67.9 % and 33.7% value were obtained for as isolated BFR and 11 hemes BFR, respectively. Thus, an increase in heme content resulted in a small increase in the rate of iron release, but a decrease in the extent of iron release.

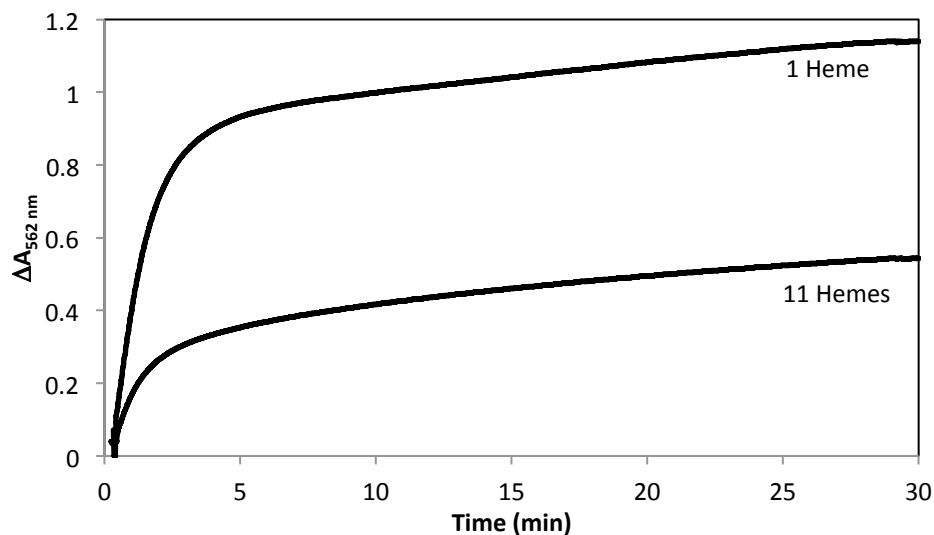


**Figure 5.14.** The influence of heme on iron release from *E. coli* BFR utilizing dithionite as a reductant and ferrozine as a chelator. Time-dependent increases of  $\Delta A_{562\text{nm}}$  following the addition of 200  $\mu\text{M}$  dithionite, to either 11 heme loaded BFR(dashed lines) or isolated wild-type containing 1 heme BFR (solid line). Both BFRs were loaded with 1200 iron ions (0.05  $\mu\text{M}$  BFR) in MBS, 1 mM Ferrozine as a chelator and conducted pH 7 and at 25 °C. Pathlength 1 cm.

The data presented here indicate quite different behaviour compared to that previously reported (27). To check that this was not due to a problem with how the experiments were being performed some additional checks were made. Similar experiments were carried out with heme-free M52H BFR and as isolated wild-type BFR using the FMN/dithionite-chelator assay in an anaerobic environment at pH 7 and pH 6. Figure 5.15 shows a plot of absorbance change at 562 nm as a function of time following the addition of sodium dithionite 100  $\mu\text{M}$ , 75  $\mu\text{M}$  FMN to BFR proteins containing  $\sim 1200 \text{ Fe}^{3+}$ /protein in MBS buffer with Ferrozine (1 mM). The data demonstrated iron release was pH dependent and heme-free M52H BFR exhibited a lower rate and extent of iron release compared to wild-type BFR. Data was fitted well to a double exponential function, with the majority of the amplitude associated with the first phase. For pH 7, it provided rate constant of 3.83 ( $\pm 0.004$ )  $\text{min}^{-1}$ , and 2.94 ( $\pm 0.005$ )  $\text{min}^{-1}$  for as isolated BFR

and heme-free M52H BFR, respectively. For pH 6, it provided rate constant of  $7.36 (\pm 0.006)$   $\text{min}^{-1}$ , and  $6.40 (\pm 0.005)$   $\text{min}^{-1}$  for as isolated BFR and heme-free M52H BFR, respectively. The amount of iron released could be calculated from the end points of the kinetic profiles. For pH 7, 49.5%, and 35.1% amount of iron release was obtained for as isolated BFR and heme-free M52H BFR, respectively. For pH 6, the extents of iron release were 48.7%, and 38.8% for as isolated BFR and heme-free M52H BFR, respectively.

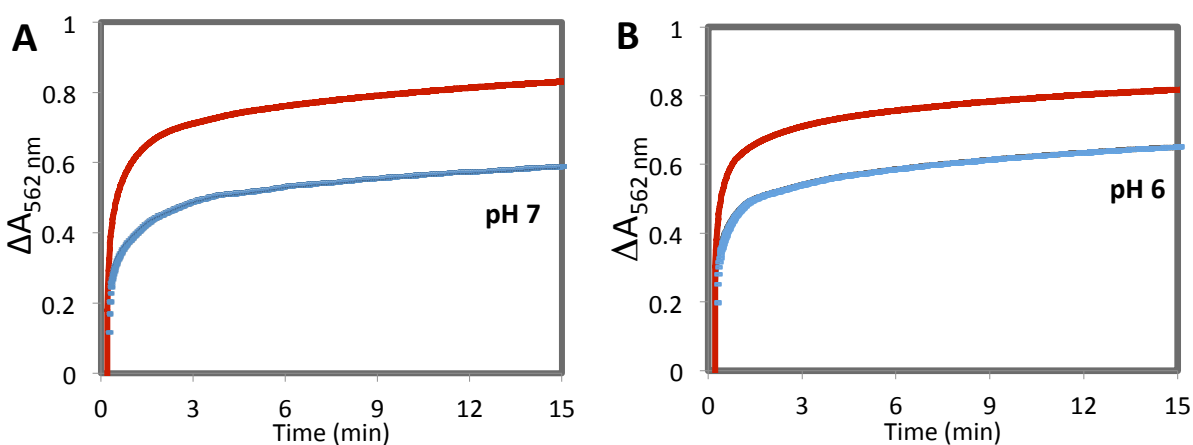


**Figure 5.15.** The influence of heme on iron release in *E. coli* BFR by utilizing dithionite as a reductant/FMN and ferrozine as a chelator. Time-dependent increases of  $\Delta A_{562\text{nm}}$  following the addition of  $100 \mu\text{M}$  dithionite,  $75 \mu\text{M}$  FMN to either heme-free (M52H) BFR (blue line) or as isolated wild-type containing 1 heme BFR (red line). Both BFRs were loaded with 1200 iron ions ( $0.05 \mu\text{M}$  BFR) in MBS, and 1 mM Ferrozine. The release reaction was carried out at  $15^\circ\text{C}$ . (A) pH 7 and (B) pH 6. Pathlength 1 cm.

Previous studies of iron release from BFR showed that the presence of a chelator influenced the rate of the release, i.e. the chelator is not an innocent reporter of iron release, but instead is actively involved in the process. To remove the influence of the chelator, a modified iron release assay was designed, in which the reductant was added to initiate release, and the chelator added at increasing time points. The instantaneous increase in absorbance measured immediately upon addition of the chelator represents the concentration of iron that has been released at that time

point. To obtain an indication of the true iron release rate, dithionite 100  $\mu$ M and 100  $\mu$ M FMN were added to the 5 heme BFR solution that contains  $\sim$ 1200 irons at pH 7, and then the ferrozine chelator was added at increasing time points. Figure 5.16 shows the instantaneous observed jumps in absorbance at 562 nm (due to the formation of Fe(II)-ferrozine-complex) plotted as a function of increasing time between addition of reductant and the addition of chelator. The data suggest that Fe(II) was not entirely held within the BFR cavity after the reduction of the core. About 50% of iron was available as soon as the reductant was added. This behaviour is very different from that previously reported for wild-type BFR. In combination, the data reported here suggest that the in vitro heme loading method significantly affects the iron-release properties of the protein.

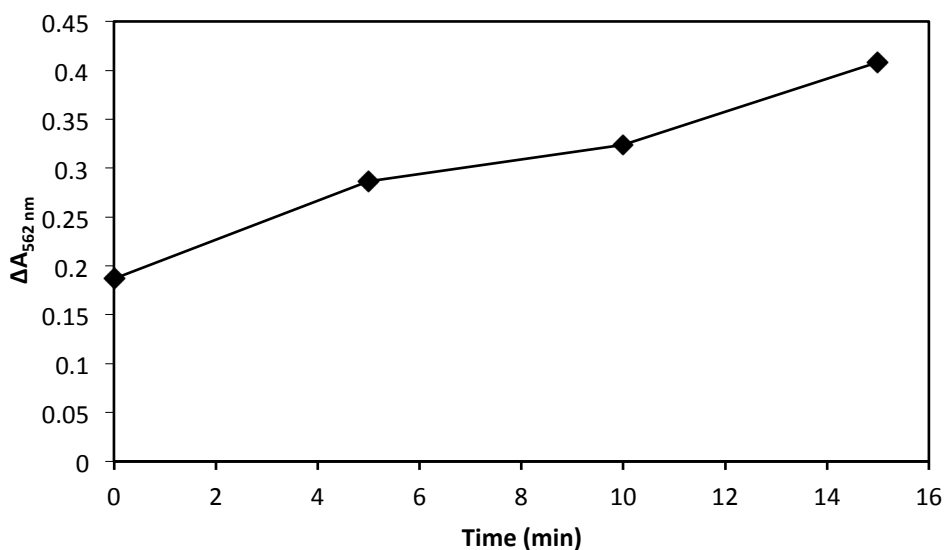


**Figure 5.16.** The influence of heme on iron release in the absence of ferrozine, a high affinity ferrous chelator. Plot of the instantaneous increase of absorbance after the addition of the chelator. Time-dependent increases of  $\Delta A_{562\text{nm}}$  following the addition of 100  $\mu$ M dithionite, 100  $\mu$ M FMN to 5 heme loaded BFR. BFR 0.05  $\mu$ M BFR loaded with 1200 iron ions in MBS, with addition of 100  $\mu$ M dithionite, 100  $\mu$ M FMN, 1 mM Ferrozine pH 7, 0.05  $\mu$ M BFR 15  $^{\circ}$ C. Pathlength 1 cm.

## 5.4 Discussion

### 5.4.1 The mechanism of exogenous heme-binding to BFR

Overexpressed recombinant *E. coli* BFR contains very low amounts of heme, usually as low as one per 24mer. Figure 5.2 shows, and as previously reported (73), addition of exogenous heme is not incorporated into the BFR heme-binding site. Structural studies of BFR showed why this is so, the heme-binding site is inaccessible from the outside of the protein (73). Previous attempts to gain higher levels of heme involved inducing expression of the *bfr* gene with low levels of IPTG, supplementation of cultures with iron and aminolevulinic acid (the first dedicated intermediate of heme synthesis), resulting in five hemes per 24mer (27). In this study, various amounts of heme were added to BFR, resulting in 5, 6, 7 and 11 hemes per 24mer. BFR with 12 hemes was also achieved, but higher amounts of hemein chloride was needed to fully occupy the intersubunit heme-binding site. Addition of a large excess of heme results in heme-binding to non-specific sites, which was difficult to remove.

The mechanism of this reconstitution method is not fully understood and further investigation is needed. However, there are some clear possibilities. With increasing temperature, the BFR 24mer may dissociate into smaller assemblies, allowing heme to enter the heme-binding sites. Heating the 24mer in a low or insufficient ionic strength solution leads to denaturation of the dissociating protein. However, in the presence of high ionic strength (such as 1 M NaCl) the secondary structure is stabilized, and facilitates restoration to its native structure upon cooling. Another possibility is that a melting of secondary structure within each subunit occurs, enabling heme to enter through a newly formed pore in the protein shell. For example, the two coils between the two subunits above the heme-binding site are close and block heme from entering the heme-binding site. It is possible, that at higher temperatures, these coils located above the

heme-binding site break apart and allows heme to enter the heme-binding site (51).

Further confirmation of specific heme-binding to BFR was provided through studies of the BFR variant, heme-free M52H, in which the heme-coordinating residue is substituted with histidine. These revealed that heme does not bind to this variant, to any significant degree, as only a very low amount of heme was detected, with spectral characteristic similar to those of metmyoglobin. Thus, the 739 nm band, which is due to the methionyl residues provided by two separate subunits, is only observed in the wild-type protein. Note that this coordination is rare with only one other example currently known, in surface protein Shp of *Streptococcus pyogene* (38).

#### **5.4.2 The effect of heme on iron core formation**

The data from iron core formation revealed that higher heme contents resulted in faster iron core oxidation during the late stages of iron core formation; a possible mechanism for this involves the bound heme facilitating electron transfer from Fe(II) in the central cavity to the dinuclear iron ferroxidase sites. Evidence for this suggestion came from a study of iron uptake into BFR reconstituted with Co-protoporphyrin IX compared to that reconstituted with Fe-heme (51). This showed no influence on the Phase 3 kinetics of BFR mineralisation in the protein containing Co-heme. Thus, Fe-heme bound to BFR most likely contributes to some electron-transfer activities as a part of BFR ferroxidase activity (51). An assumption made here was that Co-heme and Fe-heme bind to BFR similarly; this has been shown to be the case for Co-heme-binding to cytochrome c, myoglobin, and haemoglobin (74, 75).

### 5.4.3 The role of Heme in iron release from BFR

Previous studies suggest that heme groups play a major role in both the kinetics and thermodynamics of iron release in a heme-containing BFR (27). BFR samples with 5 hemes had significantly greater iron release and rate constant compared to BFR containing 1 heme and no heme. In the presence of heme there was a 4-fold increase in the rate constant as compared to heme-free M52H BFR. Recently, the structure of the complex between Pa-BFD-BFR was solved, providing structural insight into the mechanism of iron mobilization and the electron path through the BFR shell to reduce Fe(III) in the BFR cavity (49). BFD most likely facilitates release of iron by catalysing the transfer of electrons into the core via the heme. The proposed schematic shows BFD with a [2Fe-2S] cluster, promoting the release of  $\text{Fe}^{2+}$  from BFR by mediating electrons from FPR (NADPH-dependent ferredoxin reductase) to BFR, to heme, Figure 5.17 (49).

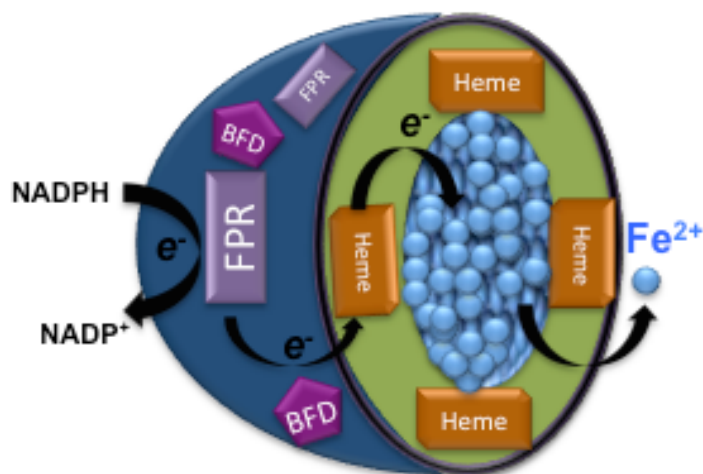


**Figure 5.17.** Proposed requirements for BFR iron release in *pseudomonas aeruginosa*, FPR mediates the flow of electrons from NADPH to the mineral in BFR via the heme and that interactions between Bfd and BFR promote the release of iron.

The reduction potential of *Azotobacter vinelandii* BFR heme was reported to be -225 mV and -475 mV (vs. NHE) in the absence and presence of an iron core, respectively. The iron core has a reduction potential of -420 mV, which suggested that the heme group plays an important role in the reduction of the iron core (51, 76). The data presented here are not consistent with a significant role of heme in iron release and are contradicting to previously published data of iron release from *E. coli* BFR and *P.aeruginosa* BFR. Here the data suggest that increase heme levels only marginally increases the rate of iron release and actually lowers the extent of iron release. To ensure that these unexpected results were not due to a problem with the assay, a comparison of as isolated BFR (containing 1 heme) with M52H BFR (containing no heme) was made. This revealed a positive effect of heme, as previously reported. Thus, one possibility is that the method of heme loading described here somehow affects the protein so that iron release cannot proceed normally.

Clearly, the heme-binding site itself is not affected in terms of its spectroscopic properties. Another possibility is that during the heat treatment the 24mer becomes loosely assembled and does not fully regain its homogeneous 24meric structure upon cooling, such that the iron is not properly stored within the protein. Figure 5.16 suggests that some of the iron may be available to the chelator before the addition of reductant. However, it is not clear why an overall lower amount of iron would be released from heme-loaded samples. Further work will be needed to resolve this.

## Chapter 6: General Discussion

### 6.1 Mechanistic studies of iron uptake by Pennate Diatom Ferritin

The aim of this project was to investigate the catalytic mechanism of iron uptake in the recently discovered diatom ferritin PmFTN. This was of particular interest because the mechanism of mineralisation is not well understood; also PmFTN is the first eukaryotic ferritin with a site C located close to the intra-subunit ferroxidase centre. The investigation of PmFTN focused on kinetic studies of the wild-type and variant proteins and on characterizing the mechanism by which it reacts with iron.

The data presented in chapters 3 and 4, show that that PmFTN can store iron and kinetic measurements of iron oxidation showed an exceedingly rapid initial oxidation phase involving the binding and oxidation of two Fe(II) ions per subunit. However, the exact mechanism of iron uptake in PmFTN remains unclear and further experiments are needed to define what occurs following the initial Fe(II) binding and oxidation at the ferroxidase centre. Nonetheless, several conclusions can be drawn about the mineralisation process based on the data presented here.

The data presented in chapter 3, suggest a mechanism of iron uptake that is different from those previously reported for 24mer ferritins. The ferroxidase centre oxidation reaction is a second order reaction that is dependent on the concentration of Fe(II), indicating that iron binding and oxidation are closely linked such that they cannot be easily distinguished. Since oxidation occurs immediately after Fe(II) binding to PmFTN, the binding event can be viewed as the slow step of the reaction.

The data from crystallographic studies carried out by the Murphy laboratory (UBC) demonstrated that, in the absence of O<sub>2</sub>, Fe(II) only binds at site A of the ferroxidase centre (57). Occupation of sites B and C occurs only when O<sub>2</sub> is present. The stopped-flow data presented shows saturation of the rapid phase 2 at a level of two Fe(II) ions per monomer of PmFTN. Together these results indicate a likely stepwise binding of the Fe(II) and O<sub>2</sub> to ferroxidase sites. A possible mechanism is one in which ferrous iron binding to site A is followed by the binding of the oxidant. Binding of the second ferrous iron to site B, occurs only when the O<sub>2</sub> is bound. This mechanism accounts for the observed rate dependence, because once the second Fe(II) binds, oxidation can occur immediately. Therefore, Fe(II) binding to site B of the ferroxidase site is suggested to be the rate determining step, with binding and oxidation events intimately connected.

Previous studies have shown that the ferroxidase centre reaction of PmFTN consumed dioxygen in a ratio of  $1.9 \pm 0.2$  Fe(II):O<sub>2</sub> (30). The data presented here showed that only two Fe(II) ions are initially bound and oxidised per PmFTN subunit and, if it is assumed that the two Fe(II) ions bind at sites A and B of the ferroxidase centre, site C is not occupied during the initial oxidation reaction. The data suggest that the three Cys residues of PmFtn do not play an important role in Fe(II) oxidation and iron uptake, since similar behaviour was observed for alkylated and non-alkylated forms of wild-protein and for a site-directed variant lacking all three Cys residues.

In chapter 4, the role of site C was further examined. We proposed that in PmFTN Glu44 and Glu130 may be involved in gating the passage of iron from site B to site C. The data suggest that variants E44Q (in Cys-free background), E44H (alkylated) and H130A (alkylated) all exhibited rapid phase 2 oxidation of Fe(II) at the ferroxidase centre with a rate only slightly lower than that of the wild-type protein. However, each of the variants exhibited behaviour

distinct from that of the wild-type protein in that relatively little Fe(II) oxidation occurred below a level of 1 Fe(II) per subunit. This is indicative of a change in Fe(II)-binding properties at the ferroxidase centre. This could be due to a significantly higher Fe(II) binding affinity at one site of the ferroxidase centre relative to the other. Alternatively, it could result from negative cooperativity of Fe(II)-binding at the two sites of the ferroxidase centre. In both cases, Fe(II) binds to the apo-ferroxidase centre in preference to a centre that already contains an Fe(II) ion even when O<sub>2</sub> is present. Because Fe(II) oxidation only occurs when the centre contains two Fe(II) ions, significant oxidation only occurs when more than 24 Fe(II) ions are added to the protein. It is likely that the affinity of Fe(II) for site B is affected in the variants, since the substitution are close to site B (Figure 6.1). In the case of E130A, the residue actually coordinates Fe(II) at site B. However, it is noticeable that the two Glu44 variants exhibit cooperativity to a greater extent.

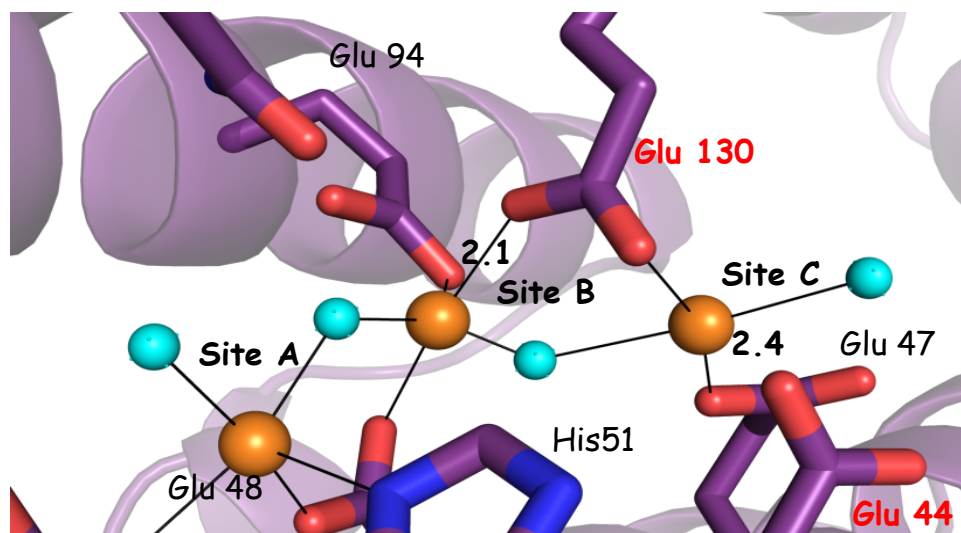


**Figure 6.1.** The substituted residues Glu44 and Glu130, shown in red, exhibit coordination at site C iron. Glu130 is also observed coordinating to site B. Water molecules are shown as blue spheres.

Each of the of E130A, E44Q, and E44H substitutions affected iron oxidation, but for E130A PmFTN there was a very significantly enhanced rate of mineralisation compared to wild-type and E44Q and E44H proteins.

It was recently suggested that a unifying mechanism, in which the Fe(III) product at the ferroxidase site remains bound to the ferroxidase site but is rapidly displaced by incoming Fe(II), could account for the behaviour of all ferritins (67). This unifying mechanism is not consistent with the partially filled ferroxidase centre (site C) observed by crystallography (57), nor kinetic studies. Where immediately following oxidation of Fe(II) at the ferroxidase centre small absorbance changes were observed which are consistent with the idea that the di-Fe(III) form of the centre is unstable, leading to occupation of site C. The rapid ferroxidase centre-catalysed oxidation of ferrous iron in PmFTN was not regenerated upon up to 20 hours incubation specifying that at least some iron remains present at the ferroxidase site. Thus, if Fe(III) is displaced, the subsequent iron oxidation is much slower than the initial oxidation. The mechanism of mineralisation in PmFTN appears to be more complex than either of the two general mechanisms previously outlined in which the centre operates either as a gated pore or as a stable catalytic centre. In PmFTN there is partial iron migration to the core. The two distinct kinetic phases observed after the second addition of 48 Fe(II) iron may also be associated with slow iron migration to the core, likely involving the third iron binding site (site C). Figure 6.2 shows a possible mechanistic scheme for PmFTN mineralisation. The data on E130A are particularly interesting because mineralisation occurs much more rapidly than in the wild-type protein. This suggests that the PmFTN ferroxidase centre may have evolved to be less than optimally active in terms of mineralisation. It is likely that site C is important for this and further studies of more site directed variants will be needed to investigate this. Initially, this could involve the E44A alone and also in combination with the E130A variant.

An unknown species that absorbs at 650 nm is observed to form in PmFTN. Although the wavelength maximum absorbance corresponds to that expected for a 1,2-peroxodiferrous intermediate found in many diiron enzymes, intensity did not decay and so its characteristics are not consistent with those observed for such intermediates in other ferritins. Further experiments with PmFTN would help assign the identity of the species observed in the current work and would provide insight into the mechanism of iron oxidation at the ferroxidase site.

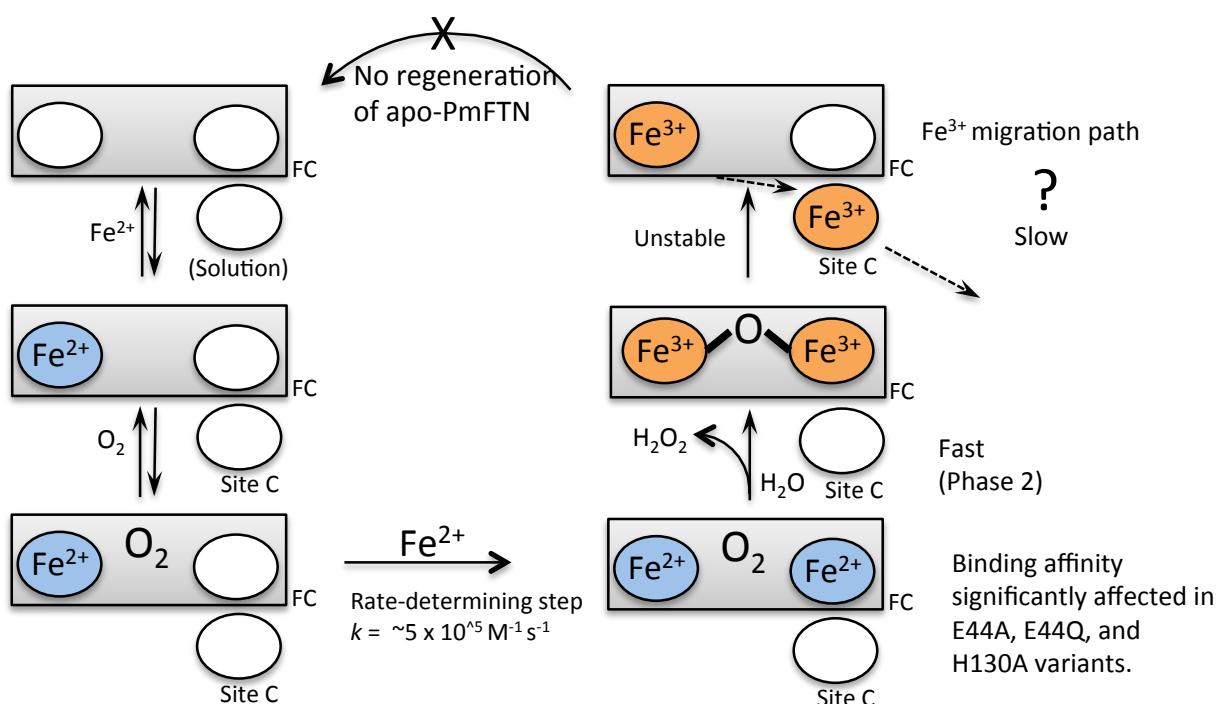


**Figure 6.2.** Schematic model of the representation of mineralisation in PmFTN. Fe<sup>2+</sup> ions bind at the ferroxidase centre and site C (labelled C) and become oxidised, in the presence of oxygen, generating an unstable di-Fe<sup>3+</sup> form at the ferroxidase centre. Fe<sup>3+</sup> ions at site C and the ferroxidase centre are transferred to the internal cavity where they nucleate, or become incorporated into, the mineral iron core. Further Fe(III) remains iron-bound. Oxidised could occur with significantly altered kinetics.

## **6.2 Mechanistic study of iron release from Bacterioferritin**

Previous mechanistic studies of BFR have shown that heme plays a role in iron release (27).

That study was carried out with samples of BFR containing zero, one or five hemes per BFR.

Recently, a novel method for fully loading BFR with heme after purification was devised. It was proposed to use this method to more fully investigate the function of heme in iron release. First, it was necessary to establish that the added heme binds at the native heme-binding site and to then generate a range of heme loaded BFR samples.

The data presented in chapters 5 show that various amounts of heme were successfully added to BFR, up to 11 hemes per 24mer. Further confirmation of specific heme-binding to BFR was provided through studies of the BFR variant, heme-free M52H, in which the heme-coordinating Met residue is substituted with His. The data from iron core formation showed BFR samples containing higher heme (6 and 11 hemes) resulted in faster iron core formation. In the latter stages of mineralisation, as previously reported (51). Thus, heme accelerates the late phases of iron core formation.

The data suggest that increased heme levels only marginally increases the rate of iron release and actually lowers the extent of iron release. Clearly, the heme-binding site itself is not affected in terms of its spectroscopic properties. Further investigation is needed; for example, it is possible that during the heat treatment the 24mer becomes loosely assembled and does not fully regain its homogeneous 24meric structure upon cooling, such that the iron is not properly stored within the protein. Some data suggested that some of the iron may be available to the chelator before the addition of reductant. However, it is not clear why an overall lower amount of iron would be released from heme-loaded samples. Further work will be needed to resolve this.

## References

1. Aisen P, Enns C, Wessling-Resnick M. 2001. *Int J Biochem Cell Biol* 33: 940-59
2. Yang X, Le Brun NE, Thomson AJ, Moore GR, Chasteen ND. 2000. *Biochemistry* 39: 4915-23
3. Chasteen ND, Harrison PM. 1999. *J Struct Biol* 126: 182-94
4. Kehrer JP. 2000. *Toxicology* 149: 43-50
5. Chiancone E, Ceci P, Ilari A, Ribacchi F, Stefanini S. 2004. *Biometals* 17: 197-202
6. Theil EC. 1990. *Advances in Enzymology and Related Areas of Molecular Biology* 63: 421-49
7. Arosio P, Ingrassia R, Cavadini P. 2009. *Biochimica Et Biophysica Acta-General Subjects* 1790: 589-99
8. Bou-Abdallah F. 2010. *Biochimica et Biophysica Acta (BBA) - General Subjects* 1800: 719-31
9. Le Brun NE, Crow A, Murphy ME, Mauk AG, Moore GR. 2010. *Biochim Biophys Acta* 1800: 732-44
10. Lewin A, Moore GR, Le Brun NE. 2005. *Dalton transactions*: 3597-610
11. Weeratunga SK, Lovell S, Yao H, Battaile KP, Fischer CJ, et al. 2010. *Biochemistry* 49: 1160-75
12. Schrodinger, LLC. 2010. The AxPyMOL Molecular Graphics Plugin for Microsoft PowerPoint, Version 1.0.
13. Pulliainen AT, Kauko A, Haataja S, Papageorgiou AC, Finne J. 2005. *Molecular Microbiology* 57: 1086-100
14. Abdul-Tehrani H, Hudson AJ, Chang YS, Timms AR, Hawkins C, et al. 1999. *Journal of Bacteriology* 181: 1415-28
15. Ratnayake DB, Wai SN, Shi YX, Amako K, Nakayama H, Nakayama K. 2000. *Microbiology-Uk* 146: 1119-27
16. Zhao GH, Ceci P, Ilari A, Giangiacomo L, Laue TM, et al. 2002. *Journal of Biological Chemistry* 277: 27689-96
17. Smith JL. 2004. *Critical reviews in microbiology* 30: 173-85
18. Velayudhan J, Castor M, Richardson A, Main-Hester KL, Fang FC. 2007. *Molecular microbiology* 63: 1495-507
19. Ma JF, Ochsner UA, Klotz MG, Nanayakkara VK, Howell ML, et al. 1999. *Journal of bacteriology* 181: 3730-42
20. Bou-Abdallah F, Lewin AC, Le Brun NE, Moore GR, Chasteen ND. 2002. *J Biol Chem* 277: 37064-9
21. Theil EC. 2011. *Current Opinion in Chemical Biology* 15: 304-11
22. Crichton RR, Declercq JP. 2010. *Biochimica et biophysica acta* 1800: 706-18
23. Tosha T, Ng H-L, Bhattasali O, Alber T, Theil EC. 2010. *Journal of the American Chemical Society* 132: 14562-9
24. Haldar S, Bevers LE, Tosha T, Theil EC. 2011. *Journal of Biological Chemistry* 286: 25620-7
25. Zhao G, Bou-Abdallah F, Arosio P, Levi S, Janus-Chandler C, Chasteen ND. 2003. *Biochemistry* 42: 3142-50

26. Turano P, Lalli D, Felli IC, Theil EC, Bertini I. 2010. *Proceedings of the National Academy of Sciences of the United States of America* 107: 545-50
27. Yasmin S, Andrews SC, Moore GR, Le Brun NE. 2011. *The Journal of biological chemistry* 286: 3473-83
28. Crow A, Lawson TL, Lewin A, Moore GR, Le Brun NE. 2009. *Journal of the American Chemical Society* 131: 6808-13
29. Watt RK, Hilton RJ, Graff DM. 2010. *Biochimica et biophysica acta* 1800: 745-59
30. Marchetti A, Parker MS, Moccia LP, Lin EO, Arrieta AL, et al. 2009. *Nature* 457: 467-70
31. Bertini I, Lalli D, Mangani S, Pozzi C, Rosa C, et al. 2012. *Journal of the American Chemical Society* 134: 6169-76
32. Honarmand Ebrahimi K, Hagedoorn PL, Jongejan JA, Hagen WR. 2009. *Journal of biological inorganic chemistry : JBIC : a publication of the Society of Biological Inorganic Chemistry* 14: 1265-74
33. Stillman TJ, Hempstead PD, Artymiuk PJ, Andrews SC, Hudson AJ, et al. 2001. *Journal of molecular biology* 307: 587-603
34. Tatur J, Hagen WR, Matias PM. 2007. *Journal of biological inorganic chemistry : JBIC : a publication of the Society of Biological Inorganic Chemistry* 12: 615-30
35. Stiefel EI, Watt GD. 1979. *Nature* 279: 81-3
36. Bulen WA, LeCompte JR, Lough S. 1973. *Biochemical and biophysical research communications* 54: 1274-81
37. Barker PD, Nerou EP, Cheesman MR, Thomson AJ, de Oliveira P, Hill HA. 1996. *Biochemistry* 35: 13618-26
38. Cheesman MR, Thomson AJ, Greenwood C, Moore GR, Kadir F. 1990. *Nature* 346: 771-3
39. Andrews SC, Le Brun NE, Barynin V, Thomson AJ, Moore GR, et al. 1995. *J Biol Chem* 270: 23268-74
40. Andrews SC, Smith JM, Hawkins C, Williams JM, Harrison PM, Guest JR. 1993. *European journal of biochemistry / FEBS* 213: 329-38
41. Le Brun NE, Andrews SC, Guest JR, Harrison PM, Moore GR, Thomson AJ. 1995. *Biochem J* 312 ( Pt 2): 385-92
42. Nordlund P, Eklund H. 1995. *Current opinion in structural biology* 5: 758-66
43. Proulxcurry PM, Chasteen ND. 1995. *Coordination Chemistry Reviews* 144: 347-68
44. Baaghil S, Lewin A, Moore GR, Le Brun NE. 2003. *Biochemistry* 42: 14047-56
45. Romao CV, Louro R, Timkovich R, Lubben M, Liu MY, et al. 2000. *FEBS letters* 480: 213-6
46. Aitken-Rogers H, Singleton C, Lewin A, Taylor-Gee A, Moore GR, Le Brun NE. 2004. *J Biol Inorg Chem* 9: 161-70
47. Watt GD, Frankel RB, Jacobs D, Huang H, Papaefthymiou GC. 1992. *Biochemistry* 31: 5672-9
48. Quail MA, Jordan P, Grogan JM, Butt JN, Lutz M, et al. 1996. *Biochemical and biophysical research communications* 229: 635-42
49. Yao H, Wang Y, Lovell S, Kumar R, Ruvinsky AM, et al. 2012. *Journal of the American Chemical Society* 134: 13470-81
50. Yao H, Jepkorir G, Lovell S, Nama PV, Weeratunga S, et al. 2011. *Biochemistry* 50: 5236-48

51. Wong SG, Abdulqadir R, Le Brun NE, Moore GR, Mauk AG. 2012. *The Biochemical journal* 444: 553-60
52. Gibbs CR. 1976. *Analytical Chemistry* 48: 1197-201
53. Cheesman MR, le Brun NE, Kadir FH, Thomson AJ, Moore GR, et al. 1993. *Biochem J* 292 ( Pt 1): 47-56
54. Richards TD, Pitts KR, Watt GD. 1996. *J Inorg Biochem* 61: 1-13
55. Treffry A, Zhao ZW, Quail MA, Guest JR, Harrison PM. 1998. *Febs Letters* 432: 213-8
56. Pereira AS, Small W, Krebs C, Tavares P, Edmondson DE, et al. 1998. *Biochemistry* 37: 9871-6
57. Pfaffen S, Abdulqadir R, Le Brun NE, Murphy MEP. 2013. *Journal of Biological Chemistry*
58. Treffry A, Zhao ZW, Quail MA, Guest JR, Harrison PM. 1997. *Biochemistry* 36: 432-41
59. Crow A, Liu Y, Moller MC, Le Brun NE, Hederstedt L. 2009. *J Biol Chem* 284: 10056-66
60. Langlois d'Estaintot B, Santambrogio P, Granier T, Gallois B, Chevalier JM, et al. 2004. *Journal of molecular biology* 340: 277-93
61. Wong SG, Tom-Yew SA, Lewin A, Le Brun NE, Moore GR, et al. 2009. *J Biol Chem* 284: 18873-81
62. Schwartz JK, Liu XS, Tosha T, Diebold A, Theil EC, Solomon EI. 2010. *Biochemistry* 49: 10516-25
63. Treffry A, Hirzmann J, Yewdall SJ, Harrison PM. 1992. *Febs Letters* 302: 108-12
64. Bauminger ER, Harrison PM, Hechel D, Nowik I, Treffry A. 1991. *Biochimica Et Biophysica Acta* 1118: 48-58
65. Hwang J. 2000. *Science* 287: 807-
66. Tatur J, Hagen WR. 2005. *Febs Letters* 579: 4729-32
67. Honarmand Ebrahimi K, Bill E, Hagedoorn PL, Hagen WR. 2012. *Nature chemical biology* 8: 941-8
68. Johnson E, Cascio D, Sawaya MR, Gingery M, Schroder I. 2005. *Structure* 13: 637-48
69. Hempstead PD, Yewdall SJ, Fernie AR, Lawson DM, Artymiuk PJ, et al. 1997. *Journal of Molecular Biology* 268: 424-48
70. Kendrew JC, Bodo G, Dintzis HM, Parrish RG, Wyckoff H, Phillips DC. 1958. *Nature* 181: 662-6
71. Schuller DJ, Wilks A, Ortiz de Montellano PR, Poulos TL. 1999. *Nature structural biology* 6: 860-7
72. Yoshida T, Kikuchi G. 1979. *The Journal of biological chemistry* 254: 4487-91
73. Moore GR, Kadir FHA, Almassad FK, Lebrun NE, Thomson AJ, et al. 1994. *Biochemical Journal* 304: 493-7
74. Hoffman BM, Petering DH. 1970. *Proceedings of the National Academy of Sciences of the United States of America* 67: 637-43
75. Moore GR, Williams RJP, Chien JCW, Dickson LC. 1980. *Journal of Inorganic Biochemistry* 12: 1-15
76. Cheesman MR, Kadir FH, al-Basseet J, al-Massad F, Farrar J, et al. 1992. *The Biochemical journal* 286 ( Pt 2): 361-7

77. J.D> Thompson, D.g. Higgins, T.J. Gibson, CLUSTAL W: improving the sensitivity of progressive multiple sequcne alignmet though sequence weighting, position speicif gap penalties and weight matrix choice, *Nucl. Acids Res.* 22. 1994 4673-468
78. K.B. Nicholas, H.B Nicholas Jr., Genedoc: A tool for eding and naotating mulptple sequence alignments, distubted by the authors, 1997.